UNIVERSITY OF OKLAHOMA

GRADUATE COLLEGE

IN SITU OBSERVATIONS OF SOUTHERN OCEAN CLOUDS FROM THE
SOCRATES FIELD CAMPAIGN: EVALUATING CLOUD PHASE, AEROSOL-
CLOUD INTERACTIONS, CLOUD LAYER TYPES AND ENTRAINMENT-MIXING
IMPACTS ON MIXED PHASE CLOUDS

A DISSERTATION

SUBMITTED TO THE GRADUATE FACULTY

in partial fulfillment of the requirements for the

Degree of

DOCTOR OF PHILOSOPHY

By

John D'Alessandro
Norman, Oklahoma
2022

IN SITU OBSERVATIONS OF SOUTHERN OCEAN CLOUDS FROM THE
SOCRATES FIELD CAMPAIGN: EVALUATING CLOUD PHASE, AEROSOL-
CLOUD INTERACTIONS, CLOUD LAYER TYPES AND ENTRAINMENT-MIXING
IMPACTS ON MIXED PHASE CLOUDS

A DISSERTATION APPROVED FOR THE
SCHOOL OF METEOROLOGY

BY THE COMMITTEE CONSISTING OF

Dr. Greg M. McFarquhar, Chair

Dr. Jens Redemann

Dr. Scott T. Salesky

Dr. Amy McGovern

Dr. Andrew H. Fagg

ABSTRACT

Low level clouds are ubiquitous over the Southern Ocean. However, climate and weather models fail to accurately simulate their radiative impact. This has been attributed in part to the inadequate representation of cloud phase distributions. Using in situ airborne observations acquired during the Southern Ocean Clouds, Radiation, Aerosol Transport Experimental Study (SOCRATES) campaign, this dissertation classifies cloud samples with horizontal spatial resolutions ranging from 120–150 m as either liquid, ice or mixed phase (i.e., liquid and ice particles in the same volume). Cloud phase is determined using a combination of data from the in situ cloud probes and a supervised machine learning algorithm, which determines phase based on particle imagery. An abundance of liquid phase samples is observed over the region (70%) at temperatures from -20° to 0°C. The prevalence of supercooled liquid abruptly decreases to single digit percentages at temperatures less than -20°C. There is also a notable ice phase presence (10%) at relatively high temperatures (> -5°C).

Ice nucleating particle (INP) and cloud condensation nuclei (CCN) concentrations are compared with relative cloud phase frequencies within and above the boundary layer. A positive correlation is found between INP concentrations and ice-containing cloud phase (i.e., ice and mixed phase) frequencies in select cases. However, many cases do not exhibit significant correlation, suggesting a prevalence of alternative ice initiation/growth processes, such as secondary ice production. CCN concentrations are negatively correlated with ice-containing frequencies above the boundary layer, which may be related to longer lifetimes of supercooled liquid clouds in high CCN environments. A strong negative correlation is also found between CCN and large cloud drop (> 25 μm)

number concentrations, suggesting secondary ice production may be inhibited in the presence of high CCN concentrations.

A novel cloud layer classification method is introduced to classify cloud layers into single-layer and multi-layer clouds. Normalized occurrence frequencies of ice-containing phases are greater for multi-layer clouds (0.10–0.32) compared with single-layer clouds (0.05). Frequencies are greatest for the lowest cloud layers of multi-layer clouds, and then incrementally decrease up to the third highest layer. When classifying multi-layer clouds as the lowest, highest, and middle cloud layers, ice-containing frequencies for the lowest and middle cloud layers are similar. These frequencies are greater than those for the highest layers and single-layer clouds, which are also similar to each other. The tendency of greater ice-containing frequencies within the lowest layers of multi-layer clouds suggests a prominent seeder-feeder mechanism exists over the region.

A novel quantitative measure of phase spatial heterogeneity is introduced and used to show that the mixed (liquid) phase is the most (least) spatially heterogeneous phase from temperatures between -20° and 0°C. Greater spatial heterogeneity is associated with broader vertical velocity distributions, suggesting increased turbulence is directly related to spatial heterogeneity. Distributions of precipitation-size particle (diameter > 50 μm) mass and mean diameter shift towards smaller values with greater heterogeneity. These particles are primarily ice, which are observed in mixed and ice phase samples. This may be due to a relationship between cloud lifetime and spatial heterogeneity, where ice particles grow as a mixed phase cloud glaciates resulting in decreasing spatial heterogeneity.

Differences in microphysical properties between coupled and decoupled

environments are examined. No significant differences are observed for relative phase frequencies or the spatial heterogeneity. However, drop number concentrations were approximately doubled in coupled environments compared to decoupled environments.

Entrainment-mixing has been shown to impact drop size distributions in warm clouds, but few studies have considered the impacts on mixed phase clouds. By taking advantage of strong correlations between droplet clustering and entrainment-mixing, a clustering metric is used as a proxy to assess the degree of entrainment-mixing in order to maximize the sample size for a statistical analysis of entrainment-mixing impacts on mixed phase cloud properties. A positive relationship is found between the magnitude of droplet clustering and large ice crystal concentrations (diameters greater than ~300 μm), suggesting entrainment-mixing can enhance the Wegener-Bergeron-Findeisen (WBF) process. Particle size distribution functions averaged over different ranges of liquid (LWC) to total water content (TWC) ratio provide insight into the relation of entrainment-mixing to mixed phase cloud evolution. Mixed phase samples with the greatest large ice crystal concentrations occur for LWC/TWC<0.4 in moderate clustering regions. However, these samples are relatively few, whereas high clustering regions have a greater frequency of samples with LWC/TWC<0.4. This suggests sublimation/vapor sinks associated with entrainment can counteract the enhanced WBF. In high clustering regions, small drop concentrations are relatively constant and large droplets (>30 μm) are preferentially removed as LWC/TWC transitions from 1 to 0, representative of glaciation.

These results should provide key insights towards improving the representation of Southern Ocean clouds in both low and high resolution models, as well as improve our overall understanding of varying Southern Ocean cloud types and mixed phase clouds.

ACKNOWLEDGEMENTS

COPYRIGHT NOTICE

Chapter 2 is adapted from a paper published in *Journal of Geophysical Research: Atmospheres* (D'Alessandro et al., 2021) with minor formatting changes. The paper is available to public with open access at https://doi.org/10.1029/2020JD034482.

These documents are distributed under the Creative Commons Attribution 4.0 License (https://creativecommons.org/licenses/by/4.0/) by Copernicus Publications. Under this license, the documents can be shared and adapted if appropriate credit is given, the license is linked, and changes are indicated.

For more information on journal policy regarding license and copyright: https://agupubs.onlinelibrary.wiley.com/hub/journal/24711403/open-access.html.

TABLE OF CONTENTS

LIST OF TABLES

LIST OF FIGURES

1 Introduction

1.1. Clouds over the Southern Ocean

Low-level clouds are ubiquitous over the Southern Ocean, with an annual mean cloud fraction exceeding 80% (e.g., Kay et al., 2012; Mace et al., 2009). These clouds generally reside between the -40°C and -0°C isotherms, meaning either supercooled liquid drops, ice particles or a combination of both (i.e., mixed phase samples) can exist. Both single- and multi-layer low-level clouds are observed over the region, with 34% of cloud cover being multi-layered (Haynes et al., 2011). There are still uncertainties concerning the formation of multi-layer clouds, as multiple pathways for their development have been proposed (e.g., Herman & Goody, 1976; Luo et al., 2008; Tsay & Jayaweera, 1984). Further improving our understanding of such clouds is crucial since overlying layers can cause differences in net radiative fluxes at top-of-atmosphere or towards the surface on the order of 10 W m^{-2} (Christensen et al., 2013; Li et al., 2011).

Due to the remoteness of the Southern Ocean, few field campaigns have taken place over the region. Some include the Aerosol Characterization Experiment (ACE-1; Bates et al., 1998), a few legs of the HIAPER Pole-to-Pole Observations (HIPPO; Wofsy et al. 2011) and the O_2/N_2 Ratio and CO_2 Airborne Southern Ocean Study (ORCAS; Stephens et al., 2018). Previous in situ studies from these campaigns have found a prevalence of supercooled liquid over the region (Chubb et al., 2016; Chubb et al., 2013; D'Alessandro et al., 2019), although most of the campaigns' primary objects were unrelated to obtaining cloud microphysical measurements. Due to the greater sampling frequency of satellite platforms, a relatively large number of studies using satellite retrievals have been performed to quantify phase partitioning over the Southern Ocean.

These studies have previously noted a large frequency of supercooled liquid water over the region (e.g., Mace, 2010; Morrison et al., 2011). However, satellite observations are often restricted to cloud top measurements (e.g., Coopman et al., 2020; Riedi et al., 2010). There are also uncertainties associated with cloud edge (e.g., Nagao & Suzuki, 2021), low-level cloud retrievals due to attenuation (e.g., Hu et al., 2009), and problems with low solar zenith angles (e.g., Khanal & Wang, 2018).

1.2. Simulating Southern Ocean Clouds

Previous studies have noted large discrepancies in simulated outgoing shortwave radiation over the Southern Ocean compared to observed radiative fluxes. In fact, the shortwave error of most climate models is greatest over this latitudinal band (~50°S to 70°S), and the outgoing shortwave radiation is on the order of 10 W m^{-2} lower than observed (Bodas-Salcedo et al., 2014). These errors have been attributed to simulating too little supercooled liquid (Bodas-Salcedo et al., 2016) as well as unrealistically low cloud fraction (Naud et al., 2014), which primarily occurs in the cold sector of midlatitude cyclones (Trenberth & Fasullo, 2010). The newest iteration of the Coupled Model Intercomparison Project (CMIP version 6) has recently been released, and recent studies have highlighted improvements towards increasing the frequency of supercooled liquid. However, there are still issues in capturing the observed drop concentrations over the region (Gettelman et al., 2020; McCoy et al., 2021) and some models now produce unrealistically high liquid phase frequencies (Yang et al., 2021). There are still significant errors in zonal mean shortwave cloud radiative effect over the Southern Ocean for the CMIP version 6 models (Schuddeboom & McDonald, 2021), which have been attributed to continued errors in simulated cloud microphysics (Fiddes et al., 2022). It is crucial to

correctly represent phase partitioning in low and high resolution models due to its impacts on cloud radiative properties (McFarquhar & Cober, 2004; Sun & Shine, 1994) and precipitation tendencies (Mülmenstädt et al., 2015).

Previous studies have noted additional uncertainties and limitations contributing to simulated errors in cloud properties. One example is the spatial distribution of liquid and ice particles in a mixed phase sample. Most models simply assume liquid and ice particles are homogenously mixed (e.g., Zhang et al., 2019). However, the spatial distribution of liquid and ice particles can substantially alter cloud lifetimes by altering the Wegener-Bergeron-Findeison (WBF) process rates, whereby ice particles grow at the expense of liquid droplets due to differences in the saturation vapor pressures of liquid and ice. In fact, Tan & Storelvmo (2016) showed that for one prominent climate model, the homogeneously mixed assumption results in unrealistically high glaciation rates, and also variability in WBF process rates accounts for the most variability in mixed phase properties compared with other relevant mixed phase processes. Efforts must be made to observationally constrain phase spatial heterogeneity to improve the representation of clouds in both low and high resolution models.

1.3. Ice initiation mechanisms

In order to adequately represent phase frequencies over the Southern Ocean, multiple ice initiation mechanisms must be accounted for. Ice initiation occurs through primary nucleation or secondary ice production, and it is crucial to account for both processes to adequately represent phase partitioning in both low- and high- resolution models. Primary nucleation is characterized by the transition of vapor to ice, or of liquid to ice, and can be characterized as either homogeneous or heterogeneous nucleation.

Heterogeneous nucleation involves an aerosol to aid in the nucleation event, whereas homogeneous nucleation is the direct transition of vapor or liquid to the ice phase. Such aerosols are commonly referred to as ice nucleating particles (INPs). Heterogeneous nucleation occurs from -40° to 0°C, whereas homogeneous nucleation occurs once temperatures drop below approximately -40°C. The pristine conditions over the Southern Ocean have been found to contain relatively low INP concentrations (McCluskey et al., 2018), introducing uncertainty concerning the prevalence of heterogeneous ice nucleation over the region.

In contrast to primary nucleation, secondary ice production generates ice particles through varying particle interactions or unique processes, all of which require the pre-existence of liquid or ice. The most commonly evaluated mechanism is the Hallet-Mossop process, where irregularly shaped edges of aggregates shed off of the ice particles (Hallett & Mossop, 1974) during the riming process. This process is found to be favorable in regions with high concentrations of large drops (diameter > 25 μm), which result in high accretion rates. Other mechanisms of ice multiplication vary from ice-ice collisions to droplet fragmentation, characterized as ice splinters ejecting from a droplet as it freezes (e.g., Korolev & Leisner, 2020). Observational studies are crucial to constrain prominent ice production methods in order to accurately represent phase frequencies and partitioning, as well as other microphysical properties of Southern Ocean clouds.

1.4. Clouds over the Tasmanian Passage

Recently, the Southern Ocean Clouds, Radiation, Aerosol Transport Experimental Study (SOCRATES) took place (15 January to 28 February, 2018) over the Australasia

sector of the Southern Ocean (McFarquhar et al., 2021), obtaining a wealth of in situ measurements from varying low-level cloud types. The campaign commonly sampled both single- and multi-layered clouds, which varied from multi-layered stratus to broken cumulus underlying and puncturing overlying stratus. Research flights often targeted clouds in the cold sector of midlatitude cyclones due to the aforementioned simulated errors in this region. Multiple cloud probes were deployed on the National Science Foundation/National Center for Atmospheric Research G-V aircraft used to collect the data, including an optical imaging probe which can derive cloud phase information based on particle sphericity. Instrumentation obtaining INP measurements as well as cloud condensation nuclei (CCN) concentrations were also deployed, which can aid in determining the efficacy of primary and secondary ice production mechanisms.

Figure 1 shows flight paths of the 15 research flights associated with SOCRATES, acquiring cloud measurements south of Hobart, Tasmania.
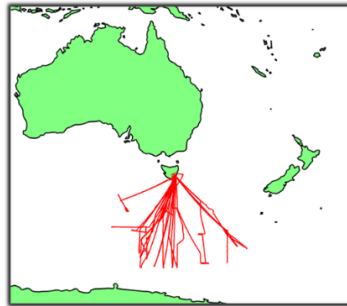
Figure 1: Flight tracks from the SOCRATES field campaign over the Tasmanian Passage. The aircraft was tasked with sampling both the marine boundary layer and the free troposphere, and flight paths alternated between level-leg and sawtooth sampling. The campaign provided a wealth of in situ observations which have sorely been needed towards improving our understanding of Southern Ocean clouds, including relevant ice initiation mechanisms and important processes influencing their microphysical properties

and lifetimes.

The objective of this dissertation is to utilize observations from SOCRATES and evaluate relevant properties of Southern Ocean clouds to aid in improving their representation in numerical weather prediction. Chapter 2 characterizes the observed phase frequencies, as well as introduces a novel method to quantify the degree of phase spatial heterogeneity over the region. Chapter 3 compares and contrasts the microphysical properties of single- and multi-layer clouds, and provides insight into the different physical, dynamic and thermodynamic features of the different cloud types. Additionally, phase frequencies are directly related to INP, CCN and large drop concentrations to examine the prevalence of primary and secondary ice production mechanisms. Chapter 4 explores a relatively unique and unexplored topic, namely, the impact of entrainment-mixing on mixed phase cloud properties. In a review paper summarizing the current field of mixed phase clouds, Korolev et al. (2017) states that "until now no studies on entrainment and mixing in mixed-phase clouds have been conducted." Little work has been done since, although Hoffmann (2020) found that ice particles can grow exceedingly large due to an enhanced WBF process resulting from entrainment using a millimeter resolution linear eddy model. This chapter explores whether there is observational evidence for this finding. Chapter 5 summarizes findings and provides concluding remarks from Chapters 2–4. Appendix A provides details of calculations used in Chapter 4, Appendix B provides supplementary figures from Chapters 2 and 3 and Appendix C lists pertinent terms.

2 Characterizing the occurrence and spatial heterogeneity of liquid, ice and mixed phase low-level clouds over the Southern Ocean using in situ observations acquired during SOCRATES

2.1. Introduction

Clouds over the Southern Ocean (SO) strongly influence the energy budget over this region, with satellite observations showing an annual mean spatial fraction around 80%–90% (e.g., Kay et al., 2012; Matus & L'Ecuyer, 2017; McCoy et al., 2014). Climate models struggle to correctly simulate radiative fluxes over the Southern Ocean (50–80°S), commonly underestimating reflected shortwave radiation in part because they (e.g., Bodas-Salcedo et al., 2016; Cesana & Chepfer, 2013; Kay et al., 2016; Trenberth & Fasullo, 2010; Wang et al., 2018) produce lower cloud fraction and less supercooled liquid water (SLW, liquid water at temperatures below 0°C) than observed. Similar problems have been noted in output from higher-resolution models (e.g., Huang et al. 2014, 2015; Naud et al. 2014).

Supercooled liquid water (SLW) plays a critical role in determining cloud radiative forcing (e.g., Ceppi et al., 2014; Lawson & Gettelman, 2014; Shupe & Intrieri, 2004), cloud feedbacks (e.g., Gettelman & Sherwood, 2016; Tsushima et al., 2006), and equilibrium climate sensitivity (e.g., Frey & Kay, 2017; Tan et al., 2016). A negative cloud phase feedback resulting from the transition of ice to liquid under surface heating was first proposed by Mitchell et al. (1989). Additional considerations must be made for mixed phase clouds by characterizing the mass fractions and spatial distribution of ice and liquid phases, as well as their degree of mixing, which can substantially impact the radiation budget (e.g., Sun & Shine, 1994; McFarquhar & Cober, 2004). Commonly

referred to as the Wegener–Bergeron–Findeisen (WBF) process, ice particles grow at the expense of neighboring SLW droplets given that the equilibrium water vapor pressure with respect to liquid is greater than that with respect to ice (Bergeron, 1928, 1935; Findeisen, 1938, 1940; Wegener, 1911). Several microphysical and dynamical mechanisms have been introduced to describe mixed phase clouds and their evolution (e.g., Korolev & Field, 2008; Jackson et al., 2012; Korolev et al., 2017; Kreidenweis et al., 2018). However, considerable work is required to constrain such mechanisms and further improve the understanding of these clouds. For example, although mixed phase clouds are thermodynamically unstable due to the differences in the saturation vapor pressures of liquid and ice, they are commonly observed to persist for hours or even days in the high latitudes (e.g., Morrison et al., 2011; Verlinde et al., 2007).

The spatial distribution of liquid and ice particles can have major impacts on the WBF process (Korolev & Isaac, 2006; Korolev et al., 2003). Further, the relatively coarse spatial resolutions of climate models require smaller scale/subgrid cloud heterogeneities to be parameterized. Differences in these parameterizations can significantly impact simulated cloud lifetimes and microphysical properties (e.g., Storelvmo et al., 2008; Zhang et al., 2019). Previous studies have examined the spatial heterogeneity of cloud phase at different locations (e.g., Chylek et al., 2006; Field et al., 2004; McFarquhar et al., 2007a; Stubenrauch et al., 1999) including the Southern Ocean (D'Alessandro et al., 2019; Zaremba et al., 2020). However, most of these studies merely comment qualitatively on observed heterogeneity from time series and vertical cross sections. Improved characterizations of phase spatial heterogeneity are crucially needed to provide clear and definite results for the evaluation of model simulations. This study uses in situ

observations from the 2018 Southern Ocean Clouds, Radiation, Aerosol Transport Experimental Study (SOCRATES) to characterize the frequency and spatial distributions of cloud phases over the SO. Section 1.2 introduces the in situ instrumentation and data processing techniques, Section 1.3 presents the findings, Section 1.4 provides further interpretation of the results, and Section 1.5 summarizes the key findings.

2.2. Dataset and experimental setup

2.2.1. In situ observations

This study uses 1-Hz airborne measurements collected from the National Science Foundation (NSF)/National Center for Atmospheric Research (NCAR) Gulfstream-V (GV) research aircraft during SOCRATES. SOCRATES was based out of Hobart, Tasmania and took place from 15 January to 28 February 2018, sampling over the Southern Ocean from 42° to 62°S and from 133° to 163°W. Fifteen research flights were conducted during SOCRATES. The aircraft primarily targeted cold sector boundary layer clouds. Flight plans were designed to ideally sample 10-minute level legs above cloud, in cloud, and below cloud, followed by sawtooth legs to obtain vertical profiles. Additional details on flight objectives and analyses can be found in Section 1.4 and in McFarquhar et al. (2021). Observations are restricted to temperatures less than 0°C to exclude warm clouds (i.e., clouds with no ice or SLW), so that approximately 14 hours (7,680 km) of in-cloud data between -40° and 0°C were available for analysis. The flights during SOCRATES primarily sampled the cold sector of cyclones with some passes through frontal systems, mostly associated with strong westerly flow over the Southern Ocean (McFarquhar et al., 2021). These synoptic-scale conditions coupled with a cool ocean surface led to cloud cover commonly observed over the SOCRATES flight domain,

including many cases of low-level and midlevel stratus and stratocumulus. Multilayer stratus and single-layer stratocumulus were frequently observed in several flights. Temperature was measured using a fast-response Rosemount temperature probe; for steady conditions the estimated accuracy and precision are 0.3K and 0.01K, respectively. Table 1 includes information of all the instrumentation used in this study, all of which are introduced and discussed further below.

	Instrument	Measurement	Uncertainties	Manufacturer
Bulk cloud properties	Cloud droplet probe (CDP)	size distribution (2-50μm)	Uncertain size distribution of non-spherical particles	DMT
	Two-dimensional Stereo probe (2DS)	size distribution (10-1280μm)	Highly uncertain depth of field at D<50μm	SPEC, Inc.
	Rosemount Icing Detector (RICE)	presence of SLW	Theoretical threshold liquid water content limit of ~0.025 $g\,m^{-3}$ or less	Rosemount
	KING probe	liquid water content	Underestimates liquid water content in presence of drizzle	DMT
Additional instrumentation	Rosemount temperature probe	temperature	Accuracy of 0.3 K Precision 0.01 K	Rosemount
	Radome gust probe, inertial system, and GPS	vertical air speed	Net uncertainty of 0.12 m s^{-1} (likely higher uncertainty for SOCRATES)	–
	25-Hz Vertical Cavity Surface Emitting Laser (VCSEL) hygrometer	water vapor	Accuracy of ~6% Precision of 1%	Southwest Sciences Inc.

Table 1: A list of all instrumentation and relevant information used in this study. Sources related to uncertainties are contained within Section 1.2.

A suite of cloud probes was installed on the G-V. Probes for measuring size distributions included a 2-Dimensional Stereo probe (2DS, manufactured by SPEC, Inc.), a 2-Dimensional Cloud probe (2DC, a Particle Measuring Systems instrument, modified for fast response), a Precipitation Imaging Probe (PIP, manufactured by Droplet Measuring Techniques, DMT), a Particle Habit Imaging and Polar Scattering probe (PHIPS HALO) and a DMT Cloud Droplet Probe (CDP). Second-by-second comparison

of the size distributions of the 2DC and 2DS showed marked differences between probes. Examination of particle images showed degraded 2DC image quality occurred for more than half of the flight hours due to fogging, and hence these data were unusable. A problem with the time record on the PIP prevented use of the PIP image data, and hence information about the size distributions of large particles was not available. Thus, the base size distributions were characterized by a combination of the CDP and 2DS data. Data from the CDP were used to characterize particles with maximum dimension (hereafter size D) ranging from 2 to 50 μm. Although the 2DS can nominally detect particles with D ranging from 10 to 1280 μm, only particles having maximum dimensions (D_{2DS}) greater than or equal to 50 μm were used because of a small and highly uncertain depth of field for $D_{2DS} < 50$ μm (e.g., Baumgardner & Korolev, 1997). The SOCRATES 2DS size distributions and particle morphological data (Wu & McFarquhar, 2019) were determined using the University of Illinois/Oklahoma Optical Probe Processing Software (UIOOPS, McFarquhar et al., 2017, 2018), and include corrections for removal of shattered artifacts (Field et al., 2003; Field et al., 2006). Mass distribution functions are determined using the habit-dependent mass-size relationships summarized by Jackson et al. (2012, 2014) for the different particle habits that are identified in UIOOPS (McFarquhar et al., 2018) following a modified Holroyd (1987) approach.

A 1-s sample is identified as in-cloud if either of the following two conditions is met: 1) CDP measurements reporting mass concentration (M_{CDP}) greater than 10^{-3} g m^{-3} where M_{CDP} is estimated from the size distributions assuming all particles are spherical water droplets, or 2) 2DS measurements report number concentrations of at least one particle having $D_{2DS} > 50$ μm (N_{2DS}). The rest of the time periods are defined as outside

11

of cloud. Although this definition of cloud allows for thinner and more tenuous cloud than previous studies that assumed mass thresholds of 0.01 g m^{-3} for identifying cloud (e.g., McFarquhar et al., 2007a), it allows thin layers at lower temperatures to be included in the analysis. Further, although M_{CDP} is not a well-defined quantity for ice clouds as forward scattering probes assume Mie theory and spherical particles in their sizing and the CDP does not properly sample non-spherical particles (McFarquhar et al., 2007b), a threshold based on M_{CDP} was chosen to eliminate sea spray (and other large aerosols) as confirmed by comparing time series with images from the forward-facing camera, which reported encounters with sea spray. The CDP threshold was also chosen by evaluating a joint frequency distribution controlled by mass and number concentrations (Figure A in supplementary material) and finding a significant bimodality, by which the modes are separated by M_{CDP} greater than and less than the threshold chosen, consistent with inspection of time series and the forward-facing camera of in-cloud samples and sea spray.

Liquid water was sampled by two instruments, a Rosemount icing detector (RICE), and a King-style hot wire instrument (KING; King et al. 1978, manufactured by Droplet Measurement Technologies (DMT)). The presence of small amounts of SLW can be ascertained from the Rosemount Icing Detector (RICE). The RICE is a metal protrusion which vibrates at a constant frequency; if supercooled droplets collide with it, the droplets freeze and alter the frequency of the vibrating rod. The output is translated into a voltage signal, which increases as more, or decreases as less (e.g., by sublimation) ice accumulates on the protrusion. The theoretical performance of the RICE is described in Mazin et al. (2001). The response of the instrument is dependent on airspeed, air

density, and humidity as well as the sizes of droplets, as large drops may splash upon hitting the probe and be undetected. Mazin et al. (2001; Figure 4a) suggest a theoretical threshold liquid water content limit of ~0.025 g m^{-3} or less at conditions similar to those sampled in this study; however, the response to liquid water may vary from probe-to-probe, requiring independent calibration for quantitative results. During the lower-level cloud conditions in SOCRATES, droplets were found to not freeze on the RICE protrusion for temperatures greater than -5°C due to dynamic heating of the sensor. Further, data are not usable during the reheating cycle of the RICE that removes the frozen particles accumulated on the wire (e.g., Mazin et al., 2001), which are shown in Figure 2C where dV/dt<0 V s^{-1}. Thus, the RICE offers an independent detection of SLW conditions, but is not used here as a stand-alone quantitative measure of supercooled water concentrations. Sensitivity tests were performed to determine the best method to discern the cloud phase using the RICE probe in combination with data obtained from other probes, as discussed in the next section.

For results examining the characterization of mixed phase microphysical properties (Section 3.2), the KING probe was utilized. King et al. (1978) report a sensitivity of 0.02 g m^{-3}, a response time of better than 0.05 s and an accuracy of 5% at 1 g m^{-3}, but these parameters can vary depending on flight speed as discussed in McFarquhar et al. (2017) and Baumgardner et al. (2017). Similar to the RICE probe, the KING probe responds to smaller liquid droplets (e.g., volume-weighted mean diameter less than 0.15 mm as reported by Biter et al. (1987)) so it underestimates SLW in the presence of supercooled drizzle (e.g., Schwarzenboeck et al. 2009), but also can overestimate SLW in the presence of ice (Cober et al., 2001). Thus, the KING probe is

best for measuring the liquid water contents in the presence of exclusively smaller drops, while estimates of SLW content in the presence of drizzle are best obtained by integrating the size distributions. Water vapor is measured using the 25-Hz Vertical Cavity Surface Emitting Laser (VCSEL) hygrometer (Zondlo et al., 2010), which has an accuracy and precision of ~6% and ≤1%, respectively. The calculation of relative humidity with respect to ice (RHi) is based on Murphy & Koop (2005). For temperatures from -40° to 0°C, the uncertainties in RHi range from 6% to 8%. Vertical velocity (w) is measured using the Radome Gust Probe in combination with pitot tubes and the differential Global Positioning System, where Cooper et al. (2016) report a net uncertainty in the standard measurement of vertical wind of 0.12 m s^{-1}, although this represents ideal sampling conditions. More information on the performance of the GV gust probe processing and other instrumentation performance is provided in the manager's report (EOL, 2018). The report describes methods that were used to correct for drift with altitude in the system, which likely increases the uncertainty, especially over the whole range of altitudes in SOCRATES (although the performance at constant altitudes should be steady). Further research on the performance of the system is planned to better document these uncertainties. The project manager's report also provides additional information on the processing and data quality issues related to the other routine instruments.

2.2.2. Dataset and experimental design

Figure 2A shows normalized frequency distributions of the RICE change in voltage (dV/dt) for different ranges of number concentrations from the CDP (N_{CDP}). Greater voltage changes are associated with greater liquid mass. Results show changes in voltage are positively skewed and noticeably greater for $N_{CDP} \geq 1$ cm^{-3}, suggesting that high N_{CDP}

are generally liquid samples. This is consistent with previous studies (e.g., Lance et al., 2010; Heymsfield et al., 2011; Finlon et al., 2019) which have noted that a threshold in CDP concentrations can serve as a first estimate for the presence of SLW in the absence of information from other probes.
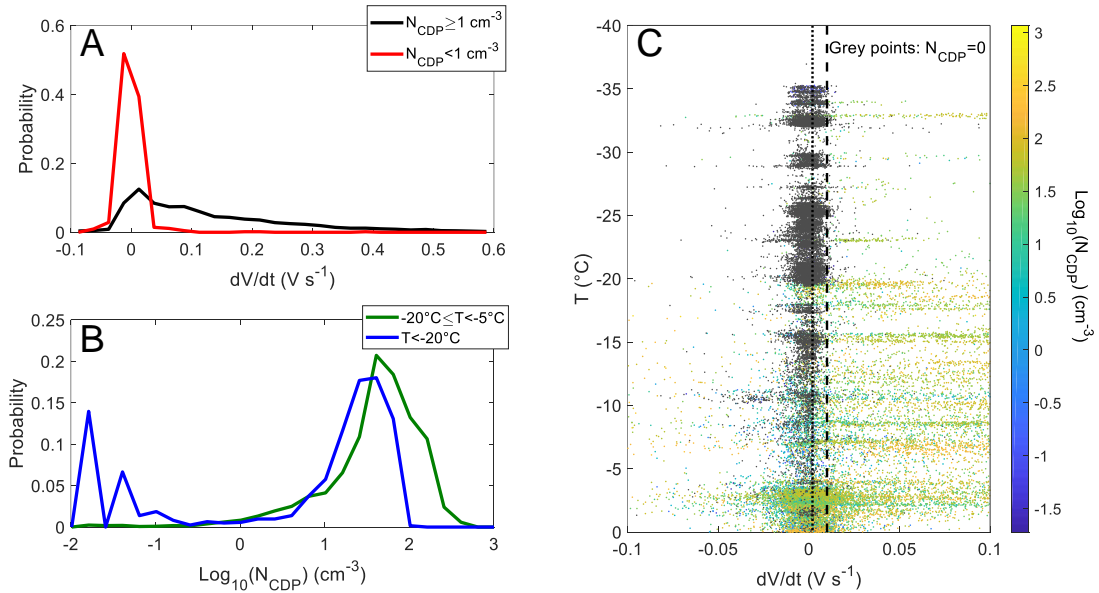
Figure 2: Normalized occurrence frequency of dV/dt (dt=1 second) of RICE for $N_{CDP} \geq 1$ cm^{-3} and $N_{CDP} < 1$ cm^{-3} (A), as well as for N_{CDP} at temperatures from -20° to -5°C and less than -20°C (B). Vertical profile of dV/dt colored by N_{CDP} (C). Samples in 1A,B are all considered in-cloud for CDP (i.e., $M_{CDP} \geq 10^{-3}$ g m^{-3}) and in 1C for CDP or 2DS ($M_{CDP} \geq 10^{-3}$ g m^{-3} or $N_{2DS} > 0$). The grey points in 1C represent in-cloud samples having $N_{CDP} = 0$. The dotted and dashed lines are at 0.002 V s^{-1} and 0.01 V s^{-1}, respectively.

Figure 2B shows a sharp bimodal distribution of N_{CDP} for temperatures less than -20˚C where more ice would be expected. Thus, a threshold value of $N_{CDP} \geq 1$ cm^{-3} is used to identify time periods where cloud particles with D < 50 μm are liquid. Examination of the CDP and RICE data confirmed that time periods with $N_{CDP} < 1$ cm^{-3} correspond to minimal voltage responses from RICE, further suggesting low N_{CDP} corresponds with ice phase observations. Figure 2C shows vertical profiles of the RICE dV/dt for all in-cloud samples acquired during SOCRATES with results colored by N_{CDP}. The dashed line at

0.01 V s^{-1} roughly intersects between datapoints where $N_{CDP}=0$ (grey points), and N_{CDP} >0 (colored points) over most of the vertical column. The dotted line at 0.002 V s^{-1}, based on a previously proposed threshold to infer the existence of liquid (Heymsfield & Miloshevich, 1989), shows that this threshold would overestimate the frequency of liquid based on the CDP measurements, especially those at low temperatures. Thus, results presented here suggest a 0.01 V s^{-1} threshold is less susceptible to overestimating the frequency of liquid (for example, the large number of samples >0.002 V s^{-1} at temperatures less than -20°C where $N_{CDP}=0$ cm^{-3}).

The phase of the 2DS particles with D_{2DS}>50 um is calculated using multinomial logistic regression (MLR), which models nominal outcome variables. Logistic regression is commonly accepted as a successful method for classification (e.g., Bishop, 2006). Specifically, MLR produces the logarithmic odds of outcomes modeled as a linear combination of the predictor variables. Previously, this method was used to derive the habits of ice crystals from two-dimensional particle images using multiple optical array probes, including the 2DS (Praz et al., 2018). The 2DS provides two-dimensional particle imagery, of which 1362 s worth of particles with $D_{2DS} > 50$ μm were visually inspected and classified as either liquid, mixed or ice phase (i.e., the training set). Spherical particle images are assumed to be liquid drops whereas all other particles are assumed to be ice particles. The predictor variables used in MLR were M_{2DS}, N_{2DS}, number-weighted mean D_{2DS} (Mean D_{2DS}), standard deviation of D_{2DS} (σ_{D_2DS}), standard deviation of number concentrations in 10 μm bins (σ_{N_2DS}), the maximum particle D_{2DS} (Max D_{2DS}) and N_{CDP}. Since the presence of smaller cloud droplets (D<50 μm) was found to be a successful proxy for larger supercooled droplets (D'Alessandro et al., 2019; Finlon et al., 2019;

Heymsfield et al., 2011), N_{CDP} was included as a predictor in the MLR. The phase having the highest likelihood of the three as determined by the MLR is selected. Additional visual inspection of a separate 1287 s worth of 2DS imagery was performed following the MLR analysis in order to evaluate its success (i.e., the validation set). A decision tree similar to that used for the 2DC in D'Alessandro et al. (2019) was developed for the 2DS and compared with results from the MLR as a baseline model. The Heidke skill score gives an indication of a prediction's success, where values approaching one indicate improving predictions and a value of 0 indicates the prediction performs as well as a randomized dataset. It was calculated as a multi-category forecast (one phase per category), of which further information of can be found in Jolliffe & Stephenson (2011). The MLR classification was found to perform well, as highlighted by Heidke skill scores of 0.88 and 0.68 for the MLR and baseline datasets, respectively. The phase classification was manually corrected for the "missed" predictions, including an additional 751 samples from further visual inspection of 2DS images showing spherical particles where neither the RICE nor CDP was flagged as liquid. The use of RICE and CDP as proxy data for the phase of particles having D>50 μm is believed to improve upon the MLR phase classification, as distributions of RHi for these cases center around 100%, most notably at temperatures less than -20°C (Figure B in supplementary material). A flow chart highlighting phase categorization using the RICE, CDP and 2DS is shown in Figure 3.
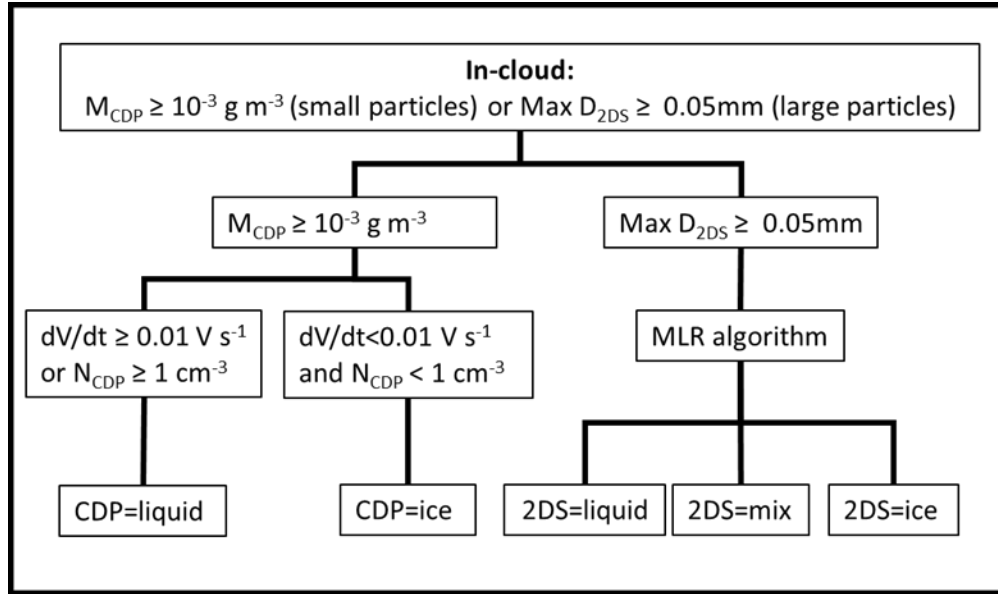
Figure 3: Flow chart highlighting how phase is determined using the CDP, RICE and 2DS probes. The phase is reported for every second, whereby the combination of CDP and 2DS phases determines the phase at every second (e.g., CDP=liquid and Max D_{2DS}<0.05 mm is classified as liquid, CDP=liquid and 2DS=ice is classified as mixed phase, etc.).

The phase is determined separately for cloud particles having $D < 50$ μm (CDP and RICE) and $D > 50$ μm (2DS). Thus, a sample is liquid when liquid is only reported for all particle sizes, and similarly for ice. A sample is mixed phase when both liquid and ice are reported. Cloud phase is determined every second, amounting to horizontal spatial resolutions of ~150 m depending on the aircraft flight speed.

A time series including 2DS images and cloud phase classification results is shown in Figure 4. Examples of images for all three phases are shown underlying the time series, where the images correspond with the overlying boxes. The top two rows show temperature, particle size distribution statistics from the 2DS (Max D_{2DS} and Mean D_{2DS}) and N_{CDP}. The third row shows particle mass distribution functions from the 2DS over all available bin sizes and the fourth row shows cloud phase results. For the liquid case, Max D_{2DS} reveals that SLW drops can often have $D > 0.3$ mm, consistent with

18

observations that drizzle is sometimes present in low-level cloud regimes.
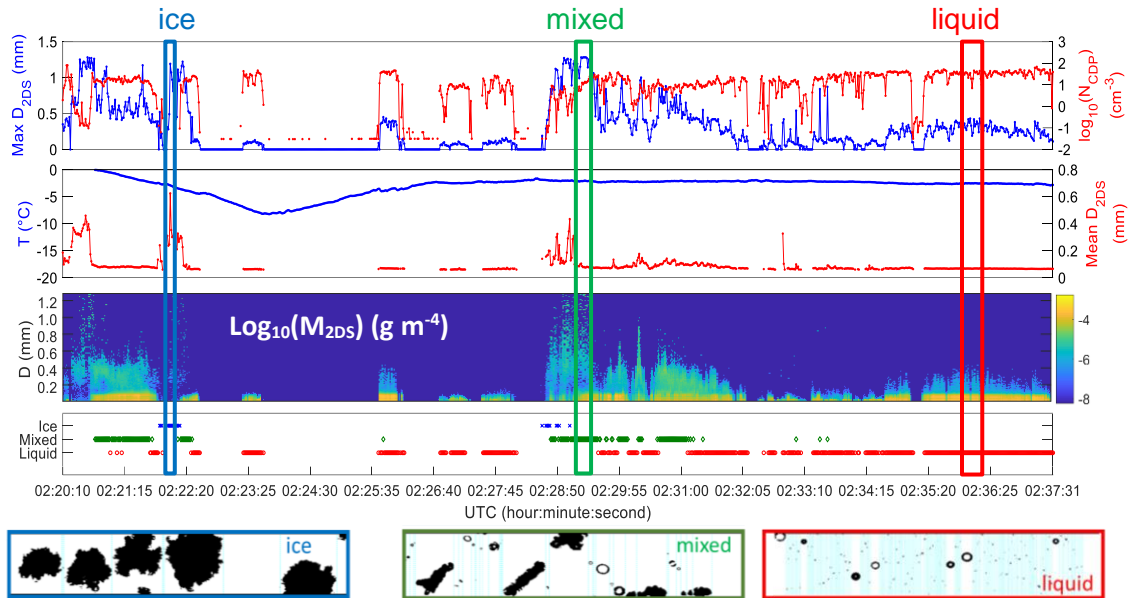
Figure 4: Time series from RF06 showing Max D_{2DS} and N_{CDP} (top row), temperature and number weighted mean D_{2DS} (2nd row), the mass size distribution normalized by bin width (3rd) and the phase derived from the phase algorithm in Figure 3 (bottom row). The red, green and blue boxes correspond with underlying 2DS optical array imagery of liquid, mixed and ice phase samples, respectively.

Mean D_{2DS} is exceptionally low (typically less than 0.2 mm), due to the vast majority of droplets having relatively small D_{2DS}. This is similarly observed for the mixed phase case, although in contrast Max D_{2DS} far exceeds the sizes of supercooled drizzle drops due to the large ice particles observed that may preferentially grow due to riming or the larger supersaturation over ice compared to water. The ice phase case similarly has large Max D_{2DS}, and in contrast to the liquid and mixed phase case has much larger Mean D_{2DS}, since there is no longer a large concentration of smaller liquid drizzle particles. These variations in 2DS particle statistics highlight how the listed statistical parameters can be used to derive the phase of larger particles ($D > 50\mu m$). Similarly, large segments of the mass distribution functions are relatively homogeneous, highlighting relatively static microphysical properties over short durations of observations having similar phase.

19

2.3. Results

2.3.1. Cloud phase frequency distributions

The relative frequency distribution of cloud phase as a function of temperature is shown in Figure 5. Cloud samples are primarily liquid phase at the highest temperatures, and ice phase at the lowest temperatures.
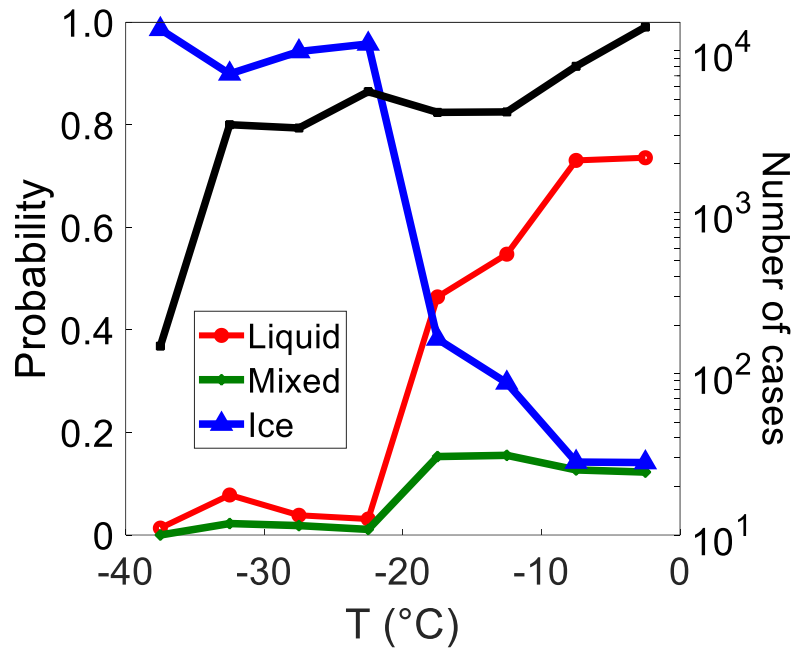
Figure 5: The relative frequency distribution of liquid, mixed and ice phase samples are shown as the colored lines, whereas the number of in-cloud samples from the SOCRATES campaign is shown by the black line. Results are binned at 5°C intervals.

Mixed phase samples are the most infrequent, which may be expected since the mixed phase is thermodynamically unstable. In fact, previous analyses have shown that mixed phase clouds, where the fraction of liquid water content to total water content is between 0.1 and 0.9, are not common (e.g., Korolev et al., 2003). This may also be related to the inability to discern the coexistence of ice and liquid particles having diameters less than 50 (due to CDP and RICE limitations) to 100 μm (due to coarse resolution of relatively small particles in 2DS particle imagery), which might result in an underestimation of mixed phase

samples. Interestingly, ice-only observations were observed at temperatures greater than -5°C, and SLW was observed at temperatures near -35°C. Samples of ice at these high temperatures were often observed as precipitating ice particles below the cloud base, which may have originated at colder temperatures. Further, there appears to be a sharp decrease in the frequency of the liquid phase once temperatures drop below -20°, suggesting the possibility of ice nucleating particles being activated at these temperatures; conversely, there is a sharp increase in the frequency of the ice phase at these low temperatures. Below a temperature of -20°C, liquid phase samples are present, but relatively sparse. Approximately 500 CDP and RICE samples meet the conditions for SLW occurrence at temperatures less than -30°C, with the lowest temperatures dropping a few tenths of a degree below -35°C. Visual inspection of the images confirmed that these samples were indeed liquid, with these liquid clouds typically being sampled during the high altitude transit legs of the GV.

2.3.2. Mixed phase characterization

Figure 6 shows the normalized occurrence frequency of liquid water fraction within clouds identified as mixed phase for different temperature ranges, where the liquid fraction is the liquid content (LWC) divided by the total condensed water content (TWC). LWC and ice water content (IWC) are determined using LWC_{KING} and M_{2DS}, respectively. Sensitivity tests relating LWC_{KING} to M_{CDP} were found to be highly correlated for $N_{CDP} > 5$ cm^{-3} (Figure C in supplementary material). Previous studies have shown a clear U-shaped distribution of liquid water fraction for in-cloud samples within the temperature range focused on in this study (e.g., Korolev et al., 2003; D'Alessandro et al., 2019).
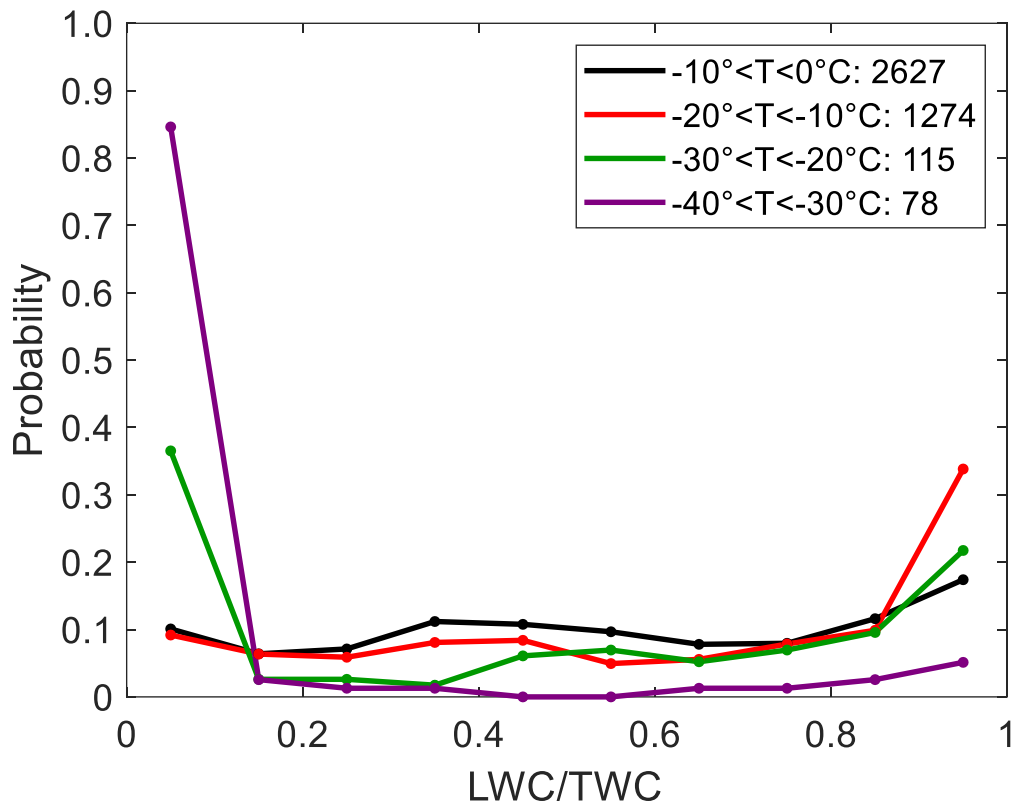
Figure 6: Normalized frequency distributions of liquid to total condensate mass ratio for SOCRATES. Results are only shown for mixed phase cases. Different colored lines correspond with different temperature regimes. The number of samples for each temperature regime is provided in the legend.

However, results here are only shown for mixed phase samples, which show a reasonable number of samples from 0.1<LWC/TWC<0.9, producing relatively uniform distributions. This is consistent with the nature of mixed phase conditions observed over this region, whereby few and large ice aggregates are surrounded by swaths of SLW, which are evidently not depleted significantly by the occasional ice particle. Results show a maximum frequency at LWC/TWC>0.9 for the highest temperatures (-20° to 0°C) and a maximum frequency at LWC/TWC<0.1 for the lowest temperatures (-40° to -20°C). Interestingly, the LWC/TWC at -10° to 0°C is the most uniformly distributed compared

to other temperature regimes, whereby the frequency at LWC/TWC>0.9 is lower for this regime (~0.18) compared with that from -20° to -10°C and -30° to -20°C (~0.35 and ~0.22, respectively).

Figure 7 shows multiple microphysical properties sorted by LWC/TWC for only those samples identified as mixed phase, whereby moving right to left along the respective abscissas corresponds to more glaciated conditions.
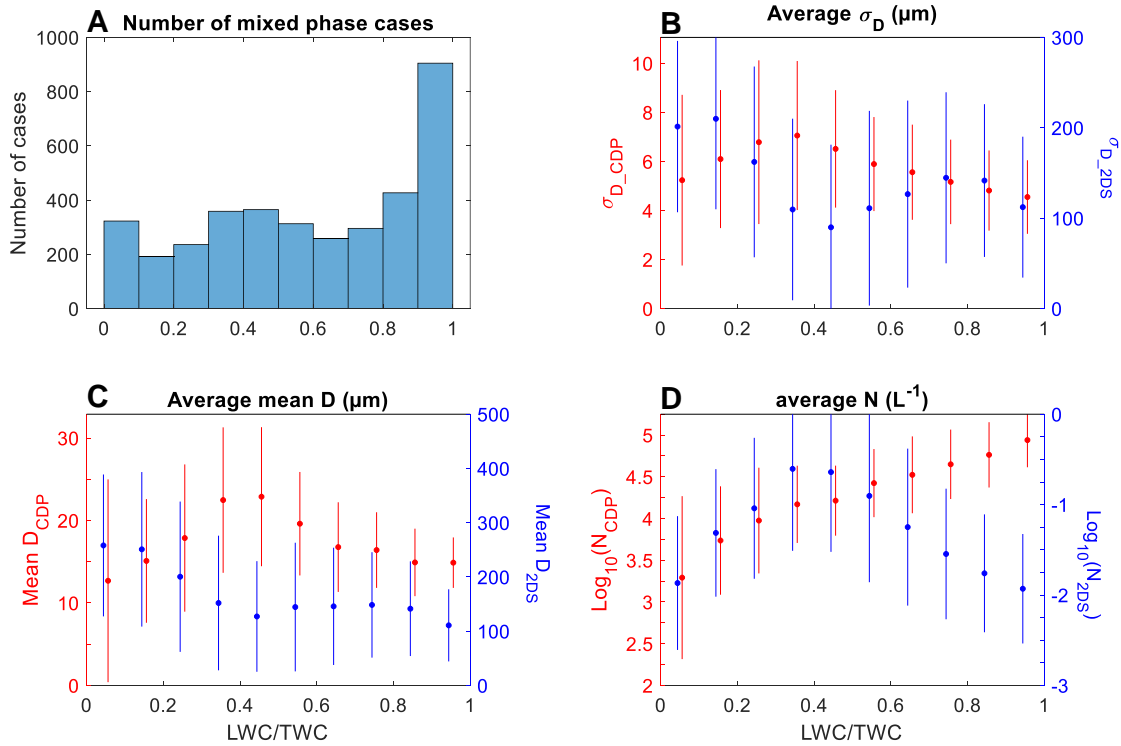
Figure 7: Number of 1 second samples for analysis (A). The mean values of σ_D (B), number weighted mean D (C) and N (D) of CDP and 2DS observations controlled by LWC/TWC. Colored lines represent one standard deviation. Results are shown for the CDP (2DS) in red (blue) and are primarily representative of liquid (ice) particles. Results are restricted to mixed phase samples where CDP is classified as liquid.

The parameters in red correspond with CDP measurements and those in blue correspond with 2DS measurements, which generally correspond to liquid and ice phase observations, respectively. Further, mixed phase samples are restricted to those having

23

CDP meet the definition of liquid as shown in Figure 3, which amounts to ~97% of all mixed phase samples. Figure 7A is a histogram of the LWC/TWC samples binned at intervals of 0.1. There is a slight peak at LWC/TWC<0.1 and the largest peak is at LWC/TWC>0.9, however, the distribution is relatively uniform.

Focusing on liquid microphysical properties, σ_{D_CDP} and Mean D_{CDP} increase with LWC/TWC until LWC/TWC reaches about 0.4, and then subsequently decrease (Figure 7B,C). Noting that N_{CDP} also increases with LWC/TWC (Figure 7D), this is consistent with smaller droplets preferentially evaporating during the WBF process, as LWC is reduced by transfer to the ice phase. This may be expected as a volume of smaller droplets has a greater total surface area relative to a volume of larger droplets having an equivalent liquid mass content. For ice phase properties, N_{2DS} slightly increases with decreasing LWC/TWC for LWC/TWC > 0.4, whereas mean D_{2DS} is relatively constant and begins to increase with decreasing LWC/TWC when LWC/TWC < 0.4. Further, N_{2DS} decreases with decreasing LWC/TWC when LWC/TWC<0.4. Examination of 2DS particle size distributions and particle imagery show drizzle drops are often collocated at LWC/TWC>0.4, and the number of drizzle drops decreases as LWC/TWC decreases below 0.4. Because of this, caution must be taken when interpreting the 2DS results, as there may still be an overlap of ice and liquid particles.

2.3.3. Cloud phase spatial heterogeneity

An additional goal of this study is to describe the phase spatial heterogeneity within low-level Southern Ocean cloud regimes. A novel quantitative approach to describe spatial heterogeneity is developed here. Figure 8A provides a visualization of three terms that are introduced to aid in the phase heterogeneity analysis. A sample has a time resolution

of one second (~150 m). A segment is defined as a set of samples whose neighboring samples all have the same phase.
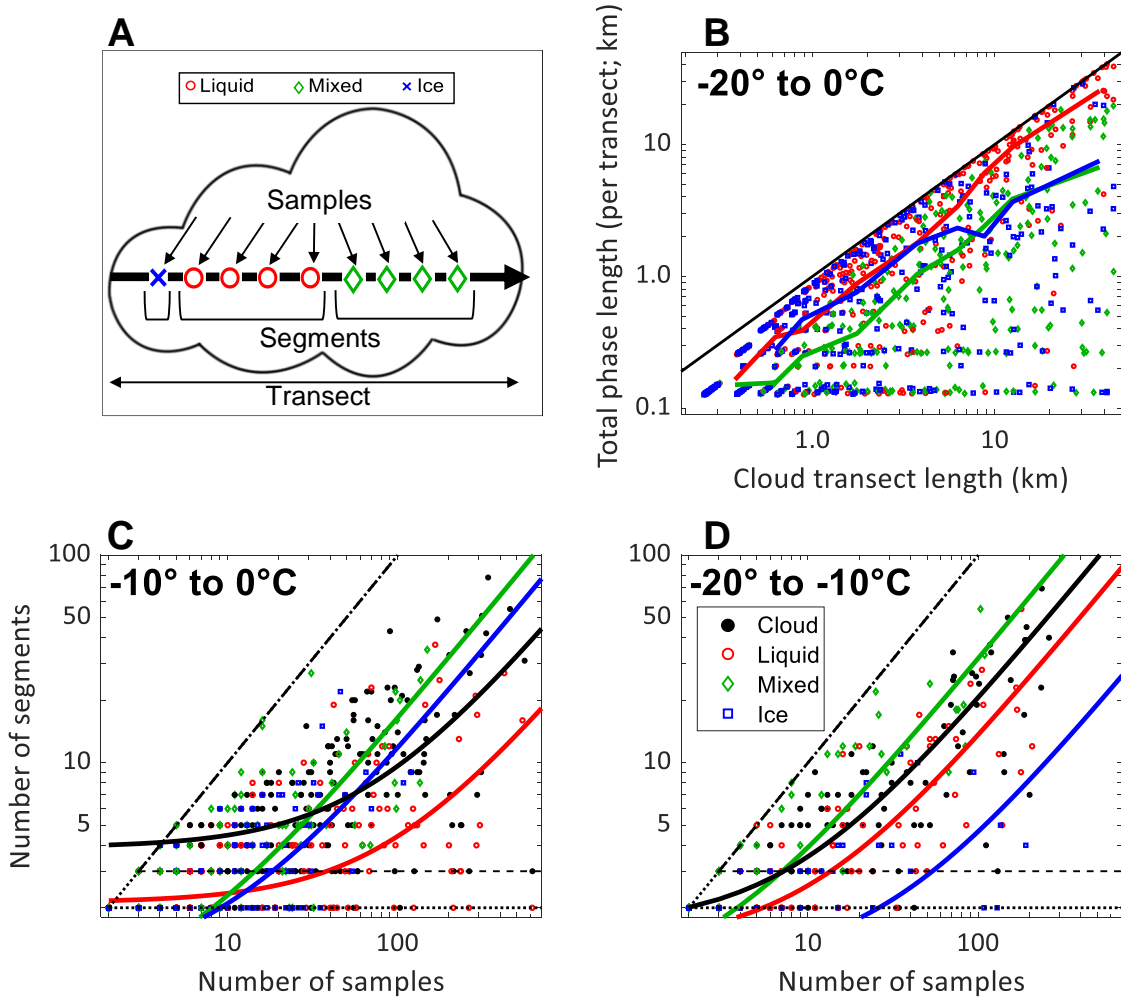
Figure 8: An idealized diagram highlighting the introduced terms "samples", "segments" and "transects" (A), a scatter plot of the cloud transect length versus the total length of the respective phases (colored markers) contained within the transects (B) and the number of samples of a cloud transect (black dots) and phase contained within a cloud transect (colored markers) versus the respective number of segments (C,D). Results in 8B,C,D are restricted to temperature ranges shown in their respective panels, and cloud transects containing at least two phases. Colored lines in 8B show average phase lengths. The lines in 8C,D are best fit linear regressions for the respective phases (colored lines) and entire cloud transects (black line). The black line in 8B shows the one-to-one line. The dotted (dashed) line in 8C,D represents the minimal possible heterogeneity for cloud transects containing two (three) phases. The dotted dashed line represents a completely heterogeneous cloud (i.e., the number of samples equals the number of segments). The markers in 8B,C correspond with those shown in the legend of 8D.

A transect is defined as the total length of the cloud sampled (i.e., a set of consecutive in-cloud samples or segments with no clear air between). Utilizing these terms allows the spatial heterogeneity to be quantified by directly relating the number of samples to segments within a transect. Namely, a cloud with a greater number of segments will be more spatially heterogeneous than one with fewer segments, given similar transect lengths. Further, a completely heterogeneous cloud would have the same number of samples as segments, as the phase would change along the flight path at every second. In contrast, heterogeneity is minimized by having the minimum number of segments possible (i.e., one segment for a cloud with one phase, two segments for a cloud with two phases and three segments for a cloud with three phases). The visualization in Figure 8A is an example of a cloud transect having the minimal amount of heterogeneity, since only three segments are observed in the transect containing three phases. Increasing the number of segments would increase its spatial heterogeneity. The heterogeneity would be maximized if every sample was a different phase from its neighboring sample(s).

Figure 8B shows the length of cloud transects (derived from the true aircraft speed) related to the total length of each phase contained within the cloud transects. The results are restricted to -20°–0°C in order to focus on boundary layer clouds; and in any event, ice phase samples dominate lower temperatures. The number (percentage) of one phase transects between -20° and 0°C having at least five samples was 268 (39%), 1 (~0%), and 54 (~8%) for liquid, mixed, and ice phase conditions, respectively. For transects containing at least two phases, 369 (53%) were observed between the same temperatures. At temperatures between -40° and -20°C, 73% were one phase transects containing ice and 23% contained at least two phases. Figure 8B does not include one

phase transects, as the markers would lie directly on the one-to-one line (black line). The colored lines show average phase lengths as a function of the cloud transect length. For all transect lengths, the total length of liquid phase samples is greater than the lengths of mixed phase samples and nearly equal to or greater than the lengths of ice phase samples, as the red line is closest to the one-to-one line. This is consistent with the relative frequency distributions in Figure 5. The lengths of the ice phase samples are relatively close to those of the liquid phase samples for transect lengths less than ~4 km and closer to those of the mixed phase samples at transect lengths greater than ~4 km. Overall, results reveal that the liquid phase is more frequent (i.e., has greater total lengths) than the ice phase for transects greater than 4 km but is equally frequent for transects less than 4 km. In addition, the mixed phase is less frequent than the ice phase for transects less than 4 km and less frequent than the liquid phase regardless of transect length, but is approximately as frequent as the ice phase for transects greater than ~5 km.

Figure 8C,D shows the number of segments within a cloud transect as a function of the number of samples within the transect as black dots, whereas the number of samples and segments for each phase contained within the cloud transects are given by the colored markers. Cloud transects with greater spatial heterogeneity are generally farther up the y-axis (i.e., clouds with a relatively large number of segments will approach the one-to-one line). Overall, the datapoints are relatively scattered for the cloud and phase samples, and the best fit linear regressions (black and colored lines for the cloud and phase markers, respectively) lie between the minimum (dotted and dashed lines) and maximum (dotted dashed line) heterogeneous values. This allows for an absolute measure of the relative heterogeneity between different phases. Figure 8C shows

results at temperatures between -10° and 0°C, which reveal the most spatially heterogeneous phase is the mixed phase, as the green lines have the greatest number of segments. In contrast, the least heterogeneous phase is the liquid phase, as the red lines have the least number of segments. Figure 8D shows results at temperatures between -20° and -10°C, revealing the most spatially heterogeneous phase is the mixed phase, whereas the least heterogeneous phase is the ice phase. When combining the two temperature regimes, the most heterogeneous phase is the mixed phase and the least heterogeneous is the liquid phase (Figure D in supplementary material). Further, the best fit line for cloud transects is slightly lower at -10° to 0°C compared with -20° to -10°C, as seen by the relatively similar slopes beyond ~30 samples and the solid black lines intercepting the right ordinate at ~40 segments for the warmer regime and greater than 100 segments for colder temperatures. This suggests spatial heterogeneity increases with decreasing temperature from 0° to -20°C.

To determine a quantitative measure of heterogeneity, a parameter is developed to define the spatial heterogeneity, which is called the spatial heterogeneity score (SHS). The equation is simply a normalization equation described as:

$$\text{SHS}_n = \frac{\text{samples}_n - \text{segments}_n}{\text{samples}_n - 1} \qquad \qquad 1)$$

where n is substituted for cld when SHS is calculated for the entire transect (SHS_{cld}), and for liq, mix or ice when calculated for the respective phases contained within a given transect (SHS_{liq}, SHS_{mix}, SHS_{ice}). A more homogeneous cloud has SHS_{cld} approach one and a more heterogeneous cloud will have SHS_{cld} approach zero. Figure 9 shows histograms of SHS_{cld} and $\text{SHS}_{liq,mix,ice}$. The frequency of SHS_{cld} cases exceeding 0.5 far exceeds the frequency of cases less than 0.5, suggesting clouds over the Southern Ocean

28

are generally spatially homogeneous. Similarly, the frequencies of SHS_{liq} and SHS_{ice} exceeding 0.5 are much greater than those less than 0.5.
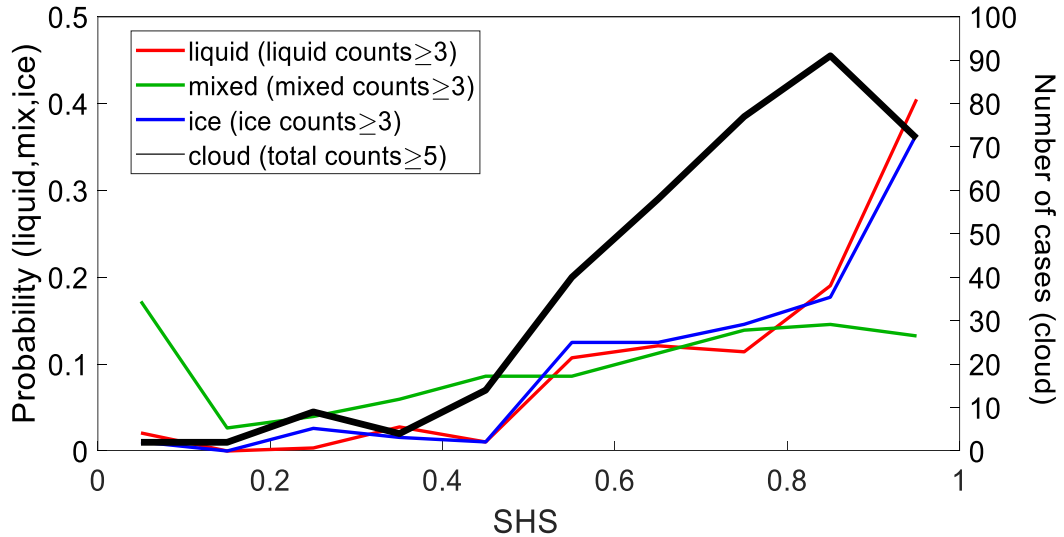
Figure 9: Histogram of SHS_{cld} (black line; right ordinate) and normalized frequency distributions of SHS_{liq}, SHS_{mix} and SHS_{ice} (colored lines; left ordinate). The results are restricted similar to Figure 8B, as well as limited for a given number of samples (shown in the legend).

In fact, nearly 50% of SHS_{liq} and SHS_{ice} are greater than 0.9. In contrast, SHS_{mix} is nearly a uniform distribution. This is consistent with Figure 8C,D, highlighting the greater degree of spatial heterogeneity of mixed phase samples. Note the frequency distribution of SHS_{cld} has a peak frequency between 0.8 and 0.9, which may seem to conflict with SHS_{liq} and SHS_{ice} having peak frequencies greater than 0.9 and SHS_{mix} having comparable peak frequencies between 0.8 and 1.0. However, values of SHS_{cld} are inherently more heterogeneous since they always contain at least two segments for cloud transects containing at least two phases. Following the normalization equation, a cloud transect with two segments would require a minimum of 12 samples to exceed 0.9 and 22 samples for a cloud transect with three segments to likewise exceed 0.9.

The linkage between meteorological and microphysical properties to the degree of

spatial heterogeneity is also investigated. An example of the analysis is shown in Figure 10 where the frequency distribution of SHS_{cld} depends on whether the sampled clouds were coupled or decoupled from the layer immediately above the ocean surface; previous studies (e.g., Wang et al., 2016; McFarquhar et al., 2021) have suggested the degree of coupling might affect cloud composition. Generally, potential temperature and moisture profiles are examined to determine coupling based on the relation between the lifting condensation level and the cloud base height. However, Wang et al. (2016) examined decoupling in subtropical environments by looking for discontinuities in vertical profiles of potential temperature, moisture content, and aerosol number concentrations. They developed a metric whereby environments are considered decoupled if the differences in the top and bottom of the subcloud layer (i.e., the cloud base and surface, respectively) potential temperature and water vapor mixing ratio exceed 1.0K and 0.6 g kg^{-1}, respectively. Otherwise, an environment is considered coupled. This metric is applied here using the nearest dropsonde profile to each cloud transect. Figure 10 shows that coupled and decoupled environments have similar distributions of SHS_{cld}, suggesting there is no relation between cloud phase heterogeneity and surface coupling.

A Whitney-Mann U-test and two-sample Kolmogorov-Smirnov test are performed on the two distributions to further evaluate their similarity. The Whitney-Mann U-test determines whether the median of one distribution is significantly greater or less than the other, whereas the two-sample Kolmogorov-Smirnov test determines the significance of the maximum absolute difference between the two cumulative frequency distributions, both of which use lookup tables. These tests are chosen since they do not require prior knowledge of the distributions' shapes. Results suggest there is no

statistically significant difference between the two distributions. Both tests do not reject the null hypothesis, namely, that the distributions are similar, at a significance level of 10%.
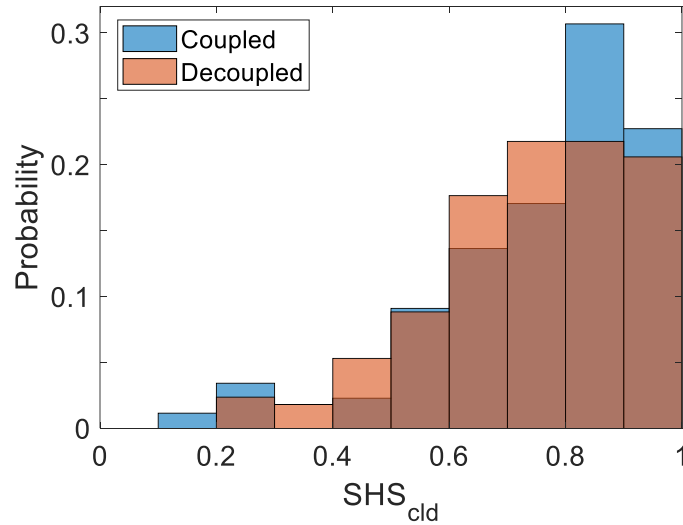
Figure 10: Normalized frequency distributions of SHS_{cld} for coupled and decoupled environments. SHS_{cld} are only shown for cloud transects with ≥ 5 samples as in Figure 9. Coupling is determined following Wang et al. (2016) whereby the nearest dropsonde to a given cloud transect is used.

Heterogeneity analyses are applied to other meteorological and microphysical parameters are shown in Figure 11, which provides normalized frequency distributions of 1 Hz observations of temperature, w, Mean D_{2DS} and M_{2DS} for varying SHS. Results are shown for liquid phase (A–D), mixed phase (E–H), ice phase (I–L), and all phases combined (cloud; M–P). The liquid, mixed, ice and cloud results use SHS_{liq}, SHS_{mix}, SHS_{ice} and SHS_{cld}, respectively. In order to provide an analysis of cloud transects having comparable spatial scales, as well as allowing for the analysis of localized regions of heterogeneity within relatively long transects, transects containing more than 20 samples are split into intervals of 20 samples, which are defined as sub-transects. Additionally, a minimum of 5 samples is required for a transect to be included in the analysis (e.g., a

cloud transect having 68 samples is broken up into three sub-transects, each having 20

samples and one sub-transect having 8 samples). Results were not statistically different

when splitting transects into intervals of 10, 30, 40 and 50 samples (Figure E1,2,3,4 in

supplementary material).
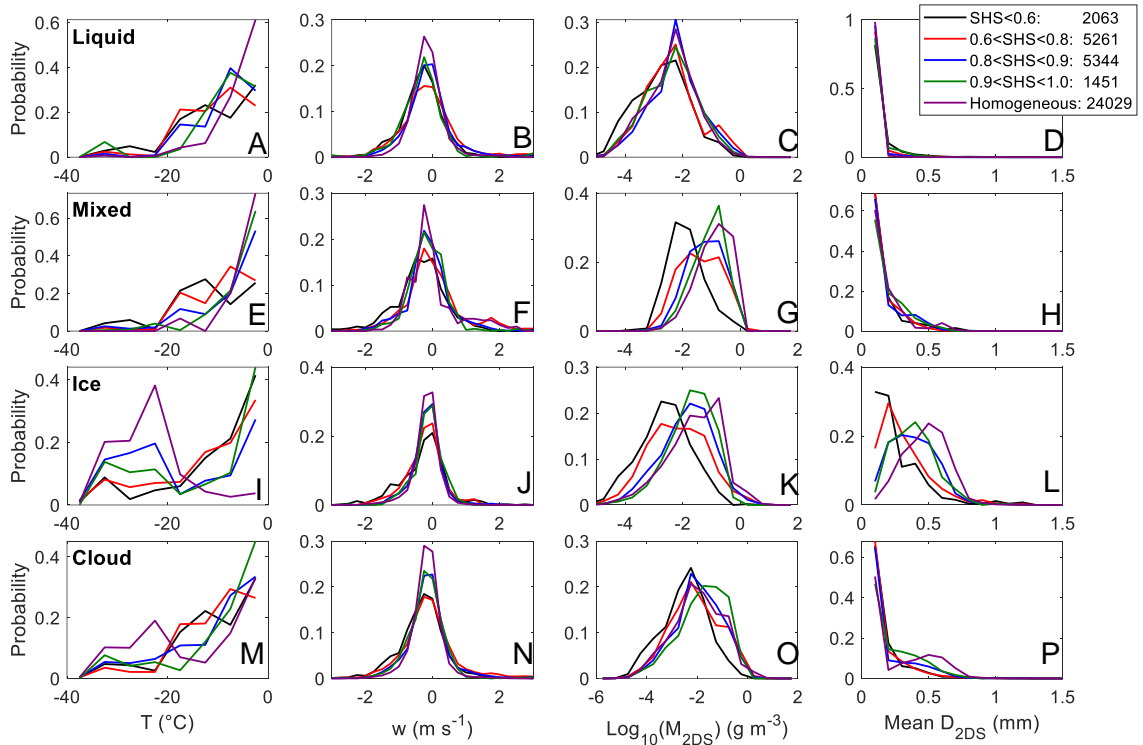
Figure 11: Normalized frequency distributions of temperature (leftmost column), w (left column), M_{2DS} (right column) and Mean D_{2DS} (rightmost column) for varying ranges of SHS. Results are shown for liquid (A–D), mixed (E–H), ice (I–L) and all phases combined (cloud; M–P). Analyses of liquid, mixed, ice and cloud samples are applied using SHS_{liq}, SHS_{mix}, SHS_{ice} and SHS_{cld}, respectively. Cloud transects longer than 20 samples are broken down into intervals of 20 samples. Transects shorter than 20 samples must contain at least 5 samples. The number of samples for each range of SHS_{cld} are included in the legend. Homogeneous represents transects containing only one phase.

Distributions of temperature for each phase are visually relatively similar among

the different heterogeneity ranges, namely, the frequencies at different ranges of SHS

generally decrease with decreasing temperature. However, there are differences worth

noting. Larger frequencies of greater SHS_{liq} and SHS_{mix} occur at temperatures greater

than -5°C, suggesting more spatial heterogeneity for these phases is observed at relatively lower temperatures (Figure 11A,E) which is consistent with Figure 8C,D. In addition, more homogeneous distributions of ice are observed at temperatures less than -20°C. This is seen with probabilities of ice greater for $SHS_{ice}>0.8$ and completely homogeneous sub-transects exceeding those of lower SHS at temperatures less than -20°C (Figure 11I). Finally, sub-transects are generally found to increase in heterogeneity (decreasing SHS_{cld}) with decreasing temperature from -20°–0°C (Figure 11M). Other notable trends are observed for additional parameters. For example, distributions of w are slightly broader for spatially heterogeneous sub-transects compared with more homogeneous sub-transects (Figure 11B,F,J,N), which exhibit slightly higher peaks. Statistical tests confirmed that this difference is significant (using two-sample Kolmogorov-Smirnov tests at a significance level of 1%) by performing multiple comparisons for different SHS ranges. This trend is most notable when examining the heterogeneity over entire sub-transects (Figure 11N), as seen by peak frequencies of ~0.29, ~0.23 and ~0.18 at w~0 m s^{-1} for completely homogeneous, $0.8<SHS_{cld}<1.0$ and $SHS_{cld} < 0.8$, respectively. The broader distributions of w suggest stronger turbulence may be related to the increase in heterogeneity within cloud transects.

In contrast, only ice particles appear to correlate with spatial heterogeneity, as highlighted by results of mean D_{2DS} and M_{2DS}. M_{2DS} decreases with decreasing SHS_{mix} and SHS_{ice} (Figure 11G,K), whereas distributions are similar for varying SHS_{liq} (Figure 11C). Likewise, mean D_{2DS} decreases with decreasing SHS_{ice} (Figure 11L). However, distributions of mean D_{2DS} are nearly identical for the liquid and mixed phase, although this is due presumably to the large number of 2DS samples containing both liquid

33

droplets and ice particles, of which liquid droplets dominate the number concentrations and number-weighted mean. In addition, N_{CDP}, σ_{D_CDP}, and M_{CDP} were similarly analyzed (as well as N_{2DS}, horizontal windspeed, and wind direction relative to flight direction; Figure F and Figure G in supplementary material, respectively) and were found to be similarly distributed regardless of SHS.

The distributions of the microphysical properties do not show any relation with SHS_{cld}, i.e., when observations from all phases are combined (Figure 11O,P). This is most likely due to the similarly distributed liquid phase data at varying ranges of SHS_{liq} (Figure 11C,D) smoothing out the combined liquid, mixed and ice phase distributions used with SHS_{cld}. Thus, differences are only observed in the microphysical properties of ice particles when related to the spatial heterogeneity of their respective phases and not that of the overall cloud sub-transects.

2.4. Discussion

In-cloud samples are determined to be either liquid, ice or mixed phase using a combination of cloud probes (CDP, RICE and 2DS). Potential caveats of the proposed phase classification method include the inability to discern whether a sample of particles having D<50 μm includes both ice and liquid particles. Further, a degree of subjectivity is inherent when visually classifying particles having D>50 μm. Aspherical particles can appear spherical in 2DS imagery, and spherical particles may even be frozen drops. However, it was shown in Section 2.2 that CDP and RICE can be used as a proxy to infer whether the phase of the larger particles was correctly classified. Additionally, ice is often expected to be associated with larger particle sizes, as theory dictates that under most conditions near water saturation, ice particles will quickly grow larger than droplets,

such as in the types of cloud regimes sampled during SOCRATES. It is also important to note that the aircraft would have experienced significant icing and aborted in-cloud measurements if flown through regions of large SLW containing large droplet sizes at temperatures below which kinetic heating fails to offset below-freezing ambient temperatures, although SLW contents are often low in clouds sampled during SOCRATES. However, the most noticeable uncertainty of the phase ID is discerning supercooled drizzle (associated with minimal aircraft icing) and precipitating ice. While caution was taken to visually examine samples of precipitation, this may introduce slight biases in the frequency of liquid and ice phase samples primarily from -10° to 0°C (samples below cloud base) in Figure 5. Overall, the observational strategy discussed in Section 2.2 provides a relatively uniform in-cloud sampling distribution to minimize any sampling bias associated with the structure of boundary layer clouds.

In situ measurements cannot be used to examine the evolution of mixed phase conditions in a Lagrangian framework, due to the aircraft's inability to sample an air parcel throughout its trajectory, which was not a major objective of the SOCRATES flights used in this study. However, theoretical and modeling studies show the evolution of mixed phase volumes almost always transitions from mostly liquid to all ice (e.g., when the WBF process and/or riming dominates). Therefore, by examining mixed phase samples as a function of LWC/TWC, different microphysical properties can be ascertained, where values near 1 depict conditions before the start of the glaciation process and values approaching 0 correspond to complete glaciation.

Figure 6 reveals U-shaped distributions in the frequency distribution of LWC/TWC for mixed phase samples, showing relatively uniform distributions from -20°

to 0°C and distributions resembling inverse exponential functions from -40° to -20°C. Samples from all temperatures are combined in Figure 7A, revealing an exponential shape consistent with the study of McFarquhar et al. (2007a). They also sampled stratocumulus boundary layer clouds, but over the Arctic, finding a relatively uniform distribution of LWC/TWC near cloud base with an increasing frequency of LWC/TWC>0.9 towards cloud top in single-layer stratocumulus mixed phase clouds. The uniform distribution of LWC/TWC near cloud base is consistent with results in Figure 6, which show the most uniform distributions of LWC/TWC at -10° to 0°C, which generally includes most samples near the base of the lowest cloud layers.

Liquid number concentrations decrease as LWC/TWC decreases, whereas the number weighted mean D and σ_D of liquid drops increase as LWC/TWC decreases. This may be due to smaller droplets preferentially evaporating at the expense of the larger droplets. Secondary ice production mechanisms (e.g., Field et al., 2017) may also play a role in these trends. Flight scientists on the G-V during SOCRATES often found drizzle collocated with ice particles, potentially suggesting that precipitation can be induced while the WBF process is acting (discussed in flight reports such as RF05, RF12, RF15). Korolev (2007) performed a box model study highlighting that the WBF process only occurs given prerequisite background requirements and discusses the range of vertical velocities whereby WBF can occur. The study found that both ice crystals and liquid drops could grow given sufficient updraft speeds. Another potential mechanism may be the removal of smaller liquid droplets via accretion. This is consistent with the increase in N_{2DS} as LWC/TWC decreases from 1.0 to 0.4, which could be related to secondary ice production such as rime splintering activating via accretion (i.e., the Hallett-Mossop

process).

Results examining the spatial heterogeneity of liquid, mixed and ice phase occurrence within clouds suggest the mixed phase appears to be the most spatially heterogeneous. Further, SHS_{cld} are often between 0.6 and 1.0, suggesting relatively homogeneous regions often occur within transects along with "pockets" of increased heterogeneity, such as that observed in Figure 3 around 02:28:50 UTC. In fact, results in Figure 11 are split up into sub-transects in order to focus on localized regions of heterogeneity within larger transects. Such localized regions of heterogeneity, associated with "pockets" of ice and mixed phase within large swaths of supercooled liquid, could be nucleating via heterogenous nucleation. Recent work has highlighted the relatively sparse but present ice nucleating particles observed over this region (e.g., Finlon et al., 2020; McCluskey et al., 2018).

The existence of small-scale generating cells at cloud top may also be impacting the heterogeneity as Wang et al. (2020) showed that the horizontal scales of generating cells from which the precipitation emanates range from approximately 200 to 800 m, smaller than those observed over the mid-latitudes (Rosenow et al., 2014) or the Arctic (McFarquhar et al., 2011). Further, the lengths of cloud segments may be directly related to generating cells, as segment lengths are often within the range of generating cells as described in Wang et al. (2020) for lower SHS. However, they found number concentrations of particles having D>200 μm (of which ice particles dominate) were greater within generating cells compared with outside of them. Work presented here shows the mass and number-weighted mean D of ice particles generally decreases as cloud segments decrease in horizontal length (i.e., increase in spatial heterogeneity).

Additionally, a similar analysis was performed on N_{2DS} having D>200 μm as in Figure 11 (Figure H in supplementary material) and values slightly decreased with increasing spatial heterogeneity. However, Wang et al. (2020) only selected 16 selected flight legs for analysis, when the GV aircraft was sampling near cloud top. Future work will focus on relating spatial heterogeneity to physical features within the environment.

A physical reason describing the decrease in M_{2DS} and $Mean_{2DS}$ with increasing heterogeneity may be related to cloud lifetimes. If SHS is considered as a proxy for the evolution/lifecycle of a cloud region, whereby "pockets" of supercooled liquid nucleate and freezing events spread spatially, then lower SHS_{liq} and higher SHS_{ice} would be expected with an "aged" cloud region. This would be consistent with the increase of ice mass and mean D (and relatively constant liquid mass and number concentrations) observed with increasing homogeneity.

In situ data are the measurements best suited for determining the heterogeneity of phases in Southern Ocean clouds, and this has important implications for modeling studies. Zhang et al. (2019) showed that parameterizing mixed phase clouds as pockets within supercooled cloud fields for arctic clouds improved model agreement with observed liquid water contents from in situ observations taken during the Mixed Phase Arctic Cloud Experiment (Verlinde et al., 2007). Tan & Storelvmo (2016) performed a quasi-Monte Carlo sampling of varying parameters in the Community Atmospheric Model version 5.1 (CAM5) and found the vapor depletion rates associated with the WBF process contributed to the greatest amount of variance of the mass partitioning of mixed phase clouds. They further tested CAM5 for the spatial heterogeneity of phase by parameterizing mixed phase clouds as having "pockets" of liquid and ice versus the

assumption of ice and liquid as homogeneously mixed, and found the simulations improved cloud macro-scale features when compared to satellite observations. They noted that the assumption of mixed phase clouds as homogenously mixed ice and liquid particles in the model results in irregularly large rates of vapor depletion, rapidly evaporating liquid at the expense of ice growth. The results presented here confirm that mixed phase regions are often on the scale of 100 m to 10 km, and adjusting models to parameterize the spatial distribution of phase as such will increase cloud fraction and lifetimes, which in turn may improve representations of radiative profiles over the SO.

2.5. Conclusions

The purpose of this study is to present the characteristics of cloud phase over the Southern Ocean using airborne in situ observations acquired during SOCRATES, which primarily sampled low-level clouds over the Southern Ocean. The relative phase frequencies controlled by temperature reveal an exceptionally large frequency of supercooled liquid between -20° and 0°C. Ice was observed at temperatures near freezing and supercooled liquid at temperatures near -35°C. A sharp decrease in supercooled liquid was observed once temperatures dropped below -20°C, suggesting that the activation of ice nucleating particles might be the primary influence on the presence of different cloud phases. This is consistent with similar findings of a sharp increase in ice phase occurrence frequencies observed over Cape Grim, Tasmania (Alexander & Protat, 2018).

The spatial heterogeneity of cloud phase is examined by relating the number and lengths of different cloud phases contained within each cloud. A metric is also introduced which diagnoses a degree of spatial heterogeneity to each cloud sampled. Results show

that most clouds are relatively spatially homogeneous as highlighted in Figures 8C,D and 8. The spatial heterogeneity of specific phases are also examined, and results show that the mixed phase is the most spatially heterogeneous from -20° to 0°C, whereas the liquid phase is the least spatially heterogeneous from -10° to 0°C and the ice phase from -20° to -10°C. Correctly characterizing the spatial heterogeneity of low-level clouds over the Southern Ocean is crucial, as assumptions on phase mixing can have major impacts on cloud cover, lifetime, and microphysical properties.

Finally, local microphysical and meteorological properties are related to the spatial heterogeneity of both the individual phases and of the cloud transects. Transects generally increase in heterogeneity with decreasing temperature from -20° to 0°C, and the distribution of w broadens with decreasing SHS_{cld}. In addition, the mass and mean diameter of ice particles are found to decrease with increasing heterogeneity. Future work will further explore the relation of microphysical properties to spatial heterogeneity.

3 An evaluation of the phase and microphysical properties of single- and multi-layer clouds over the Southern Ocean using in situ observations from SOCRATES

3.1. Introduction

Clouds over the Southern Ocean have been notoriously difficult to simulate in both climate models (e.g., D'Alessandro et al., 2019; Kay et al., 2012; Matus & L'Ecuyer, 2017; McCoy et al., 2014) and high resolution models (Huang et al., 2015; Huang et al., 2014; Naud et al., 2014). Climate models have overestimated shortwave absorption over this region (Trenberth & Fasullo, 2010), which has been attributed to the underestimation of liquid water content and cloud fraction (e.g., Bodas-Salcedo et al., 2016). This may be due in part to extremely low ice nucleating particle (INP) concentrations (N_{INP}) present over the Southern Ocean as observed on ships (McCluskey et al., 2018). While recent model changes have improved simulated clouds by increasing the frequency of supercooled liquid, work is still required to further improve the representation of microphysical properties (e.g., Gettelman et al., 2020; Yang et al., 2021) and the understanding of processes producing supercooled water.

Single- and multi-layer clouds are commonly observed over the Southern Ocean, with prior observations indicating multi-layer clouds accounted for 34% of cases when clouds were present (Haynes et al., 2011). Multi-layer clouds refer to the presence of multiple cloud layers separated by a cloud free interstice, containing either precipitation or clear-sky (e.g., Intrieri et al., 2002; Liu et al., 2012). This is distinct from vertically heterogeneous clouds, in which cloud properties embedded within a single-cloud layer vary (e.g., Verlinde et al., 2013). Although climate models often fail to capture multi-

layer clouds due to their coarse vertical resolution (e.g., Atlas et al., 2020), multi-layer clouds occur frequently and substantially impact the radiative budget. Because of this, climate models often parameterize vertical cloud overlap to adequately treat radiative fluxes throughout vertical columns (e.g., Collins, 2001).

Although the reasons that multi-layer clouds form is still uncertain, multiple explanations have been proposed. For example, Tsay & Jayaweera (1984) found that a combination of large-scale processes can account for multi-layered stratus. Herman & Goody (1976) showed that shortwave absorption of droplets within a cloud layer leads to evaporation within the cloud deck, which along with destabilization due to longwave cooling at cloud top can lead to the formation of two layers. Multiple cloud layers can also result from inhomogeneous temperature/moisture horizontal advection (Luo et al., 2008). They are also associated with additional complexities which do not need to be considered for single-layer regimes, such as seeder-feeder mechanisms (Fleishauer et al., 2002; Hobbs & Rangno, 1998; Houze, 2014).

Differences in cloud layering can impact the zonally averaged top-of-atmosphere longwave and shortwave radiative fluxes by the order of 10 W m^{-2} (Li et al., 2011), contributed in part to differences in the cloud layer heights and thicknesses. Further, overlying cloud layers can substantially impact the evolution of the underlying boundary layer clouds. Their presence increases downward longwave radiative flux by an average of 30 W m^{-2}, impacting turbulent mixing, vertical development and precipitation rates of the underlying cloud layers (Christensen et al., 2013).

Cloud layer microphysical properties substantially impact turbulent, precipitation and radiative properties. Thus, high vertical resolution measurements of cloud profiles

are needed for both single- and multi-layer clouds. A few studies showing vertical profiles of cloud microphysical properties over the Southern Ocean using in situ observations have been performed (e.g., Ahn et al., 2017, 2018; Boers et al., 1996, 1998; Chubb et al., 2013, 2016). However, they were primarily case studies lacking statistically significant datasets, and they primarily focused on single-layer clouds. Little effort has been put towards contrasting the microphysical properties of single-versus multi-layer clouds, and the dearth of prior in situ observations over the Southern Ocean relative to the Arctic warrants a statistical analysis of the varying properties of single- and multi-layer clouds.

This study aims to produce a statistical overview of single- and multi-layer clouds over the Southern Ocean using in situ observations. Section 3.2 and 3.3 describe the instrumentation and the methodology used to obtain vertical profiles as well as classify the measured profiles as either single- or multi-layer clouds. Sections 3.4–3.7 presents the cloud microphysical properties and phase occurrence frequencies for single- and multi-layer clouds, as well as comparisons of cloud condensation nuclei (CCN) and INP in relation to cloud properties. Section 3.8 delivers concluding remarks.

3.2. Instrumentation and cloud presence/phase methodology

This study uses observations acquired with instruments onboard the National Science Foundation/National Center for Atmospheric Research Gulfstream-V (GV) aircraft during the Southern Ocean Cloud-Radiation Aerosol Transport Experimental Study (SOCRATES). The aircraft primarily targeted cold sector boundary layer clouds. Flight plans were designed to ideally sample 10-minute level legs above cloud, in cloud, and below cloud, followed by sawtooth legs (i.e., sawtooths) to obtain vertical profiles.

Since major components of this chapter involve evaluating both the variation in cloud properties of single- and multi-layer clouds as well as the vertical structure of the different cloud layer types, the vertical profiles will be used to diagnose the cloud layers.

Bulk properties of cloud particles measured by the CDP and 2DS correspond with the properties of cloud particles with D less than and greater than 50 μm, respectively. Samples are determined to be either in-cloud or clear-sky following D'Alessandro et al. (2021), which utilizes measurements from the CDP and 2DS. Samples are considered in-cloud if the derived mass content of CDP observations (M_{CDP}) is greater than 10^{-3} g m^{-3} or if any particles are detected with D_{2DS}>50 μm. These threshold values were selected to eliminate sea spray and other large aerosols. The small threshold of M_{CDP} ensures that even optically thin clouds are included in the sample. The phase of in-cloud samples is also determined following D'Alessandro et al. (2021), which determines the phase of small cloud particles (D<50 μm) using a set of threshold values for the CDP and Rosemount Icing Detector measurements, whereas the phase of large particles (D>50 μm) uses a combination of multinomial logistic regression and visual examination of particle imagery from the 2DS. The phase of large particles may be classified as either liquid, ice or mixed (i.e., a sample volume containing both liquid and ice particles) whereas the phase of small particles may only be classified as either liquid or ice. Additional details of the phase classification are discussed in Section 2.2.

Additional instrumentation to obtain measurements utilized in this study are described below. Filters were collected using a forward-facing inlet (Stith et al., 2009) on the GV for offline immersion freezing measurements of INP concentrations from the released particle suspensions using the Colorado State University ice spectrometer

(DeMott et al., 2017). The sample collection approach similarly follows that of previous aircraft studies (Levin et al., 2019; Twohy et al., 2016), of which further details on the methodology can be found. Measurements of CCN were obtained using two miniaturized stream-wise thermal gradient CCN counters (Roberts & Nenes, 2005; Sanchez et al., 2021). One gathered 1Hz data at a constant supersaturation of 0.43%, whereas the other operated with a scanning flow and temperature to measure CCN spectra from 0.06% to 0.87% supersaturation every five minutes. This study uses measurements from the latter, but only using CCN data with supersaturations from 0.26% to 0.34%. This range of range of supersaturation is chosen since CCN concentrations at this range best correspond with observed N_{CDP} concentrations (Sanchez et al., 2021). Shortwave irradiance measurements were taken with a Kipp and Zonen CMP22 Pyranometer. Infrared irradiance measurements were taken using two Kipp and Zonen CGR4 Pyrgeometers. Temperature was measured using a fast-response Rosemount temperature probe. For steady conditions the estimated accuracy and precision are 0.3K and 0.01K, respectively. Water vapor was measured using the 25-Hz Vertical Cavity Surface Emitting Laser (VCSEL) hygrometer (Zondlo et al., 2010). Additional laboratory calibrations of the VCSEL water vapor measurements were conducted in summer 2018, and the final data were reprocessed (Diao, 2021). Relative humidity (RH) is calculated following Murphy & Koop (2005). The combined uncertainties from temperature and water vapor measurements results in the uncertainty of RH ranging from 6.3%–6.7% from 17° to -31°C, respectively, which is the temperature range of the cloud layers in this study (discussed in more detail in the following section). Remote sensing platforms onboard the aircraft include the High-

performance Instrumented Platform for Environmental Research (HIAPER) Cloud Radar (Vivekanandan et al., 2015) and High Spectral Resolution Lidar (HSRL; Eloranta, 2006).

3.3. Cloud layer classification

Clouds measured during all sawtooths performed during SOCRATES are classified as either single- or multi-layer clouds. Level legs are not included in the analysis because they do not provide information about the vertical profile. In the analysis, transects are first defined as ascending or descending legs, and included in the analysis provided the rate of altitude change was consistently greater than 3 m s^{-1} for the transect, which is less than the typical ascent or descent rate of the G-V during sawtooths which was 5 to 7.5 m s^{-1}. Transects with vertical lengths less than 60 m are removed from this analysis, all of which only contained one single-cloud layer.

An automated cloud layer classification method is introduced to provide an objective measure for identifying individual layers within each transect. For data obtained during each transect, a smoothing filter is applied to all 1-s in-cloud samples defined as having $M_{CDP} > 10^{-3}$ g m^{-3}. A binary array is first created where samples with $M_{CDP} > 10^{-3}$ g m^{-3} are set equal to one and all other samples equal to 0. A Savitzky-Golay smoothing method (Savitzky & Golay, 1964) is applied with a moving window of 30 1 Hz samples to each binary array. The Savitzky-Golay filter is used since it better preserves peak heights and widths of data features compared with lower order moving averages. Individual layers are identified where consecutive samples of the smoothed binary arrays exceed 0.5. Clear interstices between layers of at least 3 m can potentially be captured using this method, with the exact threshold dependent on the aircraft rate of ascent or descent rate. The vertical extent of the cloud layer within an area where the smoothed

binary array exceeds 0.5 is determined to be between the highest and lowest in-cloud sample having $M_{CDP} > 10^{-2}$ g m^{-3}. The lower M_{CDP} threshold applied prior to smoothing ensures cloud top and base is contained in each area of the smoothed binary area exceeding 0.5. All layers identified using this method are shown by the shaded rectangles in Figure 12. The CDP is solely used to identify cloud layers without the use of the 2DS to ensure that the presence of precipitating ice or drizzle is not used to identify a cloud layer when small droplets or ice crystals are not present. A cloud layer is only included in the analysis if the entirety of the layer (cloud base to cloud top) is contained within the transect.

Although flight plans were designed with the intent of sampling all cloud layers during sawtooths, it is possible that some layers may have been missed if the G-V did not ascend or descend to the altitude where these layers were located. Furthermore, for transects where there was a very narrow interstice between layers, the irregular clustering of CDP measurements make it difficult to determine the number of layers. Thus, the forward-facing camera was inspected for each transect to evaluate the classification. This was additionally required for cases when the GV intersected the same cloud layer twice (e.g., protruding filaments of cloud below cloud base). Reflectivity profiles from the HIAPER cloud radar and retrievals from the HSRL acquired during the transects were similarly used to distinguish cloud layers and also to check for cloud layers directly above and below the aircraft. The classification algorithm performed relatively well, as only 16% of the layers were corrected after manual inspection.

Figure 12 shows M_{CDP} from vertical transects flown by the GV aircraft, with layers indicated by the coloring within each rectangular box. Each column represents a single-

vertical transect, arranged in the order they took place as shown by the research flight number (RF01–RF15) underlying the respective columns.
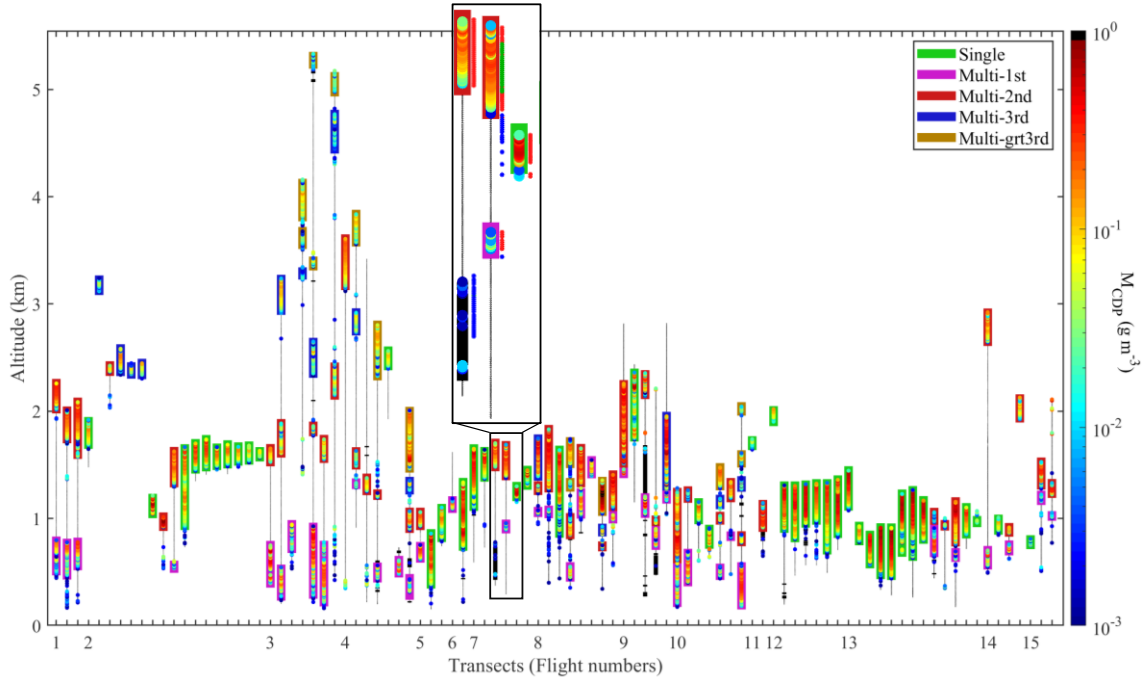
Figure 12: Vertical profiles of M_{CDP} from select ramped ascents and descents flown during SOCRATES that meet criteria described in Section 3.3. Profiles are only shown for transects where the highest and lowest altitude samples of each transect are considered clear-sky. Colored circles show M_{CDP} where $M_{CDP} > 0.001$ g m^{-3}. Solid black lines show the vertical extent of each transect. Black shaded regions represent samples where $M_{2DS} > 0.01$ g m^{-3} and $M_{CDP} < 0.001$ g m^{-3}. Red, green and blue markers to the right of the transects in the magnified panel indicate liquid, mixed and ice phase samples, respectively. Phase markers are only shown for temperatures less than 0°C.

The color of the rectangular box surrounding the M_{CDP} shading represents the identification of that profile as either a single-layer, or the lowest (Multi-1st), second lowest (Multi-2nd), third lowest (Multi-3rd) or higher layer (Multi-grt3rd) in a multi-layer cloud as determined from the cloud layer classification. Both single- and multi-layer clouds were regularly encountered in approximately half the flights, whereas other flights predominantly sampled either multi-layer or single-layer clouds (e.g., RF01 only has two-layer clouds, RF12&13 primarily have single-layer clouds). The magnified panel

shows profiles representative of most the layers sampled and includes phase information as colored markers immediately to the right of the transects. Cloud layers were typically composed of supercooled liquid and mixed phase samples. A case of light ice precipitation ($M_{2DS} < 0.01$ g m^{-3}) is observed for the highest cloud layer in the middle transect. Cloud layers were often found to precipitate either supercooled drizzle or ice, which has been previously documented (e.g., Alexander et al., 2021). Overall, 55 single-layer clouds and 183 multi-layer clouds were identified from 153 transects using this procedure. Although cloud layers are included in the analysis regardless of their altitude, the vast majority of sampling took place below 3 km (96% of single-layer clouds and 98% of multi-layer clouds).

Since M_{CDP} is solely used to determine in-cloud conditions, the cloud layer classification method fails to capture ice cloud layers with M_{CDP} below the in-cloud threshold. One such layer is in the magnified panel of Figure 12 as seen by the presence of $M_{2DS} > 0.01$ g m^{-3} (black shading and blue markers). Note that the phase information is only visible for approximately half the length of the layer since temperatures exceed 0°C below the markers and phase information is only provided for temperatures less than 0°C. There were six such layers in total (2% of the observed layers), which are not included in the analysis to be consistent with the in-cloud definition ($M_{CDP} > 10^{-3}$ g m^{-3}) proposed in order to exclude precipitating particles. Additionally, the cloud layer classification method may fail to accurately capture cloud layers which contain these ice layers embedded within multiple liquid or mixed phase layers. However, there were only 3 such layers (1% of the layers) embedded with multiple liquid layers as well as ice layers which

were deep enough to prevent the smoothing algorithm from adequately classify the cloud layers. These layers were not included in the analysis.

3.4. Cloud layer overview

Figure 13 shows the number of profiles with different layer depths for the single- and multi-layered cases (Fig. 13A), as well as the normalized occurrence frequency of different phases that occur in single-layer and multi-layer clouds (Fig. 13B).
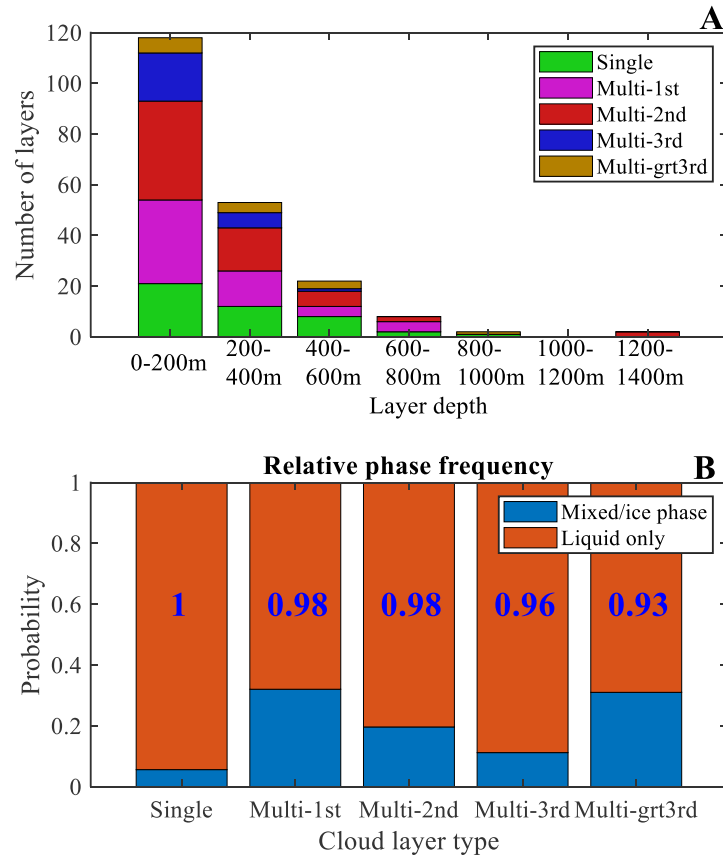
Figure 13: A) A bar chart showing the number of cloud layers with given depth, sorted according to different cloud layer types. B) Relative cloud phase frequency shown for different cloud layer types. Results in B) are only shown at temperatures less than 0°C. The blue numbers are relative frequencies of the mixed phase to all ice-containing samples (mixed and ice phase). Results are only shown for ramped ascents and descents.

Figure 13A shows that relatively thin cloud layers with depths < 200 m are more frequent than deeper layers for both single-layer and multi-layer clouds, and for all different layers

50

of the multi-layer clouds, with these thin cloud layers representing 59% of the layers

sampled during SOCRATES. Cloud layers with average temperatures less than 0°C make

up 76% of all the layers sampled, with 63% of all such layers having depths < 200 m.

Additionally, 77% of the multi-layer clouds are observed within the boundary layer and

the rest above the boundary layer, whereas over 90% of single-layer clouds were

observed within the boundary layer. The boundary layer heights were determined from

visual examination of dropsonde data. For flights without dropsonde data (RF01,08,09),

boundary layer heights are estimated from in situ temperature measurements taken from

sawtooths. Boundary layer heights are then interpolated using a nearest neighbor method

over each respective flight. Some layers could therefore be incorrectly characterized as

either above or within the boundary layer based on uncertainties or limitations associated

with the interpolation method.

Figure 13B shows that single-layer clouds contain the smallest percentage of ice-

containing samples (6%), where ice-containing samples are either ice-phase or mixed-

phase clouds, whereas the lowest layers of multi-layer clouds have the highest observed

frequency of ice-containing phases (32%). The frequency incrementally decreases with

increasing multi-layer cloud height up to the third lowest cloud layer. The highest layers

of multi-layer clouds have nearly similar frequencies of ice-containing samples (31%) as

the lowest layers. The phase frequencies are separately analyzed for above and within the

boundary layer (not shown), and the trends discussed above are observed in both cases

(i.e., greatest liquid phase frequencies in single-layer clouds, lowest liquid phase

frequencies in lowest multi-layer clouds and increasing liquid phase frequencies up to the

third highest cloud layers). Frequency values within the boundary layer are all within

10% of those in Figure 13B, whereas values are much more variable above the boundary layer. The fraction of samples that are mixed-phase compared to all ice containing samples is greatest for single-layer clouds, with slightly lower frequencies for multi-layer clouds, with the frequency decreasing with increasing cloud height (blue text within respective columns of Fig. 13B). Within all cloud layers, over 95% of ice-containing samples are mixed-phase showing the dominance of supercooled water regardless of layering. As cloud phase is dependent on many other factors such as temperature, the presence of large drops and the concentrations and compositions of both CCN and INP, the dependence of cloud phase in the different cloud layers on these parameters is investigated in the following section.

3.5. CCN and INP

Determining the concentration of INP over the SO is difficult in part due to their relatively sparse concentrations over the region (e.g., McCluskey et al., 2018; McFarquhar et al., 2021), which means long averaging times are required to get statistically significant samples above background values. The following discussion provides context for the INP observations gathered by the GV aircraft during SOCRATES and used in this analysis. Sampling of INP is taken over continuous durations on the order of minutes, which here are defined as sample areas. The sample areas were often combined in post-campaign processing accounting for flow rates which ranged from a few to 13 liters per minute (depending on altitude). Sample areas above and within the boundary layer were separately combined, with the combined areas spanning up to 15° latitude. This resulted in accumulated sample volumes ranging from 129 to 840 standard liters of air per flight. The total data acquisition time of all samples

amounts to approximately 23 hours, obtaining a total of 32 filter samples. Since the reported activation temperatures vary for different combined sample areas, reported N_{INP} are averaged at 1°C intervals to obtain N_{INP} with a constant activation temperature resolution of 1°C.

The following analysis relates N_{INP} with relative phase frequencies. To obtain adequate cloud phase sample size(s), combined INP sample areas are interpolated using a nearest neighbor method over the respective flights. Cloud phase data within the interpolated regions (including sawtooth and level-leg data) are then related to N_{INP} from the same sample area(s). The interpolation is separately performed for sample areas above the boundary layer and within the boundary. This mostly results in interpolated areas derived from single sample areas above and within the boundary layer spanning the entire research flights, with the exception of research flights 1,3,4,10. Namely, all in-cloud data above (within) the boundary layer is related with a single set of reported N_{INP} above (within) the boundary layer.

Scatter plots relating N_{INP} and liquid phase frequency (i.e., frequency of liquid phase to all phases) are shown in Figure 14. Results are separately shown within the boundary layer (Figure 14A) and above the boundary layer (Figure 14B). The different colored markers denote samples where the liquid phase frequency is taken within a specified temperature range (left-hand side of legend text) and relates it to N_{INP} having activation temperatures within a specified range (right-hand side of legend text). Measurements of INP are reported with activation temperatures ranging from -30° to -10°C, noting N_{INP} is only measurable for activation temperatures < -10°C. Phase data for temperatures less than -20°C are not included because D'Alessandro et al. (2021)

previously showed there is a sharp decrease in supercooled liquid below -20°C, with ~93% of samples between -30° and -20°C being ice phase.
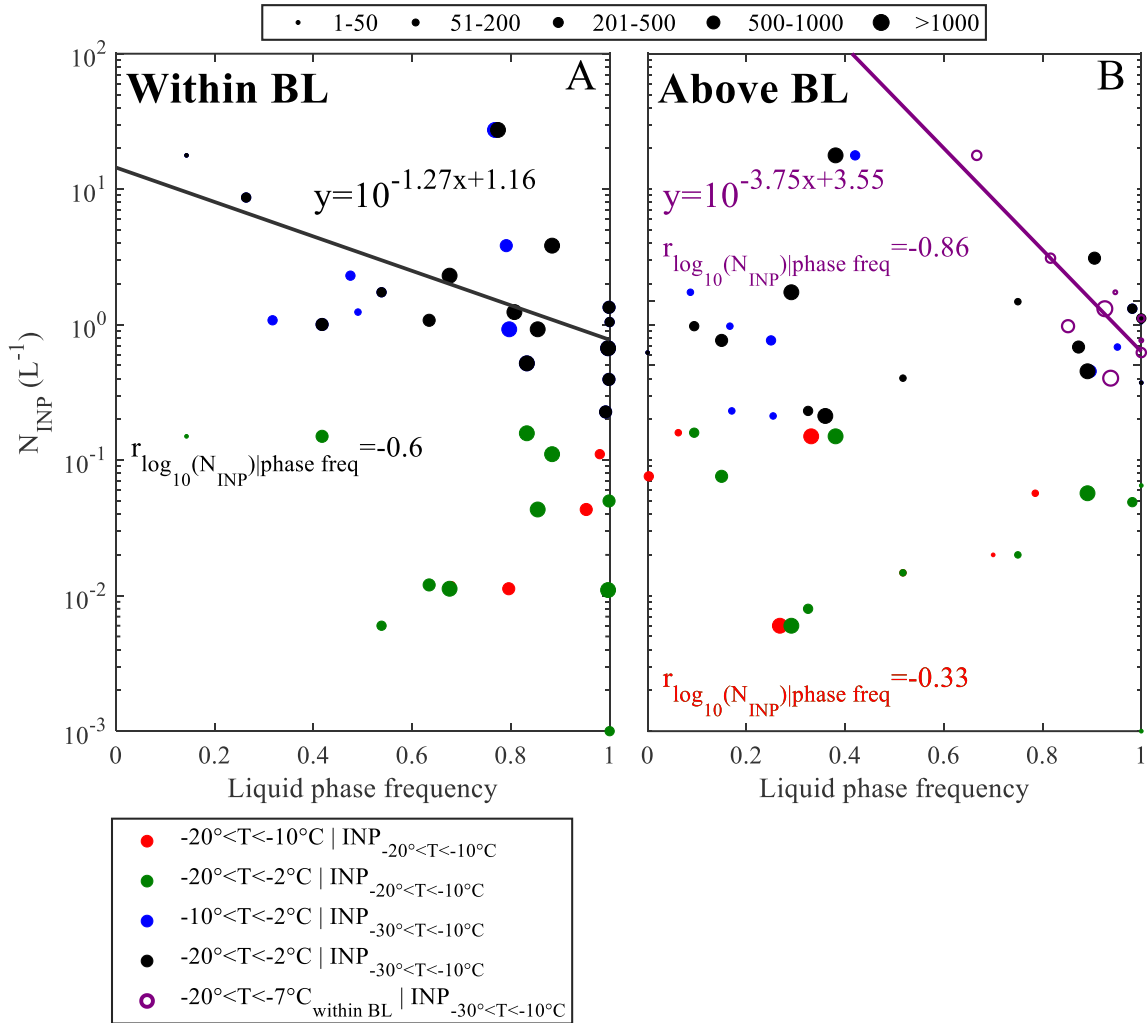
Figure 14: Scatter plots of N_{INP} related to liquid phase frequency (i.e., the frequency of liquid phase samples relative to all in-cloud samples) for samples within the boundary layer (A) and above the boundary layer (B). Samples are taken within the interpolated INP sample areas as described in the text. Different colored markers show liquid phase frequencies taken within specified temperature ranges compared with N_{INP} having different ranges of activation temperatures. The purple circles compare phase frequencies within the boundary to N_{INP} above the boundary layer using the above boundary layer interpolated area. Best fit lines and correlations correspond to the respective phase frequency and INP activation temperature ranges.

Strong negative relationships would likely indicate a prevalence of primary nucleation over the region. Perhaps the most likely temperature range and N_{INP} activation

temperature range expected to show such relationships would be those having similar ranges. However, phase frequencies from -20° to -10°C and N_{INP} with activation temperatures in the same range (red points) are associated with low sample sizes. This is observed by only three data points within the boundary layer, and six above the boundary layer (three of which have sample sizes less than 200; denoted by marker size). This is due in part to the fact that the number of in-cloud samples from -10° to 0°C is more than a factor of two greater than the number of samples from -20° to -10°C (D'Alessandro et al., 2021), and the lowest N_{INP} have relatively warmer activation temperatures which increase semi-exponentially with decreasing temperatures (Järvinen et al., 2022).

There are a few N_{INP} ranges which capture negative relationships associated with primary nucleation. One is for N_{INP} with activation temperatures from -20° to -10°C above the boundary layer. Correlations between N_{INP} and phase frequencies from -20° to -10°C and -20° to -2°C (where N_{INP} is log-scaled) are both approximately -0.3 (only shown for -20° to -10°C; Figure 14B). Another N_{INP} range is that having activation temperatures from -30° to -10°C within the boundary layer, where the correlation between N_{INP} and phase frequencies from -20° to -2°C is more significant at -0.60. This significant correlation is only observed within the boundary layer, which may be unexpected since there are no in-cloud samples below -20°C within the boundary layer. Further, this correlation was observed to decrease when decreasing the range of activation temperatures towards temperatures warmer than -30°C (not shown). Therefore, the correlation may be related to sedimenting INP from above the boundary layer. However, there is no notable relationship between similar N_{INP} and phase frequency temperature ranges above the boundary layer. One possible explanation may be the

prominence of efficient ice nucleation due to pre-activated INP (Mossop, 1956), whereby localized regions above the boundary layer may only experience significant primary nucleation via aged INP. Thus, primary ice nucleation may still occur at colder temperatures above the boundary layer, and contributions from alternative nucleation processes such as accretion and seeding mechanisms may result in decreasing liquid phase frequencies at warmer temperatures underlying the localized areas. There is evidence for this when relating N_{INP} above the boundary layer with phase frequencies below the boundary layer (Figure 14B; purple circles). This is done by obtaining the phase frequencies below the boundary layer using the above boundary layer interpolated sample areas. A correlation of -0.86 is observed between N_{INP} with activation temperatures from -30° to -20°C and phase frequencies from -20° to -7°C with a root mean square error of 0.26. However, phase frequencies including temperatures greater than -7°C results in weak correlations ($|r|<0.2$; not shown).

All the other N_{INP} ranges are weakly correlated ($|r|<0.22$), with the exception of N_{INP} with activation temperatures from -20° to -10°C and phase frequencies within the same temperature range within the boundary layer, although this dataset only contains 3 points. Aside from select combinations of N_{INP} and phase frequencies discussed above, there are no clear relationships between most combinations of the listed phase frequencies and N_{INP}, suggesting a prominence of alternative ice initiation/growth processes (secondary ice nucleation, accretion, etc.). Relationships may be sensitive to whether INP sampling took place above or below clouds, although it is at best extremely difficult to incorporate this distinction due to the interpolated sampling area method

discussed above. At the very least, results here provide a benchmark analysis towards directly relating INP to the frequency of ice over the Southern Ocean.

Liquid phase frequencies are also related to CCN number concentrations (N_{CCN}) to determine the potential impacts of CCN on cloud phase. Due to the greater spatial resolution of CCN measurements compared with INP sample areas, a method is derived to obtain a CCN measurement for each 1 Hz cloud sample. These measurements are determined using a moving window ± n 1 Hz samples from each cloud sample. The average N_{CCN} is calculated within the window over the clear-sky samples, since droplet shattering on the inlet of the CCN counter introduces error in its measurements (Hudson & Frisbie, 1991). The averaging is also restricted to samples above or within the boundary layer, depending on the location of the in-cloud sample. Results applying this methodology are shown in Figure 15, showing the liquid phase frequency for different temperature ranges above the boundary layer (15A–C) and within the boundary layer (15D–F). The different color lines denote the liquid phase frequencies for different percentile ranges of N_{CCN}, where the red line denotes samples within low N_{CCN} environments ($N_{CCN}<33^{rd}$ percentile) and the blue line denotes samples within high N_{CCN} environments ($N_{CCN}>67^{th}$ percentile). Each column shows results using a different window size, shown overlying the respective columns. Results above and within the boundary layer are relatively consistent over the different window sizes. Focusing first on observations within the boundary layer, phase frequencies are either relatively constant or slightly increase with decreasing temperature for all the moving window sizes (15D–F). Although inconsistent with observed increases in the frequency of ice-containing cloud samples with decreasing temperatures (D'Alessandro et al., 2021), results here are

consistent with the increasing liquid phase frequencies with increasing cloud height
(Figure 13B).
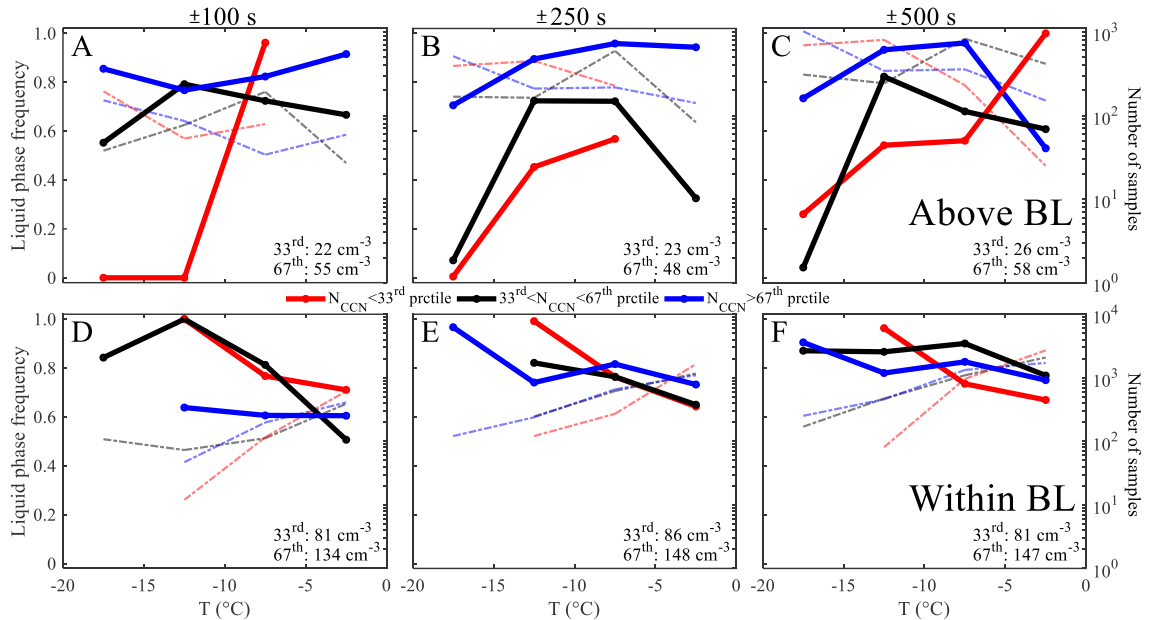
Figure 15: Liquid phase frequencies within 5°C temperature bins above (A–C) and within (D–F) the boundary layer for different N_{CCN} percentile ranges. Results are shown for different moving window averages (overlying each column), in which N_{CCN} are averaged over clear-sky samples (further described in the text). The 33rd and 67th percentiles of average N_{CCN} are included in the respective panels. The number of in-cloud samples are denoted by the dotted-dashed lines.

In contrast, liquid phase frequencies generally decrease with temperature over all the CCN percentiles above the boundary layer (15A–C). Perhaps surprisingly, stark contrasts in the liquid phase frequencies are observed for the different CCN percentiles which were not observed within the boundary layer. Namely, liquid phase frequencies are much greater within high N_{CCN} environments than low N_{CCN} environments. With the exception of two temperature bins (e.g., from -5° to 0°C for the ±500 s window; 15A), the liquid phase frequencies in the high N_{CCN} environments are 0.4–0.85 greater than the low N_{CCN} environments for all moving window sizes. Previous studies have found high N_{CCN} environments correspond with increased frequencies of supercooled liquid in low-level

Arctic clouds, which has been suggested to be due to increasing lifetimes of supercooled liquid clouds (Filioglou et al., 2019). Alternatively, varying N_{CCN} environments may be representative of different air mass source regions, and differences in phase frequencies may be the result of differences in the nucleation tendencies of the associated aerosols. Sanchez et al. (2021) identified four aerosol regimes sampled during SOCRATES, and found environments with high N_{CCN} commonly originated or passed over the Antarctic coast, where elevated phytoplankton biomass (relative to the open ocean) is a major contributor of biogenic emissions.

Additional explanation(s) may be related to varying secondary ice production mechanisms related to the presence of large droplets, which would be limited in a high N_{CCN} environment. For example, large drops have been observed to eject small ice particles as they freeze (i.e., droplet fragmentation) primarily at temperatures less than -10°C (e.g., Korolev & Leisner, 2020). However, a recent study by Järvinen et al. (2022) found little evidence to suggest this is a prominent secondary ice production mechanism over the region. A more prominent mechanism is referred to as the Hallet-Mossep process, which is characterized by splintering of small ice particles off of graupel during riming (Hallett & Mossop, 1974). Previous studies have noted its likely presence over the Southern Ocean (e.g., Huang et al., 2021; Järvinen et al., 2022). The potential for this mechanism to influence phase frequencies is explored here by relating large drop concentrations having dimensions exceeding 25 μm ($N_{CDP\_D>25μm}$) with N_{CCN}, both of which are averaged over the interpolated INP sample areas as discussed earlier. The presence of $N_{CDP\_D>25μm}$ is favorable for the Hallet-Mossop process, which occurs primarily between -8° and -3°C. Averages of N_{CCN} are only performed on clear-sky

samples, whereas large drop concentrations are only averaged over liquid and mixed phase samples. Comparisons are made using the interpolated sample areas since large drop concentrations often varied significantly with average N_{CCN} derived from the moving window method used in Figure 15. Results are provided in Figure 16, which additionally shades the markers by liquid phase frequency. The scatter plot reveals a characteristically parabolic shape, which is motivation to use the Spearman rank correlation. The Spearman correlation is moderately significant at -0.61, suggesting the possibility that high N_{CCN} environments can inhibit the production of large drops due to the increased number of nucleation sites for condensation.
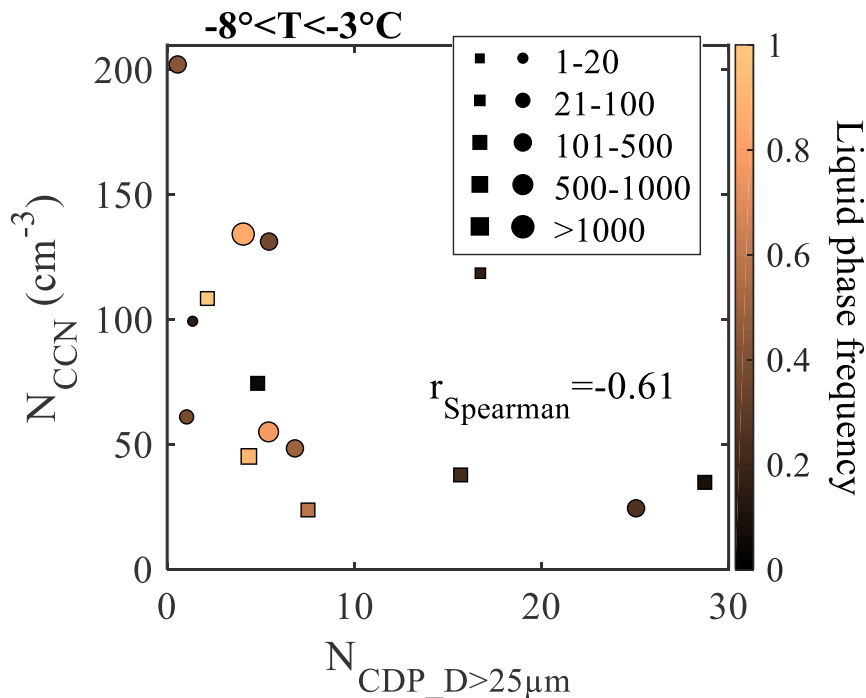
Figure 16: Scatter plots of average N_{CCN} and average N_{CDP_D}>25μm, where averages are taken within the interpolated INP sample areas as in Figure 14. Results are colored by the liquid phase frequency, and marker size denotes the sample size. Circles denote within boundary layer sample areas and squares denote above boundary layer areas.

Liquid phase frequencies are less than 0.2 in all four environments with average $N_{CDP\_D>25μm}$ exceeding 10 cm^{-3}, whereas only two of the eleven environments have

similarly low phase frequencies where there are lower large drop concentrations. This finding combined with the high Spearman correlation suggests a weakened thermodynamic effect whereby secondary ice production is limited by high CCN concentrations (e.g., Rangno & Hobbs, 1991; Jackson et al., 2012). However, the relationship of N_{CCN} and large drop concentrations may also be related to precipitation scavenging, where $N_{CDP\_D>25\mu m}$ is directly related to the presence of drizzle. Sanchez et al. (2021) found low N_{CCN} environments were associated with air masses having a history of precipitation within the previous 1.5 days using back trajectory analysis.

An additional analysis comparing differences in drop concentrations in decoupled and coupled environments is provided in Figure 17.
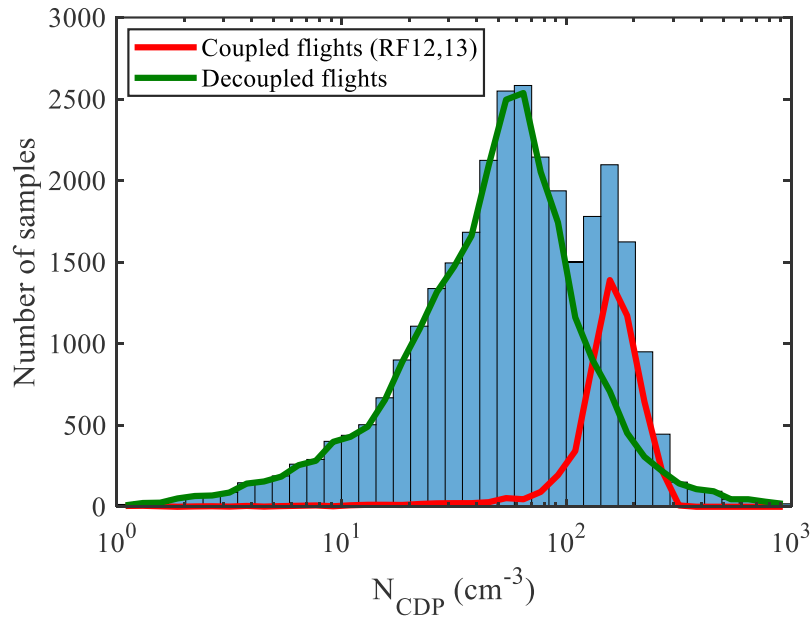
Figure 17: Frequency distribution of N_{CDP} for in-cloud conditions for all flights (blue bars). Green and red lines show distributions of N_{CDP} for decoupled and coupled environments, respectively. Results here include level periods and ramped ascents and descents.

Most of the boundary layers were decoupled with the exception of RF12 and RF13, where the presence of coupling was determined using the dropsonde data following

Wang et al. (2016). Figure 17 shows a distinct bimodality in N_{CDP} due to differences of N_{CDP} in the coupled and decoupled environments. The mode of N_{CDP} for decoupled flights is 70 cm^{-3} and for coupled flights 160 cm^{-3}, consistent with aerosols emitted from the ocean serving as effective CCN in the coupled cases. Perhaps unexpectedly, average N_{CCN} within the boundary layer is highest for RF09 (191 cm^{-3}), second highest for RF12 (175 cm^{-3}) and the third highest for RF13 and RF08 (both are 136 cm^{-3}). Further, average N_{CCN} for RF12&13 above the boundary layer were the fifth and sixth highest of all 15 research flights. The tendency for RF12&13 not having the highest average N_{CCN} is similarly observed when evaluating N_{CCN} at supersaturations greater than and less than 0.3% (not shown) and warrants further investigation.

3.6. Cloud layer properties and profiles of radiative fluxes and drop clustering

Figure 18 shows normalized frequency distributions of N_{CDP}, M_{CDP}, the standard deviation of D from CDP drop size distributions (σ_{CDP}) and the mean volume weighted diameter (MVD_{CDP}) for single-layer clouds and the different layers of multi-layer clouds using data from all flights. In Figure 18A it is seen that the N_{CDP} mode for single-layer clouds is greater than 100 cm^{-3}, coinciding with the N_{CDP} mode for flights taken in coupled environments shown in Figure 17 (RF12 and RF13, both of which primarily sampled single-layer clouds as seen in Figure 12). To examine the effect of coupling on the distribution of N_{CDP}, results for single-layer cases restricted to decoupled environments are separately shown by the dashed line. When comparing the solid and dashed black lines for the properties in all panels, N_{CDP} is the only property shown that significantly diverges for the coupled and decoupled environments. N_{CDP} distributions in

decoupled environments are more similar to distributions of all multi-layer clouds than to single-layer distributions in coupled environments. In contrast, the modes for M_{CDP}, σ_{CDP} and MVD_{CDP} are relatively similar in coupled and decoupled environments (all of which are between 100–300 cm^{-3}, 3–4 μm and ~16, respectively).
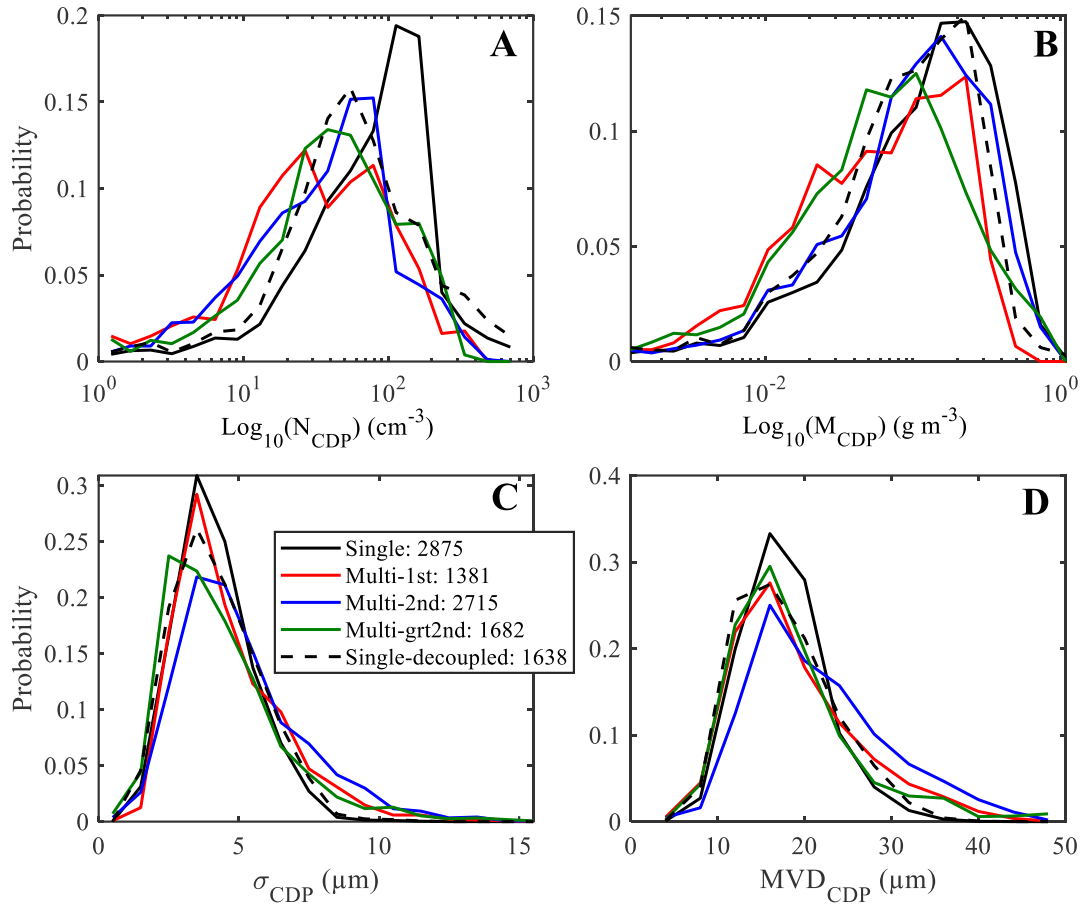
Figure 18: Normalized frequency distributions of N_{CDP} (A), M_{CDP} (B), σ_{CDP} (C) and MVD_{CDP} (D) for different cloud layer types. The black solid and dashed lines show all single-layer samples and single-layer samples from decoupled environments, respectively. Results are only shown for ramped ascents and descents.

When comparing single-to multi-layer cases, single-layer cases are slightly skewed to larger M_{CDP} values, whereas both σ_{CDP} and MVD_{CDP} (Figure 18C&D) are skewed to larger values for multi-layer cases. These results suggest multi-layer clouds observed during SOCRATES had less liquid water content than single-layer cases, but broader

droplet distributions and larger mean particle sizes. These differences may be related to the relative phase distributions of liquid and mixed phase samples, whereby available liquid is partitioned to large ice particles which often exceed sizes detectable by the CDP. This would be consistent with greater mixed and ice phase frequencies in multi-layer clouds than in single-layer clouds (Figure 13B). Differences are also consistent with a seeder-feeder mechanism, whereby underlying clouds are seeded from overlying clouds to broaden drop size distributions. A seeder-feeder mechanism is similarly consistent with the relative phase distributions of multi-layer clouds (Figure 13B).

Parameters in Figure 18 are also separately evaluated within and above the boundary layer for single- and multi-layered clouds in Figure 19. Focusing on single-layer clouds, all of the distributions are multi-modal above the boundary layer with the exception of MVD_{CDP} (e.g., more than three modes for M_{CDP} in Figure 19B), which is likely due in part to the relatively low sample size (15% of single-layer samples) as well as uncertainties associated with the interpolated boundary layer height. However, the bimodal distribution of N_{CDP} does capture differences observed between coupled and decoupled environments. Larger sample sizes for multi-layered clouds above the boundary layer (26% of multi-layer samples) reveal relatively more robust differences in the multi-layered clouds. Distributions of N_{CDP} and M_{CDP} are slightly shifted towards larger values for multi-layered clouds within the boundary layer, consistent with higher N_{CCN} within the boundary layer. The mode for σ_{CDP} is slightly lower above the boundary layer (equal to single-layer clouds above the boundary layer), whereas distributions of MVD_{CDP} are similar for both multi-layer cloud cases.
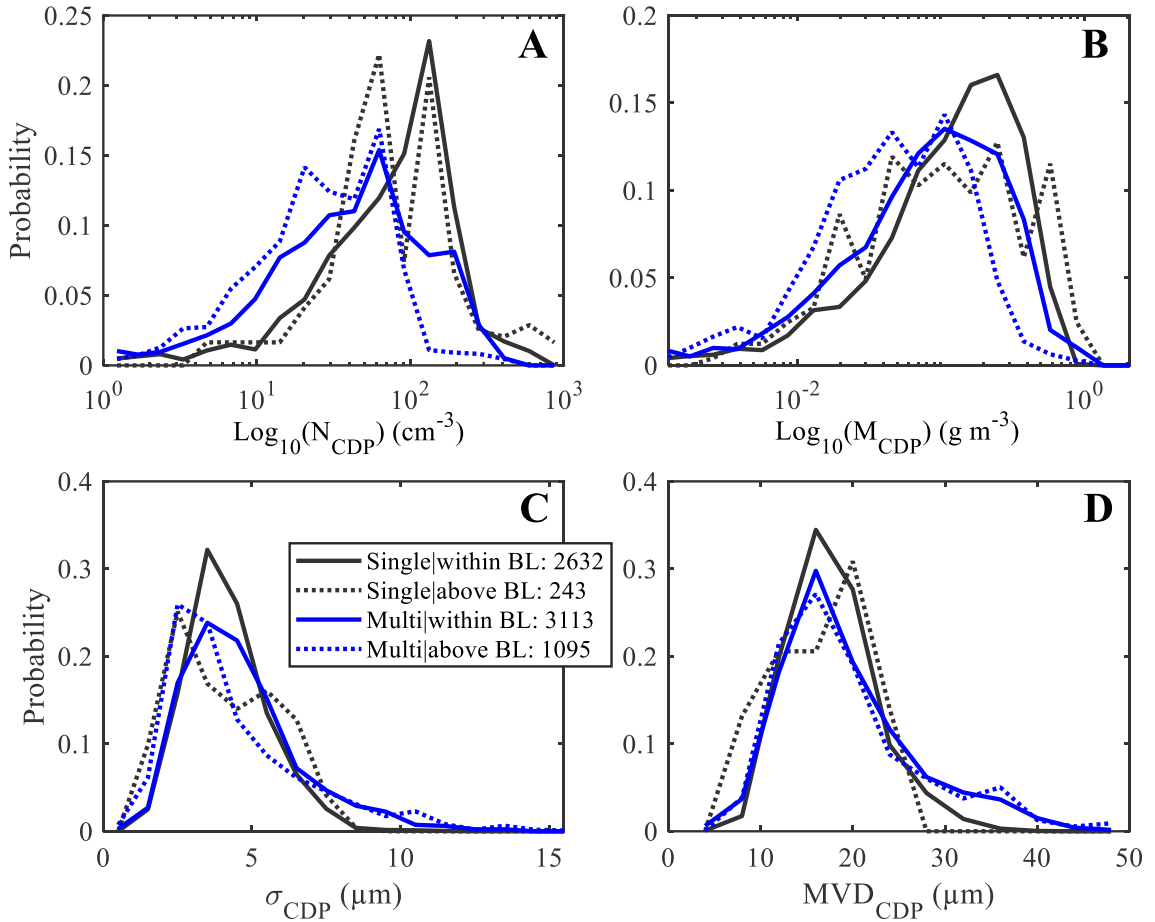
Figure 19: Similar to Figure 18, except single- and multi-layer cloud properties are separately evaluated for samples above the boundary layer and within the boundary layer. The similarity is quantitatively determined using Mann-Whitney U-tests and Kolmogorov-Smirnov tests. These tests are chosen since they do not require prior knowledge of the distributions' shapes. When applying the tests to MVD_{CDP}, both tests do not reject the null hypothesis that both sample sets are taken from the same population at a significance level of 5%. Overall, distributions of σ_{CDP} and MVD_{CDP} are more positively skewed for both multi-layer cases compared with the single-layer cases, confirming differences in the different cloud types is unrelated to differences in boundary layer and free tropospheric conditions.

It is crucial to examine how the properties vary in relation to their location within the cloud layer to get insight into physical processes occurring in the clouds and impacts on vertical profiles of radiative heating. Figure 20 shows joint histograms of both shortwave (solar) and longwave (terrestrial) irradiance as a function of the normalized height within a cloud layer, defined following McFarquhar et al. (2007) as:

$$z_n = \frac{(z - z_{Cloud\_base})}{(z_{Cloud\_top} - z_{Cloud\_base})} \qquad 2)$$

where z refers to the altitude of the local 1Hz sample, z_{Cloud_top} and z_{Cloud_base} refer to the altitudes of cloud top and cloud base for a particular layer, respectively (i.e., the highest and lowest samples within a layer having $M_{CDP} > 0.01$ g m^{-3}, respectively). Cloud layers are split into two categories: those that are the highest layer of their respective regime (top cloud layers; Figure 20A–C) and those that are underlying another cloud layer (non-top cloud layers; Figure 20D–F). Layers in the latter category are only associated with multi-layer clouds and should receive less solar radiation than layers in the former category. This is precisely what is observed when comparing the solar irradiance (F_{solar}) in Figure 20A&D: most measurements in the top cloud-layers occur between 400 and 600 W m^{-2} at $z_n > 0.9$ whereas there are nearly zero (< ~10) cases of solar irradiance greater than 400 W m^{-2} for the non-top cloud layer. Likewise, most measurements of net longwave irradiance (F_{terr_net}) ranges from -110–0 W m^{-2} for the top cloud layer at $z_n > 0.9$, with a mean value of -50 W m^{-2}. In contrast, there are nearly zero cases of F_{terr_net} < -50 W m^{-2} for non-top cloud layers.

The heating profiles shown in Figure 20C&F reveal relatively weak cloud top cooling associated with longwave radiation for both the top and lower layers.
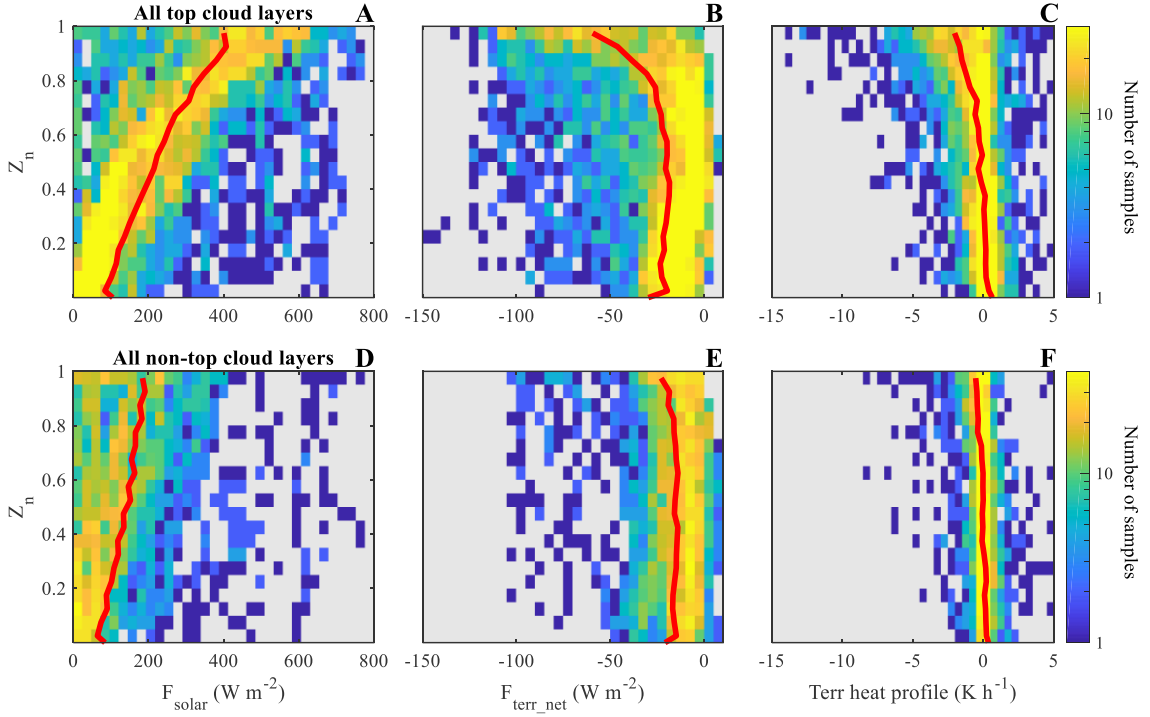
Figure 20: Joint histograms showing the frequency of downwelling solar irradiance (F_{solar}; A,D), net terrestrial irradiance (F_{terr_net}; B,E) and associated heating profiles from terrestrial irradiance (C,F) as a function of z_n for layers including single-layer and the highest layer of multi-layer clouds (top cloud layers; A, B, C) and for underlying cloud layers (non-top cloud layers; D, E, F). Red lines show average irradiance and heating rates.

Average cooling rates are ~0.5 K hr^{-1} for $z_n > 0.9$ for non-top cloud layers, and lower than ~2.5 K hr^{-1} for top cloud layers. Such low cooling rates are associated with emitted longwave radiation from overlying cloud layers for non-top cloud layers, as well as relatively low mass contents of clouds over this region, as seen with M_{CDP} having modes ranging from 0.1–0.2 g m^{-3} for all cloud layer types (Figure 18B). Weaker cooling rates may result in weaker cloud top turbulent mixing for non-top cloud layers, resulting in different lifetimes or evolutions for different cloud layer regimes. Higher cooling rates were associated with greater average liquid mass of the top cloud layers. Specifically, average cloud top cooling rates were 1.5 K hr^{-1} greater for cloud layers with average M_{CDP} above the 50th percentile (0.2 g m^{-3}) than below the 50th percentile (not shown).

67

The clustering of droplets, which can have implications for many factors such as precipitation onset (Shaw et al., 1998) and the evolution of raindrop size distributions (McFarquhar, 2004), is evaluated using joint histograms in Figure 21A,B and Figure 21C,D for all non-top cloud layers and all top cloud layers, respectively. Unlike Figure 20, results are normalized over the respective z_n bins. The clustering index (CI) is a commonly used metric (e.g., Baker, 1992; Chaumat & Brenguier, 2001; Jaczewski & Malinowski, 2005) that is defined as:

$$CI = \left(\frac{\sigma^2}{\bar{x}} - 1\right) \qquad\qquad 3)$$

where $\bar{x}$ is the mean and σ^2 the variance of a given parameter over a given number of samples. This metric takes advantage of the fact that a Poisson distribution has an equal mean and variance. By subtracting 1 from $\sigma^2/\bar{x}$, a droplet distribution sampled from a population with a constant mean rate will result in CI equaling zero, and CI will increase with increasing droplet heterogeneity. Note that CI less than zero ($\sigma^2 < \bar{x}$) is simply characterized as underdispersed (i.e., having a variance lower than that expected for a Poisson distribution). In this study, CI is calculated every second using 10 Hz observations, providing a measure of inhomogeneity over scales of ~120 m (depending on flight speed). In order to scale results on a logarithmic scale, the subtraction of 1 is removed from Eq. (2) so all results have a minimum possible value greater than zero. The altered calculation (i.e., altered clustering index; ACI) used in this study is given by:

$$ACI = \log_{10}\left(\frac{\sigma^2}{\bar{x}}\right) \qquad\qquad 4)$$

Figure 21A and 21C show ACI for N_{CDP} (ACI_N), whereas figure 21B and 21D show ACI for M_{CDP} (ACI_M). Joint histograms of ACI_N are relatively similar for layers from $0 < z_n < 0.8$, with most values ranging from -0.4–0.2 cm^{-3}. Near cloud base ($z_n = 0$), ACI_N varies

from ~0 to 1 cm^{-3} and average values are slightly greater than those from $0.2 < z_n < 0.8$.

Values increase near cloud top, with most ACI$_N$ between 0.5–2 cm^{-3}. Increased droplet

clustering has previously been found to occur at cloud top, which has been attributed to

mixing and cloud top entrainment in the past (e.g., Baker, 1992; Dodson & Small, 2019;

Small & Chuang, 2008).
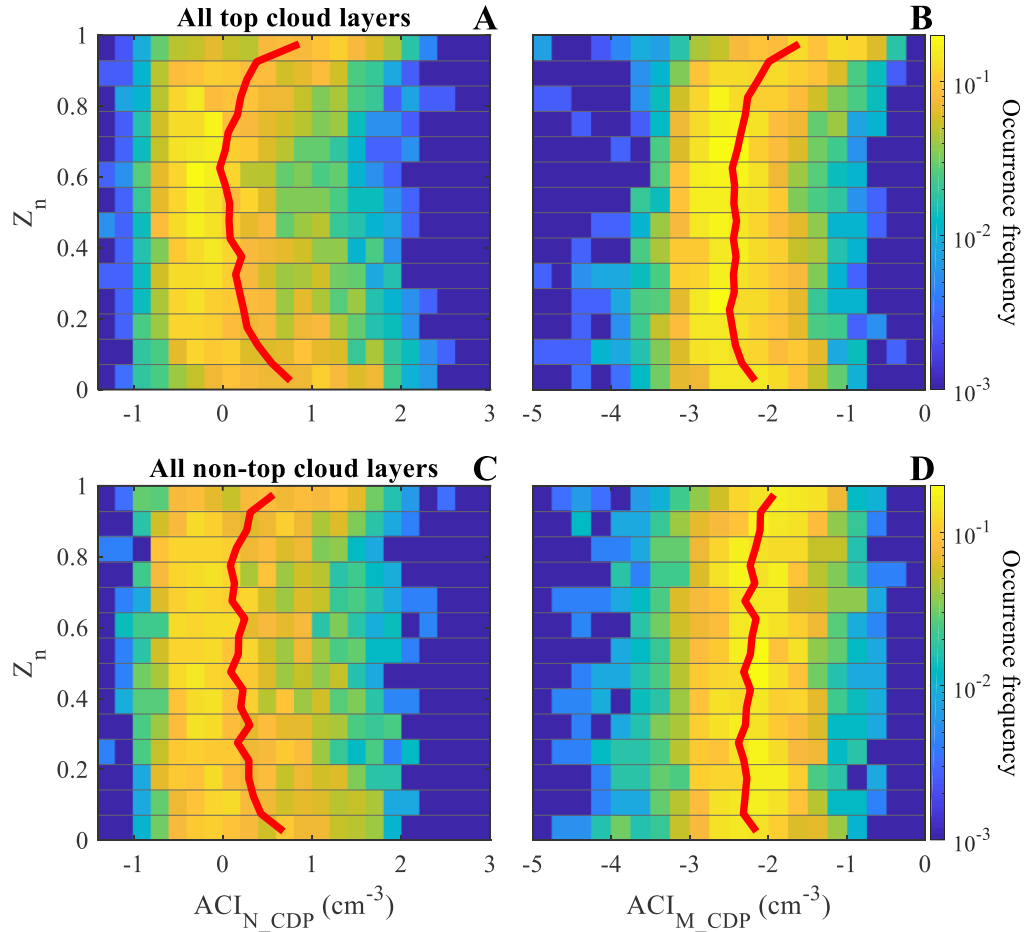
Figure 21: Joint histograms shown with ACI$_N$ (A,C) and ACI$_M$ (B,D) as a function of z_n for top cloud layers (top row) and non-top cloud layers (bottom row). Unlike Figure 20, histograms are normalized over respective z_n intervals. The red lines show average ACI$_N$ and ACI$_M$.

Mixing is often categorized as either homogeneous or inhomogeneous.

Homogeneous mixing characteristically results in a shift of drop size distributions

towards smaller drop sizes due to rapid mixing causing all droplets to experience partial

evaporation, whereas inhomogeneous mixing results in a reduction of droplet number concentrations but not in droplet sizes due to slower mixing causing different drops to experience different amounts of subsaturation (Baker et al., 1980; Latham & Reed, 1977). The above pertains to *extreme* inhomogeneous mixing (e.g., Korolev et al., 2016), whereas most mixing events do not necessarily follow one or the other extreme. Due to the different impacts of mixing on cloud top microphysical properties, examining how droplet concentrations and mass contents (derived from particle size distributions) vary can provide some information on the mixing characteristics. In fact, previous studies have attempted to characterize entrainment-mixing and its impacts based on drop size distribution inhomogeneities (Bower & Choularton, 1988; Paluch, 1986; Paluch & Knight, 1984).

Discernable differences in clustering at cloud top are observed between the top and non-top layers near cloud top, which may be due to differences in mixing strength. Namely, average ACI_N and ACI_M are greater at cloud top for the top cloud layers compared with non-top layers. The most notable differences are observed for ACI_M, where normalized occurrence frequencies greater than 0.1 exceed -1 only for the top cloud layers. In addition, the variability of ACI_M between cloud top and the underlying cloud is greater for top cloud layers than for non-top layers. Lower values of the clustering metrics at cloud top as well as lower variability of ACI_M between cloud top and the underlying cloud for the non-top cloud layers than for the top cloud layers is consistent with weaker mixing (i.e., more extreme inhomogeneous mixing). This is expected with lower cooling rates at the top of non-top cloud layers compared with top cloud layers (Figure 20C,F).

Other factors may account for the small scale variability of N_{CDP} and M_{CDP} at cloud top, such as previously observed generating cells (Wang et al., 2020) or upsidence waves (e.g., Rahn & Garreaud, 2010). The influence of upsidence waves on ACI_N is evaluated in Figure 22, which shows level leg cloud-top observations from two research flights.
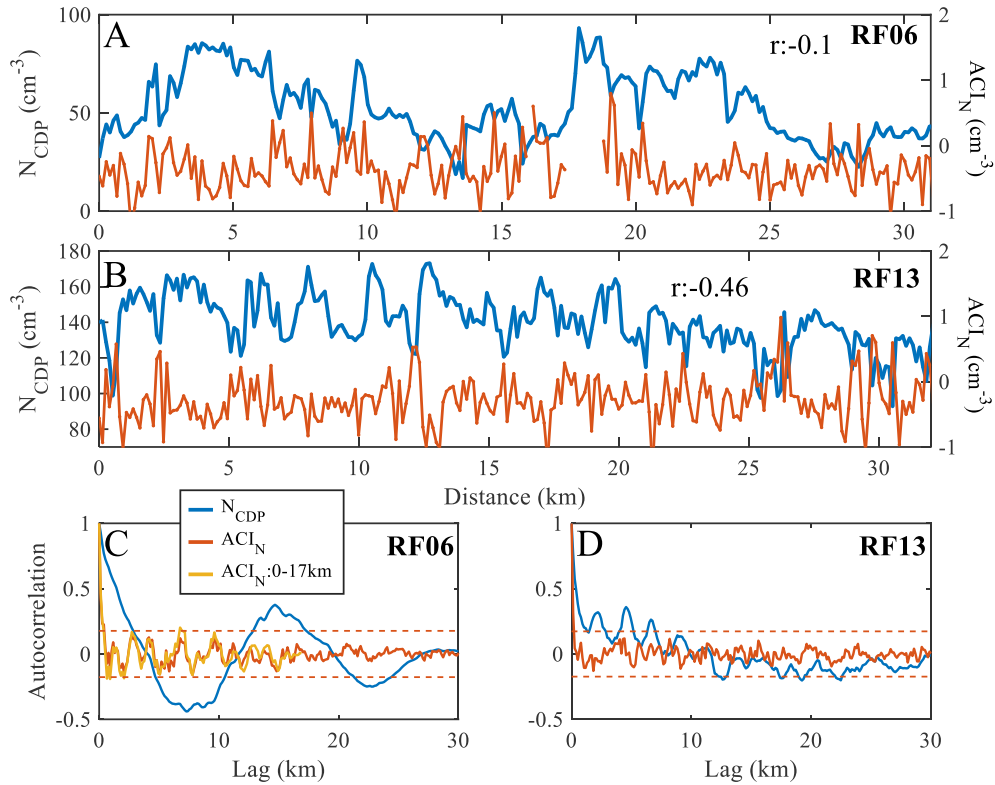
Figure 22: Two time series of level legs taken at cloud top showing N_{CDP} (blue) and ACI_N (red) from RF06 (01:47:00 to 01:51:55 UTC; A) and RF13 (02:19:00 to 02:24:00 UTC; B). Correlations are included in the respective panels. Autocorrelations of N_{CDP} and ACI_N are shown for RF06 (C) and RF13 (D). Bands for rejection testing each autocorrelation=0 under the assumption of white noise are shown as dashed lines, which are provided at the 95th percentiles. Autocorrelations are determined for flight data interpolated onto a 1D grid with a constant incrementally increasing distance (lag) of 130 m, based off the average flight speed for both cases (~130 m s^{-1}). The autocorrelation of ACI_N from 0–17 km is also provided for RF06, due to missing data from ~17.5–19 km (missing data is also observed at ~16 km, but the interpolation captures the fine scale variability).

Both cases reveal a wavelike structure in N_{CDP}, with a wavelength of ~15 km for RF06 (Figure 22A) and ~2 km for RF13 (Figure 22B). Autocorrelations of N_{CDP} for RF06

(Figure 22C) and RF13 (Figure 22D) capture the wavelike structures of N_{CDP}. For both cases, ACI_N does not possess the wavelike structures observed for N_{CDP}, which is observed when applying autocorrelations to ACI_N. A wavelike structure with a wavelength of ~1 km exists in RF06, but most amplitudes do not exceed the significance bounds. In contrast, autocorrelations exceed the significance bounds for N_{CDP} at lags comparable to the observed wavelengths. Correlations of N_{CDP} and ACI_N are -0.10 and -0.46 for RF06 and RF13, respectively. Increases in ACI_N often correspond with decreases in N_{CDP} (e.g., at 2.5 km and 12 km for RF13, Figure 22B), consistent with trends expected from entrainment-mixing.

Average normalized cloud particle size distributions, such that the integrated concentration equals one, are shown in Figure 23. Distributions include contributions from both the CDP and 2DS and are normalized over their combined range (2–1280 μm). To characterize their height variation, normalized particle size distributions are first interpolated to a 2D grid with z_n spaced over 0.01 intervals. Additionally, normalized particle size distributions are interpolated to the 2D grid over 80 logarithmically scaled bins ranging from 2–1280 μm. Results are then smoothed using a two-dimensional convolution and a 3x3 box kernel (i.e., averaging kernel). This method is analogous to that commonly used in image smoothing (e.g., Kim & Casper, 2013), allowing for a clear visual depiction of particle size distributions over the range of z_n. Focusing on the top cloud layers (Figure 23A), the maximum normalized $N(\log(D))$ (i.e., $dN/d\log(D)$) > 0.01 at $z_n < 0.1$ occurs at D from 2 to 20 μm. These maximum $N(\log(D))$ shift towards larger sizes with increasing z_n. At $z_n > 0.6$, maximum normalized $N(\log(D)) > 0.05$) occur at D from approximately 10 to 30 μm. This shift is consistent with droplet activation occurring

72

near cloud base producing small droplets, which grow with increasing height due to condensational growth and collision-coalescence.
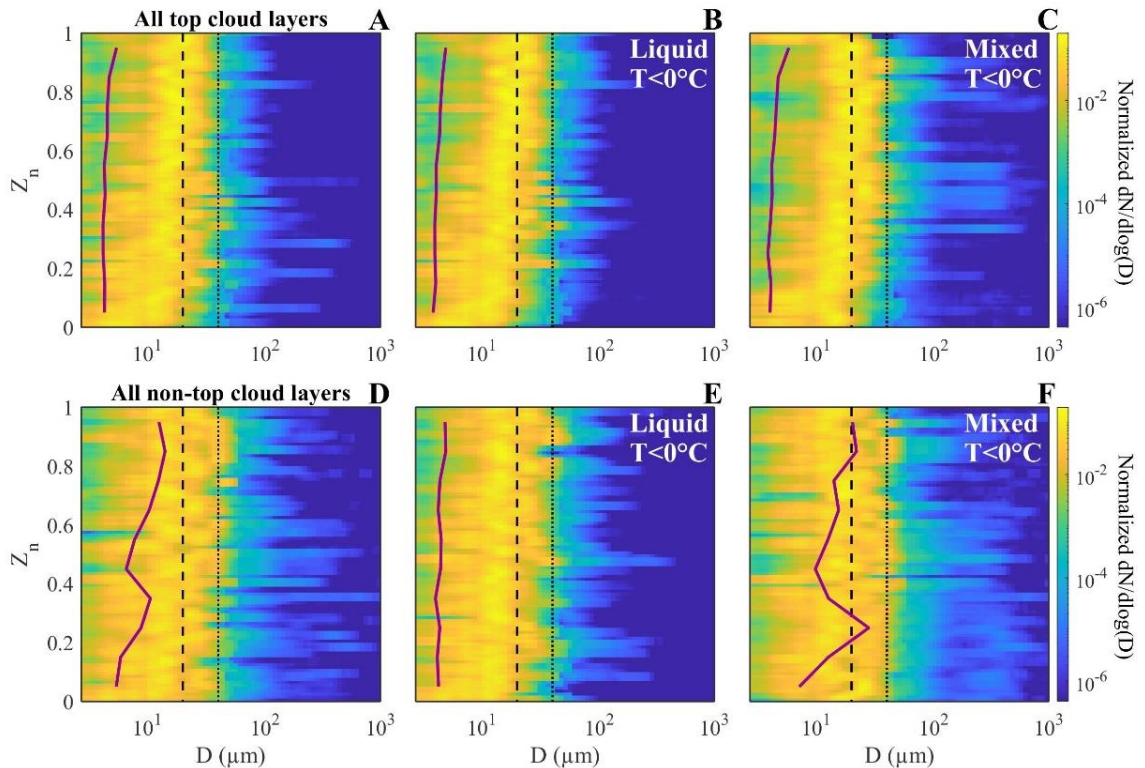
Figure 23: Normalized size distribution functions combining CDP and 2DS observations are averaged over z_n, using an image smoothing method outlined in the text. The top (bottom) row shows results for top (non-top) cloud layers. Results are shown for all in-cloud samples in the left column (A,D), liquid phase samples at temperatures less than 0°C in the middle column (B,E) and for mixed phase samples in the right column (C,F). Purple lines show the average standard deviation of particle size over the entire size distributions, applied prior to the convolution. The dashed and dotted lines correspond with D=20 μm and D=40 μm, respectively.

There are notable differences for the non-top cloud layers (Figure 23D) compared to the top cloud layers. The non-top layers have greater small droplet concentrations at z_n > 0.4 compared to the top layers with normalized N(log(D)) at D < 10 μm being ~0.05 throughout the entire cloud depth, whereas values at D < 10 μm decrease well below 0.01 for z_n > 0.5 in top cloud layers. Further, N(log(D)) greater than 0.01 reach sizes up to 40 μm throughout most of the cloud for non-top cloud layers. This is not seen for the top

cloud layers throughout most of the cloud. These trends highlight the differences seen in Figure 18C&D, namely that non-top cloud layers which only occur in multi-layer clouds have broader droplet size distributions. These broader distributions contain larger relative frequencies of both smaller ($D < 10$ μm) and larger (D from 30–50 μm) drops. Purple lines show the average σ of D for the normalized size distributions, and these values are larger for non-top cloud layers compared to top cloud layers over the entire depth. Normalized $N(\log(D))$ at $D > 50$ μm are also greater for the non-top cloud layers throughout the cloud depth.

Broader distributions are likely related to a greater frequency of mixed phase samples within non-top cloud layers, which may be associated with a broader range of ice crystals. This is suggested by plotting results separately for liquid phase samples (Figure 23B,E) and mixed phase samples (Figure 23C,F); normalized values of $D > 100$ μm are clearly greater for the mixed phase samples of both top- and non-top cloud layers compared with liquid phase samples. However, differences related to cloud phase do not account for all the observed differences between the layer types. Non-top cloud layers still have broader drop size distributions ($D < 50$ μm) than top cloud layers regardless of the cloud phase, which is likely due to particle interactions occurring vertically through local cloud layers. In fact, average ice concentrations in mixed phase samples with maximum dimensions exceed 200 μm (aspherical $N_{2DS\_D>200μm}$) are nearly an order of magnitude greater in non-top cloud layers (1.7 L^{-1}) than top layers (0.2 L^{-1}). The average σ are much lower for mixed phase samples in the top cloud layers compared with non-top layers. This is due to mixed phase samples in the top cloud layers having much greater drop concentrations (average $N_{CDP} = 120$ cm^{-3}) than non-top cloud layers (average N_{CDP}

= 40 cm^{-3}). Similarly, drop concentrations are greater in the top layers for liquid phase samples as well (average N_{CDP} = 110 cm^{-3}) than non-top layers (average N_{CDP} = 70 cm^{-3}), consistent with the lowest N_{CDP} observed for the lowest cloud layers in Figure 18A. The higher concentrations in top cloud layers are observed even when removing samples from coupled environments, which causes the average N_{CDP} of top layers to only decrease ~10 cm^{-3} for both phases.

3.7. Vertical distributions of phase and average cloud properties

In addition to characterizing multi-layer clouds based on the relative height within the cloud layer and based on whether in the top or non-top cloud layer, the relative frequency of liquid phase with respect to z_n can be analyzed as show in Figure 24. Results for multi-layer clouds are sorted by cloud height relative to the lowest cloud layer (as in Fig. 13&18; left panel) or by the lowest, highest and middle layers (right panel). Results for the lowest cloud layers (Multi-1st and Multi-lowest) are the same for both categorizations. Single-layer clouds are seen to contain the most liquid phase samples, which is consistent with Figure 13B. Further, the liquid phase frequency is the lowest for $z_n < 0.4$, which is similar to previous findings that Arctic single-layer mixed phase clouds contain the highest frequency of ice particles in the lower half of the cloud (e.g., McFarquhar et al., 2007; Mioche et al., 2017). The lowest cloud layers in multi-layer clouds have much lower liquid phase frequencies than in single-layer cases (consistent with Figure 13B), with liquid phase frequencies decreasing from 0.75 to 0.60 from cloud base to cloud top.
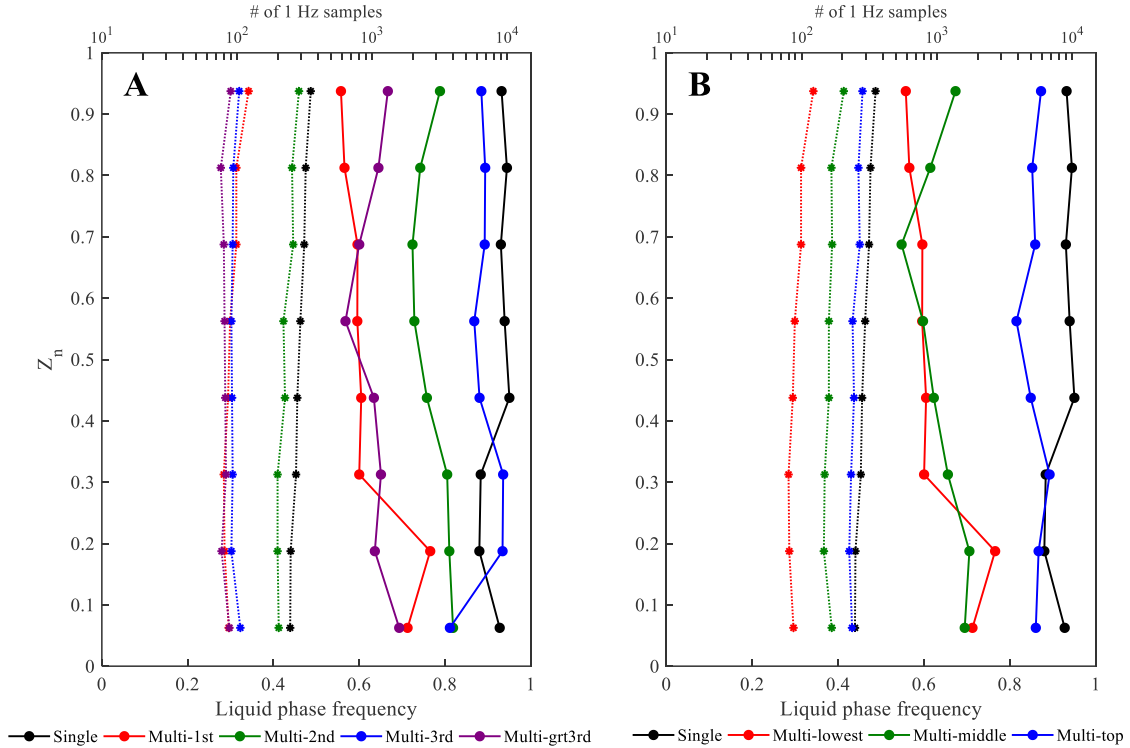
Figure 24: Cloud phase frequency as a function of z_n (solid lines) colored according to the cloud layer for single-layer and multi-layer clouds, where ordering of multi-layer height is characterized by incremental order from the lowest layer (A) and by whether layers are the lowest, highest, or in-between layer (B). Dotted lines show the number of samples for respective cloud layers following the top abscissa. Results are restricted to temperatures less than 0°C.

For multi-layer clouds, the second and third highest layers (Multi-2nd and Multi-3rd, respectively; Fig. 24A) have liquid frequencies varying between 0.75 to 0.95 throughout the normalized heights. Cloud layers overlying the third highest layers have lower frequencies which are comparable to the lowest cloud layers, varying from 0.55 to 0.70 throughout their depth. These layers typically occur at lower temperatures. Figure 24B shows results discriminating multi-layer clouds into the highest (Multi-top) and layers residing between the highest and lowest cloud layers (Multi-middle). The middle layers have much lower liquid phase frequencies compared with the top cloud layers. In fact, the liquid phase frequencies are comparable between the middle and lowest layers, whereas

76

the highest cloud layers have frequencies comparable to single-layers. The phase frequency structure of multi-layer clouds is consistent with what would be expected from a prominent seeder-feeder mechanism. Primary nucleation may occur at the highest cloud layers where temperatures are lowest, of which 61% were between -10° and 0°C and 78% between -20° to 0°C. Low liquid frequencies at cloud top of the lowest cloud layers may indicate seeding from above.

The remainder of the findings address how other microphysical properties vary as a function of z_n for the different layers, whose sample sizes are found in Figure 24. Figure 25 shows vertical profiles for single-layer clouds.
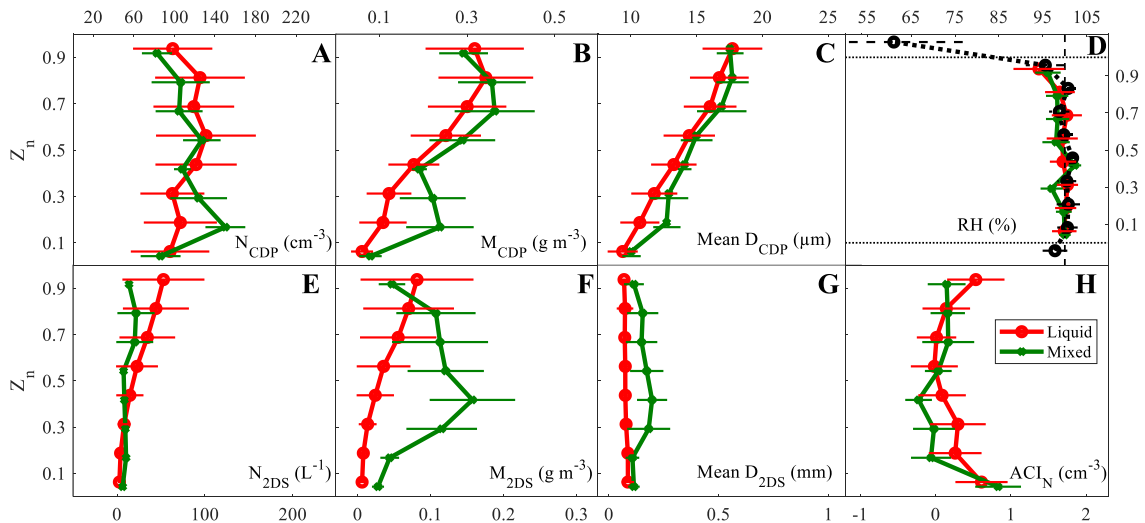
Figure 25: Averaged N_{CDP} (A), M_{CDP} (B), Mean D_{CDP} (C), RH (D), N_{2DS} (E), M_{2DS} (F), Mean D_{2DS} (G) and ACI_N (H) as function of z_n for single-layer cloud regimes. Horizontal lines are standard deviations. Results are shown for liquid phase samples with the red lines and mixed phase samples with the green lines. Properties are averaged within z_n bin sizes of 0.125. All panels show results for z_n between 0 and 1 except for RH (D), which includes additional bins above and below the cloud (dashed lines). Black circles in RH denote clear-sky samples.

Results are separately shown for liquid and mixed phase samples by the red and green lines, respectively. Ice phase samples are not included due to the relatively small sample size of ice phase compared with mixed phase samples (e.g., blue text in Figure 13B). The

top row shows N_{CDP}, M_{CDP} and number weighted mean diameter reported by the CDP (Mean D_{CDP}) (Figure 25A–C). All variables, with the exception of N_{CDP} for mixed phase samples, increase with height. The discussion for the remainder of this section focuses on liquid phase samples due to (1) the small sample size of mixed phase observations for all cloud layers and (2) the fact that such observations do not necessarily represent a secondary vertical structure, because the majority of mixed phase samples were embedded within primarily liquid phase cloud layers.

Figure 25E-G shows vertical profiles for the properties of particles with dimensions greater than 50 μm (N_{2DS}, M_{2DS} and Mean D_{2DS}). Both N_{2DS} and M_{2DS} increase with z_n, whereas Mean D_{2DS} decreases with z_n. Note that M_{2DS} and Mean D_{2DS} are larger for mixed phase throughout most of the cloud depth, consistent with the coexistence of larger particles which are primarily ice. Mixed phase Mean D_{2DS} were separately determined for spherical and non-spherical particles greater than 200 μm, and Mean D_{2DS} for non-spherical particles were greater than spherical particles at all z_n (not shown). Figure 25H shows ACI_N, which has a U-shaped distribution similar to Figure 21A&C meaning that maximum ACI_N are at cloud base and cloud top. Vertical profiles of RH in Figure 25D are ~100% throughout the cloud depth, with a deviation of ~95% at cloud top. Black dots with dashed lines show RH for clear-sky regions which primarily occur above cloud top ($z_n > 1.0$). Since the layer classification allows for clear-sky samples to exist within a profile, such samples (although very few) may occur within a cloud layer ($0 < z_n < 1$). RH is also shown above cloud top and below cloud base ($z_n > 1$ and $z_n < 0$, respectively). Above cloud top and below cloud base data is simply the neighboring 1 Hz clear-sky samples to the respective cloud edges. Clear-sky samples below cloud base are nearly

saturated, whereas clear-sky samples above cloud top have an average RH of 60%, with significant variability (standard deviation of ~25%).

Figure 26 shows vertical profiles for the lowest cloud layer in multi-layer clouds. Similar to single-layers, M_{CDP}, Mean D_{CDP}, and N_{2DS} all increase with height. Average ACI_N and Mean D_{2DS} have similar distributions, with peak values near cloud top and cloud base for ACI_N and decreasing values with height for Mean D_{2DS}.
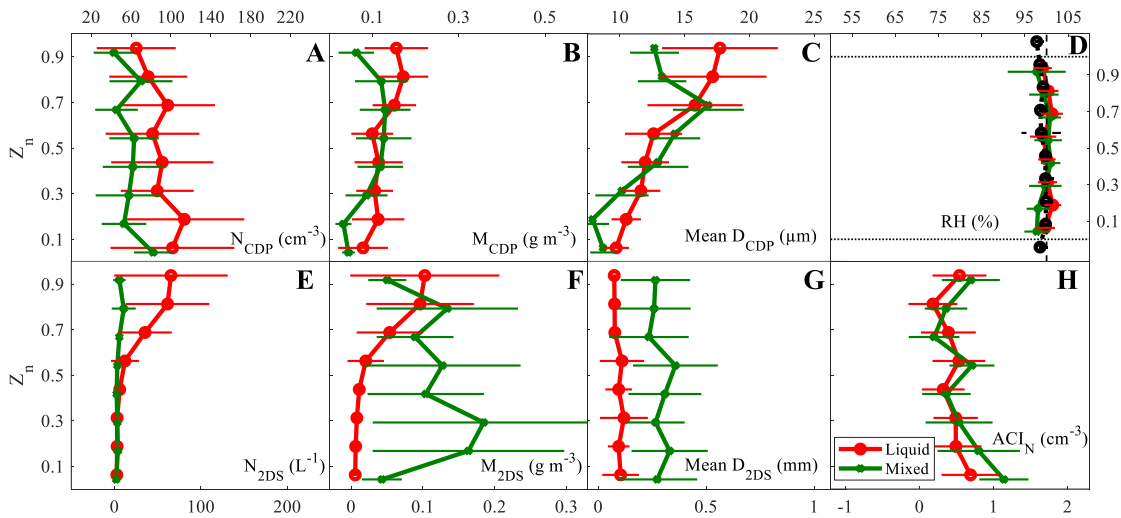
Figure 26: Similar to Figure 25 except for the lowest layer of multi-layer clouds. Differences between the cloud layer types are primarily observed for N_{CDP} and RH, where N_{CDP} roughly decreases with height and clear-sky RH above cloud top is nearly saturated (~96%) with little variance (standard deviation~3%) for the lowest layer in the multi-layer clouds.

Figure 27 shows a similar analysis for the top cloud layers (Figure 27A–D), the non-top cloud layers (Figure 27E–H), and middle layers (Figure 27I–L) of multi-layer clouds. Average N_{CDP}, Mean D_{CDP}, N_{2DS} and RH are shown for the layer types. N_{CDP} increases with increasing height and peaks above z_n=0.5 for top cloud layers, and below 0.5 for non-top layers. When removing single-layer clouds from the top cloud layer

analysis, N_{CDP} similarly peaks above $z_n = 0.5$ (supplementary Figure I). Mean D_{CDP} increases with height for all layer types. However, differences are observed in the overlying clear-sky RH for the top and non-top layers.
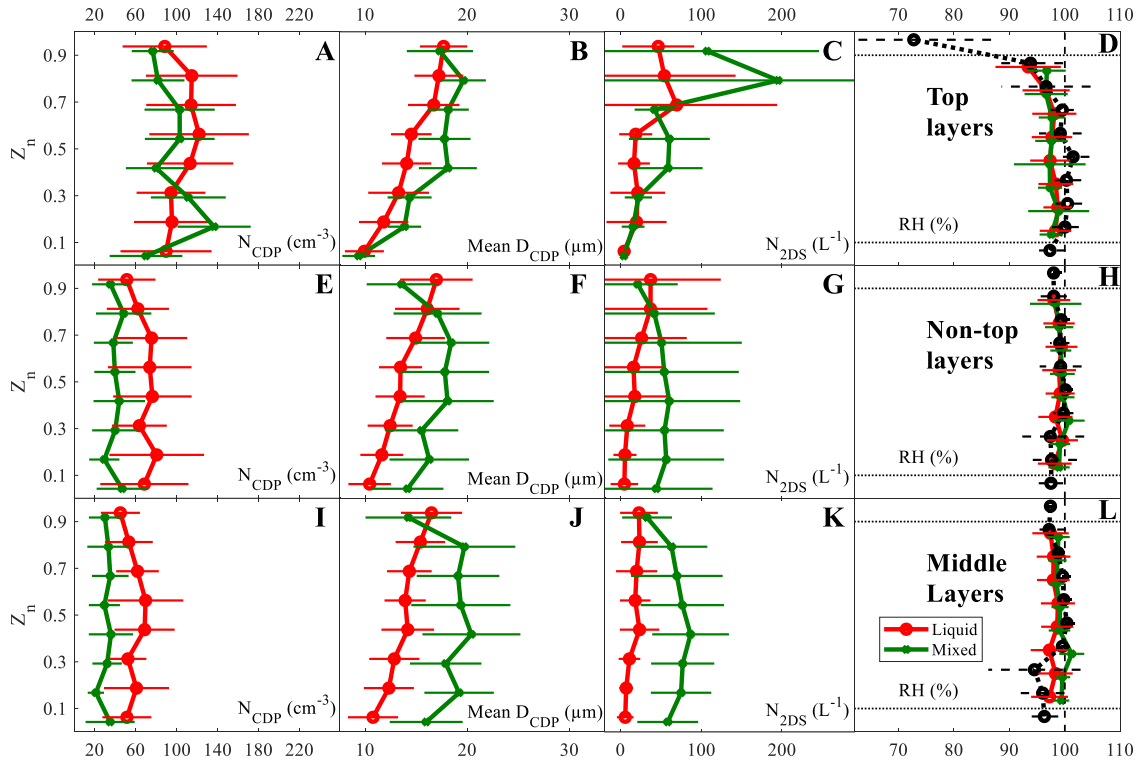
Figure 27: Similar to Figure 25&26 except results are shown for the top cloud layers (A–D), non-top cloud layers (E–H) and for all cloud layers enclosed within the lowest and highest cloud layers of multi-layer clouds (I–L). Unlike Figure 25&26, results here are only shown for N_{CDP} (A,E,I), Mean D_{CDP} (B,F,J), N_{2DS} (C,G,K) and RH (D,H,L).

Similar to the differences in single- and lowest multi-layer clouds (Figure 25D,26D), the air is nearly saturated above non-top cloud layers while RH is only ~70% above top layers. When separately evaluating highest multi-layer clouds and removing single-layer clouds from the analysis, the overlying RH is ~90% (supplementary Figure J). The saturated air overlying non-top cloud layers may be an important feature, as previous modeling studies have shown the presence of humidity inversions are required to maintain low-level mixed phase clouds in the Arctic (e.g., Curry, 1986; Curry et al.,

1988; Solomon et al., 2011). Differences in overlying RH may be expected as single-layer clouds will often be capped by rather strong inversions, whereas layers above one another will be associated with weaker inversions. In contrast, reduced longwave cooling at cloud top will be associated with underlying cloud layers of multi-layer regimes rather than top cloud layers.

The nearly saturated conditions above cloud top could also be associated with evaporating drizzle or sublimating ice from overlying cloud layers. This may be unlikely, since conditions are still nearly saturated immediately above cloud top for layers separated by distances exceeding a kilometer from the overlying cloud layer (not shown). However, following Pruppacher & Klett (1996) and Lamb & Verlinde (2011), a spherical ice particle ranging from D=50 to 150 um in environments having RH with respect to ice ranging from 60% to 80% at temperatures ranging from -20° to 0°C results in ice particles which can fall for distances ranging tens of meters to ~1.5 km before completely sublimating. In this study, cloud top observations less than 200 m from the overlying cloud layer account for 47% of the cases, and observations less than 1 km from the overlying cloud accounts for 86%. A potential source of uncertainty could be associated with how cloud top and cloud base are determined using the layer classification scheme, namely, using a threshold value of $M_{CDP} > 0.01$ g m^{-3} at the highest and lowest point of a given profile. Slight deviations in actual cloud top could account for differences in the overlying RH measurements, as well as differences in cloud top microphysical properties which either peak at the highest or second highest normalized height bins (as seen for Mean D_{CDP}, N_{2DS} and M_{2DS} amongst different cloud layers in Figures 25–27).

Differences in overlying RH between top and non-top layers are consistent with differences in cloud top ACI_M (Figure 21B,D). Namely, inhomogeneous mixing is characterized by slower mixing relative to homogeneous mixing, whereby partial regions of cloud are evaporated and consequently saturate the air which mixes with nearby cloud and preserves large particle sizes. The mixing of nearly saturated air would have a diminished impact of drop populations compared with considerably subsaturated air. This is also consistent with the expected weaker mixing at cloud top for non-top cloud layers due to weaker cloud top radiative cooling.

Despite these differences (including differences in drop clustering in Figure 21), droplets greater than 50 μm are observed at cloud top of all layer types with average concentrations ranging from ~20–50 L^{-1} (as well as mass, although only shown for single- and lowest cloud layers; Figure 25F,26F). Since mean D_{2DS} increases from cloud top towards cloud base, this suggests collision-coalescence may begin near cloud top. Greater degrees of cloud top droplet clustering could potentially contribute to the greater large drop concentrations due to increased collision likelihoods as well as screening effects (e.g., Castellano & Ávila, 2011). The average drop size of particles greater than 50 μm increases towards cloud base, which is consistent with increased collision-coalescence as droplets fall through the cloud. However, other factors may contribute to the common occurrence of droplets exceeding 50 μm, such as sea salt acting as giant CCN (e.g., CCN with maximum dimensions exceeding 2 μm; Jensen & Nugent, 2017).

3.8. Conclusions

The microphysical properties of single- and multi-layer clouds over the Southern Ocean were evaluated and contrasted using airborne in situ observations acquired during

SOCRATES. Cloud layers were classified using a novel smoothing method applied to in-situ cloud observations on ramped ascents and descents of the aircraft. This resulted in 55 profiles of single-layer clouds and 183 profiles of individual multi-layer clouds. Single-layer clouds have greater cloud liquid droplet mass and number concentrations than multi-layer clouds, with number concentrations in single-layer clouds from two research flights in coupled environments approximately double those in decoupled environments. This is consistent with the impact of an increased supply of CCN from the ocean surface. Multi-layer clouds have broader drop size distributions than single-layer clouds. When cloud layers are separated according to whether they are underlying other cloud layers (non-top cloud layers) or not (top cloud layers), non-top cloud layers have broader drop size distributions (D < 50 μm) and total particle size distributions throughout the vertical cloud depth compared to top cloud layers.

The liquid phase most frequently occurs in single-layer clouds compared with multi-layer clouds. Liquid phase frequencies in multi-layer clouds are the lowest in the lowest cloud layers and increase with higher cloud layers until the third highest layer is reached, suggesting a prominent seeder-feeder presence in multi-layer clouds. When classifying the layers of multi-layer clouds as lowest, highest, and those lying in-between, the highest cloud layers have the greatest frequency of liquid phase samples, and the middle layers have similarly low relative frequencies as the lowest layers. These findings show that caution should be taken when quantifying cloud phase frequencies solely from satellite imagery due to potential biases in cloud top phase as well as overlapping cloud layers, as well as caution in classifying phase frequency by temperature alone.

Relative phase frequencies are also explored in relation to on CCN and INP concentrations. There is evidence of ice frequencies strongly correlating with INP concentrations (e.g., a correlation of -0.6 is observed for INP with activation temperatures from -30° to -10°C and liquid phase frequencies from -20° to -2°C in the boundary layer), but it is only observed for select temperature and activation temperature ranges. This may be due to difficulties collocating the datasets, as well as insufficient sample sizes. Phase frequencies are found to be directly related to CCN concentrations, but only above the boundary layer. Ice is more likely to be observed in environments with low CCN concentrations. Results also suggest high CCN concentrations may inhibit large droplet growth due to a competition principle and may impede the Hallet-Mossop process.

The dependence of cloud microphysical properties on cloud layer normalized height are also examined. The number weighted mean diameter of drops less than 50 μm increases with height for all cloud layer types, whereas number concentrations peak near cloud top for top cloud layers and near cloud base for non-top cloud layers. The number concentration and mass of drops greater than 50 μm also increase with cloud height, whereas the mean diameter decreases with increasing height. These similarities are observed between single- and multi-layer clouds in spite of differences in cloud top droplet clustering, radiative cooling profiles, overlying RH and relative phase frequencies, highlighting a propensity for precipitation initiation in both single and multi-layer clouds. However, robust differences in the microphysical properties of single- and multi-layer clouds warrants further investigation to distinguish and constrain physical responses resulting in the differences provide here.

4   Impacts of drop clustering and entrainment-mixing on mixed phase shallow cloud properties over the Southern Ocean: Results from SOCRATES

4.1. Introduction

Mixed phase clouds, where liquid and ice particles occur in the same sample volume, have been observed in maritime and continental regions ranging from the tropics to the poles (Cossich et al., 2021; Costa et al., 2017; Hogan et al., 2003; Korolev et al., 2003; McFarquhar et al., 2007; Mioche et al., 2015; Morrison et al., 2011; Wang et al., 2021), and can be associated with cloud types ranging from thin stratiform layers to deep convective clouds (Korolev et al., 2017). The common occurrence and even persistence (Morrison et al., 2012) of mixed phase clouds is unexpected due to differences in the saturation vapor pressure of liquid and ice. When liquid and ice particles are present, ice should grow at the expense of liquid drops, commonly known as the Wegener-Bergeron-Findeison (WBF) process (Bergeron, 1928; Findeisen, 1938; Wegener, 1911).

Mixed phase clouds are ubiquitous over the Southern Ocean (D'Alessandro et al., 2019, 2021; Huang et al., 2012, 2021; Mace et al., 2021; Morrison et al., 2011). Large errors in simulated shortwave radiative flux common for climate models over this region has been attributed to the incorrect representation of mixed phase clouds, and primarily to an underrepresentation of supercooled liquid (Bodas-Salcedo et al., 2016; Naud et al., 2014). However, recent model updates approximately capture and likely overestimate observed supercooled liquid frequencies (Gettelman et al., 2020; Yang et al., 2021). In addition, climate models often over-estimate WBF, resulting in unrealistic glaciation rates (Tan & Storelvmo, 2016). Correctly simulating mixed phase clouds is crucial

towards improving both weather and climate models because of their impact on precipitation (Mülmenstädt et al., 2015) and radiation (Sun & Shine, 1994).

Previous theoretical and modeling studies considered the impacts of turbulent mixing on mixed phase properties. For example, Korolev & Mazin (2003) found that liquid could persist within a vertically oscillating mixed phase air parcel and that liquid could form within an ice cloud when the vertical velocity exceeds a critical threshold. These findings are consistent with those from Hill et al. (2014) using a large-eddy simulation model and from Heymsfield (1977) using doppler radar and airborne measurements. Less work has explored impacts of entrainment-mixing on mixed phase properties, although one recent study (Hoffmann 2020) utilized a millimeter resolution linear eddy model to show that entrainment can enhance the WBF process due to increased droplet evaporation if is not offset by the spatial inhomogeneity of phase within the mixed areas.

Cloud top entrainment is important to quantify as it controls the evolution of macro- and microscale features of low-level clouds. Entrainment rates are directly related to vertical gradients of temperature, humidity and radiative cooling directly overlying the cloud (Houze, 2014; Mellado, 2017). When considering the impacts of entrainment-mixing on microphysical properties, it is common to characterize mixing events as homogenous or inhomogeneous (Latham & Reed 1977; Baker et al. 1980) as these two alternative mixing schemes result in different pathways for the evolution of drop size distributions. Homogeneous mixing is associated with vigorous mixing of dry air into cloudy regions, resulting in all droplets undergoing at least partial evaporation. Inhomogeneous mixing is associated with weaker mixing. As dry air is slowly mixed within the cloud, a few drops will be preferentially evaporated to return the entrained area

to near saturation. Inhomogeneous mixing typically has a greater impact on drop concentrations than on sizes. In contrast, homogeneous mixing has a greater impact on average drop sizes since all droplets are at least partly evaporated. The former is associated with drop size distributions having decreasing concentrations at all sizes, whereas the latter is often characterized by a shift of the distribution towards smaller sizes.

The Damköhler number is commonly used to characterize the type of mixing and to determine the impact of entrainment on cloud microphysical properties. It is defined as:

$$Da = \frac{\tau_m}{\tau_r} \hspace{4cm} 5)$$

where τ_m is the turbulent mixing time (i.e., eddy turnover time) and τ_r is the response time of the microphysical properties to mixing. When the response time of the cloud particles is much slower than the mixing time, Da<<1 which indicates homogenous mixing. In contrast, cloud particles rapidly reacting to weak entrainment events will result in Da>>1 which indicates *extreme* inhomogeneous mixing. The τ_m is expressed as:

$$\tau_m = (L^2/\varepsilon)^{\frac{1}{3}} \hspace{4cm} 6)$$

where L is the length scale of the entrained eddy (i.e., dry air) and ε is the turbulent dissipation rate. Calculations of τ_r vary depending on whether the evaporation time (τ_{evap}), phase relaxation time (τ_{phase}), or reaction time (τ_{react}) is chosen, as each expression is associated with different assumptions. Thus, τ_r is more ambiguous than τ_m (e.g., Gao et al., 2018; Lu et al., 2018). Further discussion of homogeneous and inhomogeneous mixing can be found in Devenish et al. (2012) and Korolev et al. (2016).

Although a considerable amount of work has characterized mixing in warm

clouds, often examining drop size broadening and the potential for rain initiation (e.g., Grabowski & Wang, 2013; Jensen & Baker, 1989; Lasher-Trapp et al., 2005; Tölle & Krueger, 2014), little work has similarly been done for mixed phase clouds. This study provides an observational evaluation of entrainment-mixing impacts on mixed phase cloud properties. Section 4.2 describes the instrumentation used and relevant analysis techniques. Sections 4.3&4.4 evaluates the relationship between drop clustering and multiple measures of entrainment-mixing, which forms the basis of using clustering as a proxy to broadly diagnose the intensity of entrainment mixing. Section 4.5 relates clustering to mixed phase cloud properties to assess the impacts of mixing. The last two sections (4.6&4.7) include additional discussion and concluding remarks.

4.2. Instrumentation

This study uses observations acquired with instruments onboard the National Science Foundation/National Center for Atmospheric Research Gulfstream-V (GV) aircraft during the Southern Ocean Cloud-Radiation Aerosol Transport Experimental Study (SOCRATES). The cloud droplet probe (CDP) and the two-dimensional stereo probe (2DS) are used to obtain the cloud bulk microphysical properties for cloud particles having D less than and greater than 50 μm, respectively. Samples are determined to be in-cloud or clear-sky following D'Alessandro et al. (2021). Additionally, the phase of in-cloud samples is determined following D'Alessandro et al. (2021), which determines the phase of small cloud particles (D<50 μm) using a set of threshold values for the CDP and Rosemount Icing Detector measurements, whereas the phase of large particles (D>50 μm) is determined using multinomial logistic regression as well as visual examination of particle imagery from the 2DS (details of which are provided in Section 2.2). This study

88

only uses time periods identified as liquid or mixed phase. Analysis in this study is restricted to samples with $N_{CDP} > 5$ cm^{-3}, which are assumed to represent liquid droplets.

The phase of a 2DS sample can be classified as either liquid, ice or mixed. Since all CDP observations used in this chapter are liquid, a cloud sample is considered mixed phase if the 2DS is classified as mixed or ice phase. Cloud particle size distributions combine CDP and 2DS size distributions, corresponding to cloud particles less than and greater than 50 μm, respectively. When the 2DS sample is ice phase, liquid bulk properties are derived from the CDP and ice bulk properties are derived from all 2DS particles. For 2DS mixed phase samples, liquid bulk properties are derived from the CDP and from 2DS particles identified as spherical, whereas bulk properties of ice are derived from non-spherical particles. However, ice particles can appear spherical due to variations in particle orientation and shape. Because of this, mixed phase samples must have a number concentration ratio of round particles having D > 100 μm to all particles with D > 100 μm greater than 0.3 to apply the bulk properties as described. Otherwise, all particles greater than 100 μm are classified as ice. This is based off work from Cober & Isaac (2012) and directly taken from Schima et al., (2022). Note that this only applies to particles greater than 100 μm. Particles from 50–100 μm are classified as ice or liquid if they are non-spherical or spherical, respectively.

Additional instrumentation includes the Rosemount temperature probe for determining air temperature, and the wind components are measured using the Radome Gust Probe in combination with pitot tubes and the differential Global Positioning System. Cooper et al. (2016) reports a net uncertainty in the standard measurements of the horizontal wind components of 0.4 m s^{-1} and the uncertainty in vertical wind

measurements of $0.12 \, \text{m s}^{-1}$, although this represents ideal sampling conditions. Additional information on the GV gust probe performance and processing is provided in the manager's report (EOL, 2018).

4.3. Entrainment-mixing and clustering calculations

To calculate τ_m, ε is determined using equations 11 and 12 from Meischner et al. (2001), which are discussed in further detail in Appendix A. The calculation of L follows Gao et al. (2021), namely:

$$L = F \times TAS/f \qquad\qquad 7)$$

where TAS is true air speed of the aircraft, f is the sampling frequency and F is the fraction of clear-sky observations within each 1 Hz sample, determined using 10 Hz observations. Clear-sky samples in Gao et al. (2021) were defined as droplet free, whereas a less stringent definition of derived mass content less than 10^{-3} g m^{-3} is applied here (D'Alessandro et al. 2021). The calculations of τ_r for the liquid and mixed phase follow Pinsky et al., (2018) (shown in Appendix A), where both expressions are phase relaxation times expressing the time for reaching equilibrium conditions between the condensate and vapor content. These expressions of τ_r are inversely proportional to the particle mean radius and number concentrations.

Two clustering metrics are used in this study. The clustering index (CI) is a commonly used metric to quantify cloud droplet clustering, whose application in cloud microphysics was first introduced in Baker (1992). CI takes account of the fact that a uniform Poisson distribution will have the variance (σ^2) equal to the mean of a given quantity ($\bar{x}$). Thus, CI will equal zero for a perfectly homogeneous distribution and will diverge from this value with increasing heterogeneity. A potential caveat of CI is its inherent volume dependence, where CI contains "memory" of varying spatial scales

within the sample volume (further discussed in Shaw et al., 2002). The volume average pairwise correlation (VAPC) is introduced to partially offset this dependence and reduce scale memory:

$$\text{VAPC} = \frac{1}{\bar{x}}\left(\frac{\sigma^2}{\bar{x}} - 1\right) = \frac{1}{\bar{x}}(\text{CI}) \qquad 8)$$

where CI is weighted by the average quantity. Similar to ACI, an altered VAPC (AVAPC) is introduced as:

$$\text{AVAPC} = \log_{10}\left(\frac{\sigma^2}{\bar{x}^2}\right) = \log_{10}(\frac{1}{\bar{x}}(\text{CI} + 1)). \qquad 9)$$

For this study, 10 Hz observations are used to determine ACI and AVAPC at 1 Hz resolution. Clustering results are applied to N_{CDP} (ACI_N and AVAPC_N).

4.4. Droplet clustering as a proxy for mixing

Analysis in the following section shows that applying a clustering method on a relatively coarse spatial scale (~100 m) can give a direct, qualitative description of the degree of mixing. Higher values of cloud drop clustering indices have commonly been observed at cloud edges previously (e.g., Beals et al., 2015; Dodson & Small Griswold, 2019; Small & Chuang, 2008), including for Southern Ocean clouds (D'Alessandro et al., in preparation). Clustering can be related to localized turbulent flows, where droplets cluster in low vorticity regions (Shaw et al., 1998).

Figure 28 shows the relationship between the clustering metrics and Da at cloud top. Following D'Alessandro et al. (in preparation), cloud top samples are identified as those in-cloud data from ascending and descending flight legs where the normalized cloud height (z_n) exceeds 0.975. Although the decrease of AVAPC_N with Da is more pronounced than for ACI_N, both clustering metrics show positive correlation with mixing strength (i.e., low Da). Additionally, all samples having Da>1 is consistent with most

prior studies commonly observing inhomogeneous rather than homogeneous mixing (e.g., Andrejczuk et al., 2009; Beals et al., 2015; Burnet & Brenguier, 2007; Gao et al., 2021), especially at the relatively large mixing length scales used here (Burnet & Brenguier, 2007; Kumar et al., 2018; Lehmann et al., 2009). However, the relationship between ACI_N and Da is quite weak. In fact, previous studies have used other mixing measures in conjunction with Da to characterize mixing due to a wide range of observed Da (e.g., Burnet & Brenguier, 2007; Kumar et al., 2014; Lu et al., 2011; Yum et al., 2015). One reason for this is that there is no commonly accepted method for determining the eddy length scale. Further, Lehmann et al. (2009) noted that multiple eddy length scales (and thus mixing time scales) will exist for a subsequent entrainment-mixing event.
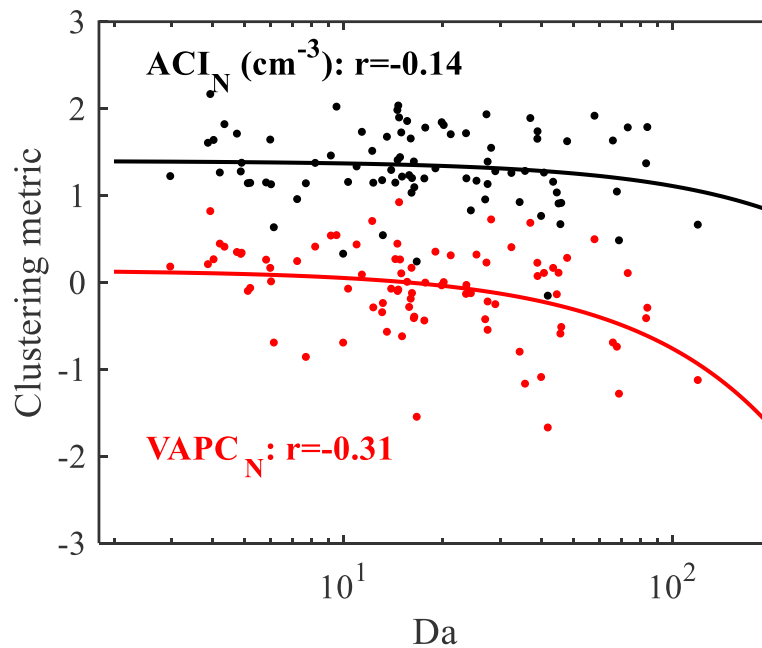
Figure 28: The clustering metrics ACI_N (black markers) and $AVAPC_N$ (red markers) versus Damköhler number. Results are shown for 1 Hz observations at all cloud tops as determined in D'Alessandro et al. (in preparation), where cloud top is defined as z_n greater than 0.975. Respective correlations are shown in the plot. Note that only samples with clear-sky fraction (F) greater than 0 are included in the plot (otherwise Da=0).

Because of this, they introduce the transition length scale (L^*), where values greater

(lower) than the measured eddy length scale is indicative of homogeneous (inhomogeneous) mixing. It is defined as:

$$L^* = \varepsilon^{\frac{1}{2}} \tau_r^{\frac{3}{2}} \qquad 10)$$

where Lehmann et al. (2009) argue τ_r should use the lower time scale between τ_{phase} and τ_{evap}. Values of L^* are determined for SOCRATES observations and similar to Lehmann et al. (2009), most values are on the order of meters and lower, much shorter than the sampling length scales of this study. For liquid phase conditions, τ_{evap} is taken from Rogers & Yau (1996) and for mixed phase conditions, τ_{evap} is replaced by the glaciation time (i.e., time for the total amount of liquid water to convert to ice) taken from Hoffmann (2020). These expressions are discussed further in Appendix A.

Other mixing measures often include mixing diagrams relating drop size, mass and number concentrations to their respective adiabatic values. Relating actual to adiabatic properties can give insight to the strength of entrainment-mixing, since adiabatically derived values assume the respective air parcel does not mix with the surrounding environment. In order to evaluate clustering in relation to adiabatically derived quantities, Figure 29A shows the clustering metrics as a function of the ratio of the observed mass content at cloud top ($M_{CDP+2DS}$) over the adiabatic mass content ($M_{adiabatic}$). Both ACI_N (black points) and $AVAPC_N$ (red points) show a strong negative relationship with the adiabatic mass ratio (correlation of -0.62 for ACI_N and -0.74 for AVAPC), showing that the degree of clustering can be directly related to the degree of mixing. Similar to the dependence of clustering index on Da, a stronger correlation is found for $AVAPC_N$ than for ACI_N. Nevertheless, ACI_N is used to determine the degree of mixing for the duration of the study because ACI_N is less dependent on N_{CDP} (r = -0.08)

than $AVAPC_N$ ($r = -0.47$). This is seen when comparing the clustering metrics and N_{CDP} in Figure 29C,D. The entire range of $AVAPC_N$ shifts towards smaller sizes with increasing N_{CDP}, whereas the range of ACI_N is relatively constant for all N_{CDP}. Results are colored by the number weighted mean diameter (mean D_{CDP}) in Figure 29C,D. Distinct modes are seen for mean D_{CDP}. For N_{CDP} greater than 40 cm^{-3}, the mean D_{CDP} varies from 15–25 μm and the majority of samples (65%) occur here.
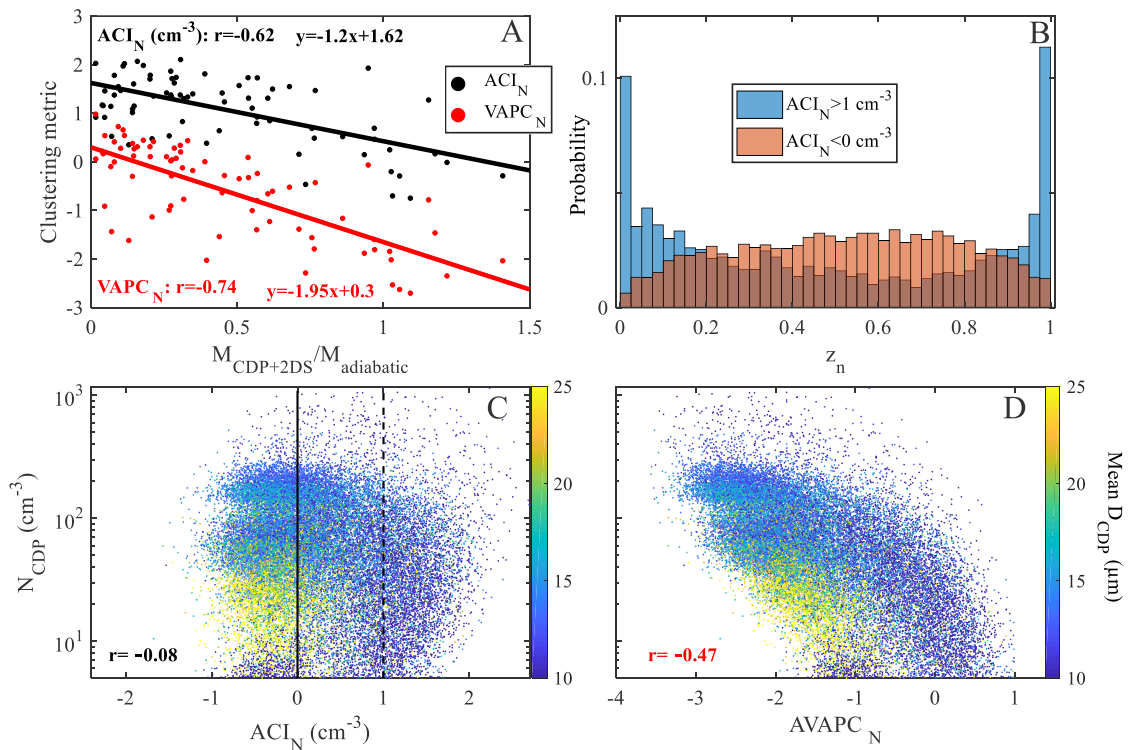
Figure 29: (A) The clustering metrics ACI_N (black markers) and $AVAPC_N$ (red markers) related to the ratio of the actual and adiabatic cloud mass. Results are shown for 1 Hz observations at cloud top similar to Figure 28, but only for single-layer clouds with thicknesses greater than 30 m. Unlike Figure 28, results include samples with clear-sky fraction (F) greater than and equal to 0. First order polynomial best fit lines as well as correlations are shown for the respective clustering metrics. (B) Normalized frequency distributions of z_n for different ranges of ACI_N. Unlike A), z_n is taken from single and multi-layer clouds for all layer thicknesses. Bins for z_n are at 0.025 intervals. (C) ACI_N and (D) $AVAPC_N$ related to N_{CDP}. Results are colored by mean D_{CDP}. The solid and dashed vertical lines in C) correspond to $ACI_N = 0$ cm^{-3} and $ACI_N = 1$ cm^{-3}, respectively, which are used as threshold values for low and high ACI_N in (B).

For $N_{CDP} < 40$ cm^{-3}, higher mean D_{CDP} (>25 μm) occur at low clustering values and lower mean D_{CDP} (<10 μm) occur at high clustering values. The low mean D_{CDP} and high ACI_N are primarily cloud edge samples where $z_n<0.1$ and $z_n>0.9$, which is shown by the normalized frequency distributions of z_n at high ACI_N in Figure 29B (blue bars). In contrast, the high Mean D_{CDP} are primarily within the cloud core as shown by z_n at low ACI_N in Figure 29B (orange bars). These high Mean D_{CDP} are primarily precipitating samples (including drizzle and ice), as 70% of these points detected the presence of particles on the 2DS with $D > 200$ μm (not shown). This shows that precipitating samples within on near the cloud core are associated with higher $AVAPC_N$ than many non-precipitating samples having low mean D_{CDP} at higher N_{CDP} (e.g., all samples having $AVAPC_N$ below -2.5), since they are weighted by lower values of N_{CDP}. Although ACI_N is used to diagnose mixing, the choice of clustering metric is inconsequential since exchanging ACI_N with $AVAPC_N$ throughout the analyses of this study show similar trends.

Droplet clustering impacts processes such as precipitation initiation (Shaw et al., 1998), evolution of raindrop distributions (McFarquhar, 2004), and ice crystal growth (Castellano et al., 2004; Castellano et al., 2008). However, clustering relevant to such mechanisms is associated with spatial scales orders of magnitude smaller (~1 cm) than that presented here (~100 m). To determine the direct relationship between the presence of ice and drop clustering, drop clustering in liquid and mixed phase samples are compared. Figure 30A shows normalized frequency distributions of ACI_N for liquid and mixed phase conditions as red and blue shading, respectively. Mixed phase results are separately shown for different ice concentrations with $D > 200$ μm. This threshold is chosen due to depth of field uncertainties and insufficient bit resolutions at lower sizes

(e.g., Baumgardner et al., 2017). Distributions are relatively similar, although the liquid

phase results are slightly more kurtotic and the mixed phase results have a slight peak at 1

cm^{-3}. Distributions for different ice concentration ranges are relatively similar to those of

liquid and total mixed phase samples.
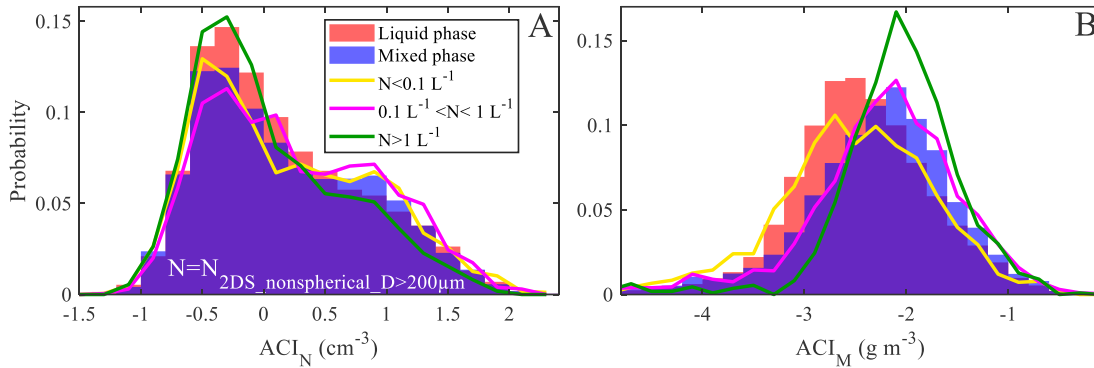
Figure 30: Normalized frequency distributions of ACI_N (A) and ACI_M (B) shown for different cloud phases (shaded colors). The colored lines show normalized frequency distributions for mixed phase results with varying ice concentrations exceeding 200 μm.

Perhaps unexpectedly, mixed phase conditions with the greatest number of ice particles

have distributions most resembling the liquid phase. This is seen using the sum of the

absolute difference in the bin values (i.e., Euclidian distance) for the liquid phase and

high ice concentration distributions (0.034), compared with the mixed phase and high ice

concentration distributions (0.053). Mann-Whitney U-tests and Kolmogorov-Smirnov

tests are performed to test the similarity of the distributions for the varying ice

concentration ranges. These tests are chosen since they do not require prior knowledge of

the distributions' shapes. Results suggest there is no statistically significant difference

between the distributions of the two lower ice concentration ranges with the mixed phase

distribution, as well as between the highest ice concentration range and the liquid phase

distribution. Specifically, both tests do not reject the null hypothesis, namely, that the

distributions are similar, at a significance level of 5%.

Normalized frequency distributions of clustering calculated using M_{CDP} (ACI_M) are shown in Figure 30B and test whether ACI_M may be preferred to ACI_N for the mixing analysis. The distribution of ACI_M for mixed phase samples is clearly shifted towards greater values than for the liquid phase, with a mode approximately 1 g m^{-3} greater. Compared with ACI_N, the Euclidian distance between the liquid and mixed phase bin values is a factor of 2 greater (0.09) than ACI_N (0.04). Figure 29B also shows that the ACI_M distributions shift towards higher values with increasing ice concentrations. The sum of the Euclidian distances between the mixed phase and all of the different ice concentration ranges for ACI_M is also higher by a factor of 2 (0.20) than for ACI_N (0.11). Since the liquid and mixed phase distributions are more comparable for ACI_N, and no apparent bias associated with ice concentrations is observed for ACI_N, mixing is qualitatively determined using drop number rather than drop mass clustering.

An initial analysis using ACI_N as a proxy for entrainment-mixing is shown in Figure 31. Particle size distributions (PSDs) are averaged over different ranges of ACI_N for the liquid phase (A–C) and mixed phase (D–F). Results are separated into different ranges of N_{CDP}. For both phases, the greatest differences in the PSDs for different ACI_N is seen for N_{CDP} less than 40 cm^{-3} (Figure 31A,D), where PSDs are shifted towards smaller sizes with increasing ACI_N. Distributions are most identical at the highest N_{CDP}, which show the greatest deviations at the smallest drop sizes (D<7 μm) for varying ACI_N. This is confirmed by taking the Euclidian distance of the normalized PSDs (i.e., dividing each bin by the sum of the total distribution function), when summed for the PSDs at N_{CDP}<40 cm^{-3} is a factor of 2.5 greater than for PSDs at N_{CDP}>80 cm^{-3}. This shift is observed for all particle sizes in the liquid phase, but only for particles less than 400 μm in the mixed phase. Drizzle drops do not likely reach sizes larger than ~400 μm at

temperatures less than 0°C due to the potential for aircraft icing. This suggests a resilience of large ice crystals from sublimating, which is consistent with a replenishing water vapor supply from evaporating liquid.
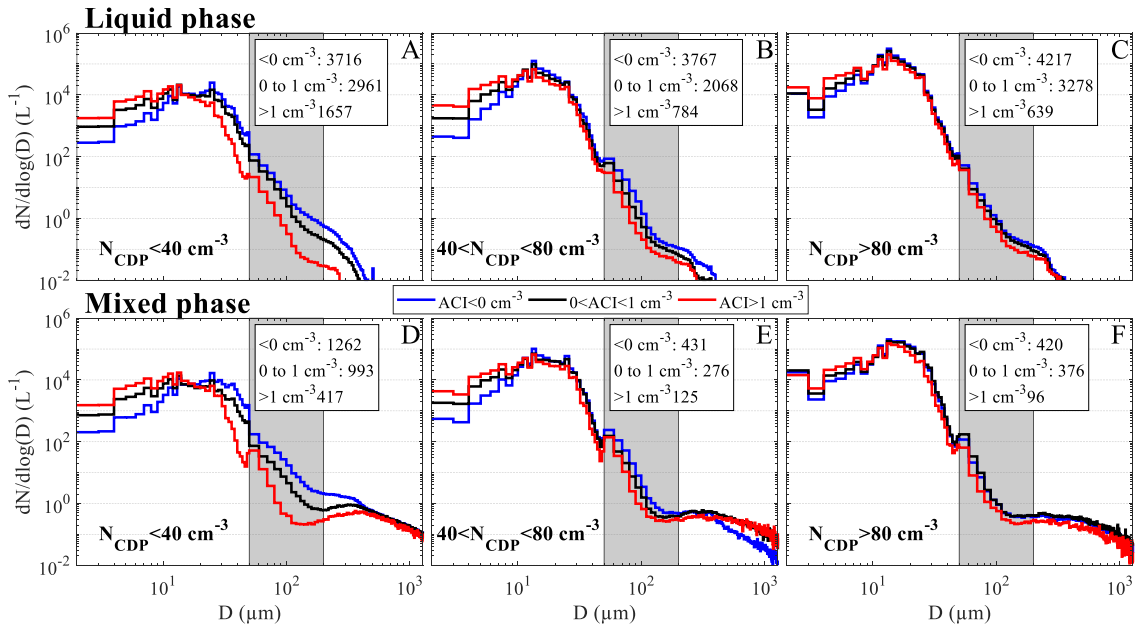
Figure 31: Average PSDs for the liquid phase (A–C) and mixed phase (D–F) shown for different ranges of ACI_N by the different colored lines. Results are shown for different ranges of N_{CDP} in the respective columns. The number of samples are shown in the respective panels. Gray shading from 50–200 μm represents particle sizes associated with depth of field uncertainties (e.g., Baumgardner et al., 2017).

The distribution shift towards smaller sizes with larger ACI_N is consistent with condensate loss due to evaporation and sublimation. However, this shift is characteristically attributed to homogeneous mixing, whereas inhomogeneous mixing typically causes a decrease in the number distribution functions at all particle sizes (i.e., a downward shift in the PSDs) (e.g., Korolev et al., 2016). This appearance of homogeneous mixing can be a consequence of combining PSDs from varying environments. For example, when a cloud with average $N_{CDP} > 80$ cm^{-3} has an entrainment-mixing event that decreases the local drop concentration to less than 40 cm^{-3}

it would be included in the left column. This is consistent with PSDs of $N_{CDP} < 40$ cm^{-3} and high ACI_N having high number distribution functions at $D < 10$ μm, which are more similar to PSDs of $N_{CDP} > 80$ cm^{-3} compared with lower ACI_N, assuming larger particle concentrations primarily decrease. Mixed phase results in the following section may suggest this. This is also suggested by high ACI_N number distribution functions of $D > 100$ μm in $N_{CDP} < 40$ cm^{-3} liquid phase samples being the most similar to those at $N_{CDP} > 80$ cm^{-3} ($N(\log(D)) < 10^{-1}$ L^{-1}) compared to lower ACI_N.

To address this potential discrepancy (i.e., the appearance of prevalent homogeneous mixing), results must account for the background cloud and environmental properties. This is done by analyzing results relative to average quantities of cloud transects, which are regions of neighboring samples. Transects are defined by consecutive in-cloud samples having $N_{CDP} > 5$ cm^{-3}. Transects are split so that (1) the number of 1 Hz observations never exceeds 10 and (2) transect lengths are at least 1 km. For example, a set of 66 neighboring in-cloud samples would be split into 6 transects having 10 samples and one transect of 6 samples. If one of the transects has a length less than 1 km, it is discarded. This results in 1781 transects having lengths ranging from 1– 2.1 km, with 86% of transects having lengths from 1200–1500 m. Quantities will be prefaced with "average" (e.g., average ACI_N) when referring to transect data, or referenced to by their quartile values (e.g., $N_{CDP} > 50^{th}$ percentile).

The average ACI_N and average $AVAPC_N$ are shown in relation to the N_{CDP} 20th and 80th percentiles for all transects in Figure 32A and 32B, respectively. To provide an all-encompassing analysis of mixing and maximize the sample size, in-cloud data is included in the analysis regardless of their proximity to cloud edge. Both ACI_N and $AVAPC_N$ increase as points diverge from the 1:1 line. This is consistent with greater

mixing and resulting evaporation of available condensate within localized regions of the transects, represented by points further from the 1:1 line where the 20th and 80th percentiles of N_{CDP} are more different, and thus where values of clustering are capturing cloud filaments on the order of meters produced by entrainment-mixing events. Figure 32C,D shows the covariance of the clustering metrics for the N_{CDP} 20th and 80th percentiles for all transects. The vast majority of values are negative (>85%) and increase in magnitude with greater divergence of the N_{CDP} percentiles. This shows that clustering and N_{CDP} within most transects are negatively correlated (i.e., clustering is primarily correlated to the low N_{CDP} samples rather than high N_{CDP} within the respective transects), consistent with clustering localized to regions of low droplet concentrations resulting from entrainment-mixing processes. Mixing for increasing divergence in the N_{CDP} percentiles is also evident in Figure 32E, which shows points colored by average Mean D_{CDP}. The lowest average Mean D_{CDP} are observed at the greatest differences in the N_{CDP} percentiles, consistent with decreasing drop sizes due to evaporation.

Mixing diagrams relating droplet concentration and volume weighted mean radius (r_v) have commonly been used in the past to distinguish homogeneous from inhomogeneous mixing (e.g., Burnet & Brenguier, 2007; Lehmann et al., 2009; Pawlowska et al., 2000) as homogeneous mixing is associated with greater variability of r_v. This variability is analyzed in Figure 32F, which shows points colored by the difference of the 80th and 20th percentiles of r_v. The difference in r_v percentiles does not increase in magnitude with increasing difference of N_{CDP} percentiles, but rather with decreasing total N_{CDP} (both 80th and 20th N_{CDP} percentiles decreasing). This irregularity highlights why studies often use complementary measures of mixing alongside N-r_v relationships (e.g., Gerber et al., 2008; Lehmann et al., 2009). Many of these points with

low N_{CDP} have the highest average Mean D_{CDP} associated with precipitation (discussed in reference to Figure 29C,D).
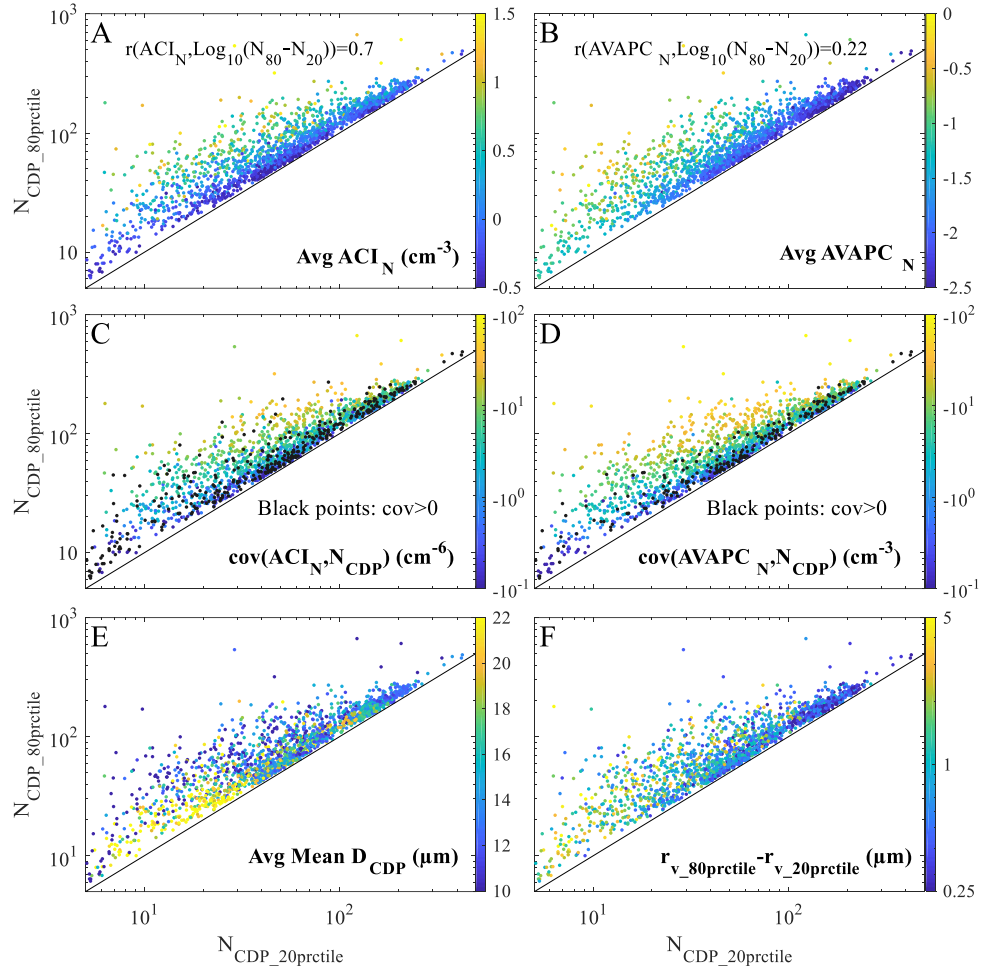
Figure 32: Scatter plots of the 80th percentile N_{CDP} and 20th percentile N_{CDP} for transect data. Results are colored by average ACI_N (A), average $AVAPC_N$ (B), covariance of ACI_N and N_{CDP} (C), covariance of $AVAPC_N$ and N_{CDP} (D), average mean D_{CDP} (E) and the difference of the 80th and 20th percentiles of the volume weighted mean radius (r_v; F). The black line represents the 1:1 line.

Further, average ACI_N and $AVAPC_N$ are the least similar at low N_{CDP}, where average $AVAPC_N$ are relatively high regardless of the difference in N_{CDP} percentiles. Many of these relatively high values of $AVAPC_N$ overlap with the high Mean D_{CDP} associated with precipitation. In addition, the correlation of clustering with the log-scale difference in the 80th and 20th N_{CDP} percentiles is much greater for ACI_N despite not having results

101

directly weighted by N_{CDP} as for $AVAPC_N$ (shown in Figure 32A,B), which is likely due to differences at log average N_{CDP}. These findings highlight the reason for choosing to use average ACI_N for the remaining analysis.

Figure 32 has shown that droplet clustering is directly related to differences in the background droplet concentrations. To relate the transects directly to mixing measures, Figure 33 shows average ACI_N related to average L and τ_m. Droplet clustering is significantly correlated with average L (r=0.53), consistent with the negative covariance of average ACI_N and low N_{CDP} within transects (Figure 32C). Clustering is also positively correlated with τ_m, which considers the instantaneous turbulent motions directly related to ε.
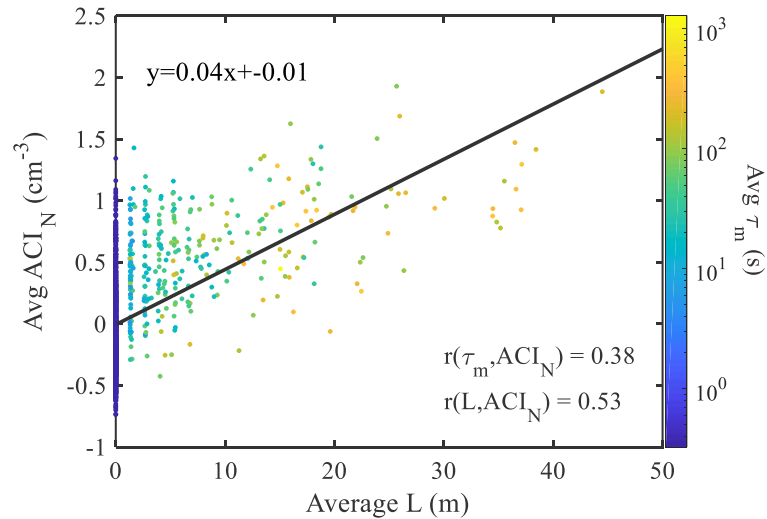
Figure 33: Transect average ACI_N related to the average length scale (L). Results are colored by the average mixing relaxation time (τ_m). Correlations between average ACI_N and the two averaged mixing variables are shown in the panel, as well as a 1st order polynomial best fit line.

Multiple benefits are associated with utilizing clustering as a proxy variable. It allows for an indirect estimation of L by obtaining an approximation of F without relying on a stringent clear-sky threshold, since clustering is associated with lower number

concentrations resulting from evaporation (Figure 32A–D). This allows for low N_{CDP} gaps between cloud filaments, which may not meet the stringent "droplet-free" condition, to be considered in the mixing analysis. This method also maximizes the total number of available samples. Other methods such as controlling results by the mass content over the adiabatic mass content similarly limits the possible sample size by limiting observations to regions adiabatic values can be derived. This also applies to other metrics such as entrainment rate, which is generally restricted to the entrainment interfacial layer. Further, ambiguous assumptions and uncertainties in determining entrainment rates (Chen et al., 2011; Romps, 2010; Wood, 2012) and Da are avoided. An additional benefit associated with the use of transects is that results are directly applicable to weather and climate models having comparable horizontal grid sizes (~1 km). The following section presents findings incorporating the use of transects to characterize the impacts of mixing.

4.5. Impacts of entrainment-mixing

Figure 34 shows average PSDs for liquid phase (A–C) and mixed phase (D–F) samples. Figure 34 differs from Figure 31 in that results are organized by different ranges of 1 Hz ACI_N as well as average ACI_N, with the largest averages in the right column. Transects expected to be associated with stronger mixing events are in the right column, whereas weaker or nonexistent mixing is associated with the left panels.

Percentiles of 1 Hz ACI_N meeting the conditions within each respective panel are shown as the different colored PSDs. The PSDs organized by 1 Hz percentiles are relatively similar within each respective panel, suggesting relative homogeneity amongst 1 Hz ACI_N within transects. However, notable differences are observed between the PSDs within the varying panels. For both phases, higher percentiles of 1 Hz ACI_N (>80th; red

lines) generally have lower number distribution functions for D > 50 μm at average ACI_N

greater than the 30th percentile compared with lower ACI_N percentiles (black and blue

lines; Fig. 34B,C,E,F). For mixed phase samples, this trend is only observed from 50–300

μm for average ACI_N 30th to 70th percentiles and from 50–200 μm for above the 70th

percentile (Figure 34E,F).
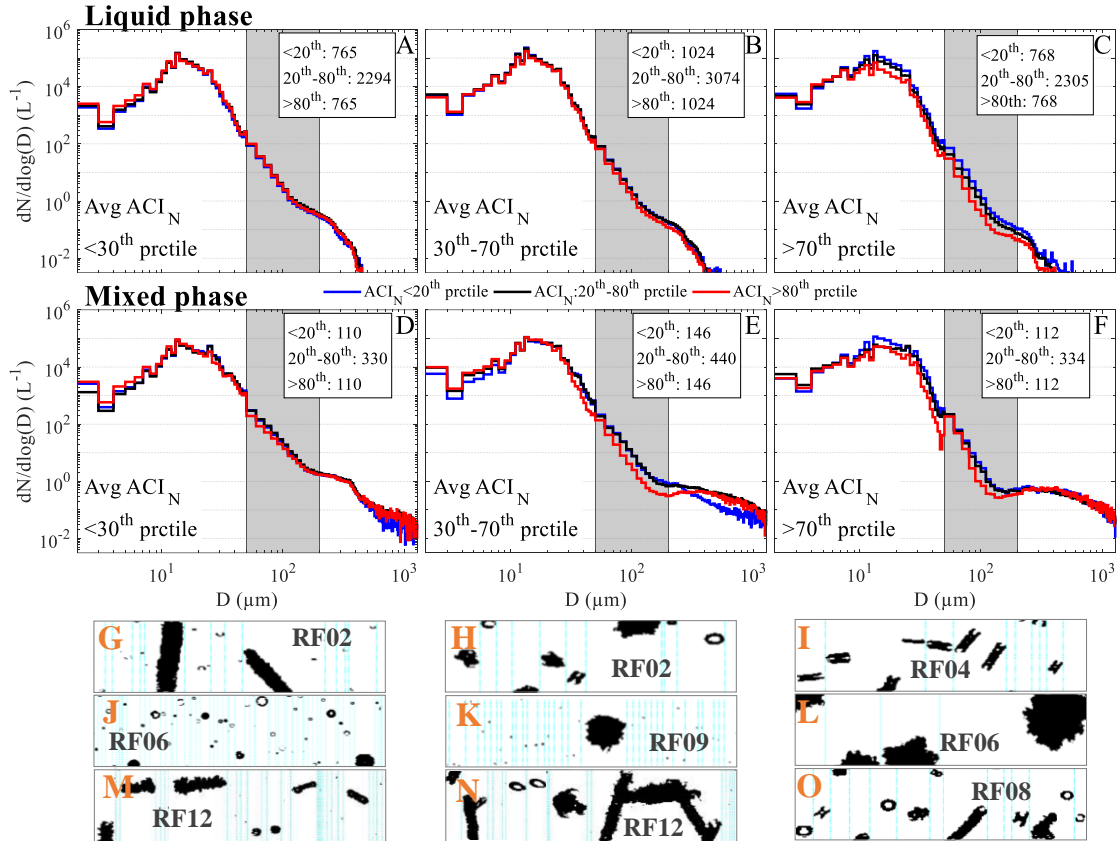
Figure 34: Average PSDs for liquid (A–F) and mixed phase (D–F) samples. Results are separated by percentiles of transect average ACI_N for each column. Different colored lines represent varying percentiles of 1 Hz ACI_N associated with the respective transect average ACI_N percentiles. Images underlying each column show representative cases of 2DS cloud particle imagery for the respective average ACI_N percentiles.

Lower number distribution functions of 1hz ACI_N > 80th are also seen from 10–50 μm,

most notably at average ACI_N greater than 70th percentile. These lower N(log(D)) for

greater 1 Hz ACI_N is characteristic of inhomogeneous mixing, which was not evident in

Figure 31 when transect data were not used.

The most distinguishing differences of PSDs are observed over different ranges of average ACI_N. For the liquid phase, PSDs are relatively similar amongst the different ranges, with the greatest differences observed at the largest drop sizes. Number distribution functions of large drops (D greater than ~40 μm) decrease with increasing average ACI_N, consistent with evaporation from entrainment. The PSDs for mixed phase conditions are much more variable amongst average ACI_N compared with the liquid phase. The most notable trend is the difference in the number distribution functions of large particles between average ACI_N less than and greater than the 30th percentile. Less than the 30th percentile, N(log(D)) from ~100–400 μm are observed at 1–10 L^{-1}, and rapidly decrease to 0.1 L^{-1} and lower at sizes greater than 600 mm (Figure 34D). This peak is primarily attributed to samples from mixed phase drizzle associated with the second and sixth research flights (RF02&06, respectively). Representative particle imagery for the different ranges of average ACI_N are shown underlying the respective columns, and the cases shown for RF02 and RF06 highlight these drizzle cases within the lower average ACI_N transects. Drizzle from RF02 occurred together with large ice crystals as seen in Figure 34G, whereas drizzle from RF06 occurred mainly in the absence of ice with the exception of a few cases of small graupel, seen as the aspherical particles in Figure 34J. Number distribution functions from ~400–800 μm increase with increasing average ACI_N (> 30th percentile) by a factor of 3–5. This is consistent with enhanced WBF due to droplet evaporation, which was also noted by Hoffmann (2020). The 1 Hz ACI_N from the 30th to 70th average ACI_N percentiles (Figure 34E) capture this transition, namely, N(log(D)) at D > 400 μm increase above the 20th percentile, and a "dip" occurs between ~100–200 μm. This dip is shown below to be likely related to the

removal of large drops.

Strong mixing events are further examined in Figure 35, where mixed phase results greater than the 70th percentile are separated into 70th–80th (A), 80th–90th (B) and greater than 90th (C) percentiles. Although there is no clear average ACI_N threshold that categorically defines the presence of entrainment-mixing, the right-most panel with the highest ACI_N in Figure 35 shows the clearest downward shifts in PSDs amongst 1 Hz ACI_N percentiles (expected with inhomogeneous mixing; Fig. 34F).
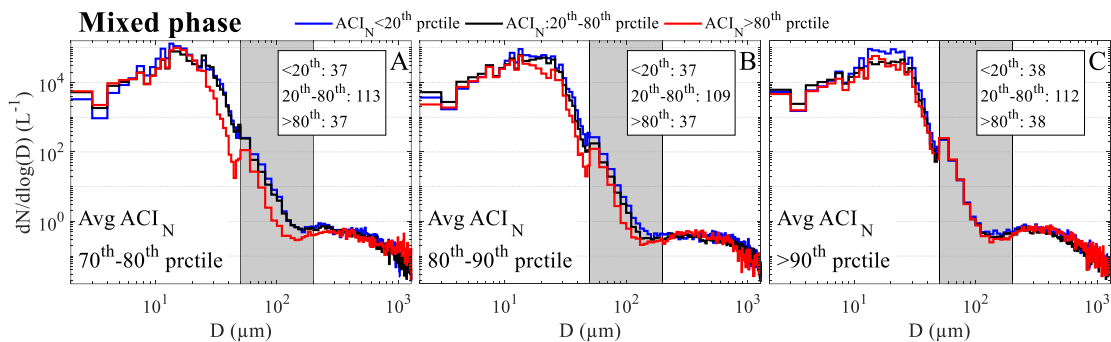
Figure 35: Similar to Figure 34, except results from Figure 34F are separated into 3 average ACI_N percentile ranges.

This adds confidence towards relating the strength of entrainment-mixing to mixed phase properties. Number distribution functions for D greater than 300 μm increase with increasing average ACI_N. Most notably, number distribution functions slightly increase from 300–500 μm, where N(log(D)) vary from 0.3–0.8 L^{-1} (0.2–0.5 L^{-1}) above (below) the 90th percentile of average ACI_N. In addition, mixed phase PSDs have less prominent peaks at ~15 μm and a slight broadening from 15–25 μm with increasing average ACI_N, which although observed in Figure 34D–F is more pronounced here. Overall, drop number distribution functions for D <10 μm are relatively similar when compared amongst the average ACI_N percentiles, whereas relatively larger drops may be preferentially evaporating, as seen by an approximate order of magnitude decrease in

number distribution functions at 50 μm with increasing ACI_N.

To evaluate how results vary for different temperatures, mixed phase results for average ACI_N greater than 30th percentile are separated into different temperature ranges in Figure 36, with lower (higher) temperatures at A&B (C&D).
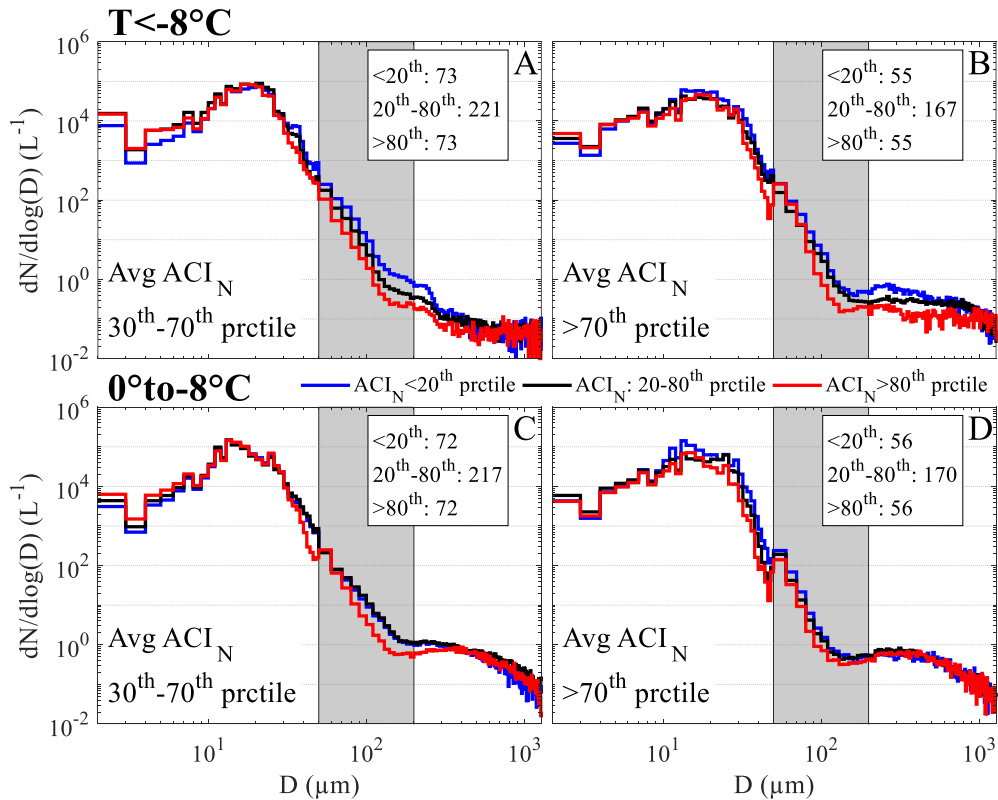
Figure 36: Similar to Figure 34, except results are only shown for mixed phase at temperatures less than -8°C (A,B) and greater than -8°C (C,D).

Similar to Figure 34, downward shifts of PSDs for greater 1 Hz ACI_N percentiles at larger average ACI_N (indicative of inhomogeneous mixing) are observed for both temperature ranges. Number distribution functions for D>400 μm are relatively similar for varying ACI_N at temperatures greater than -8°C, which may suggest weak mixing is sufficient to induce an enhanced WBF process. This would be consistent with increased N(log(D)) at D>400 μm for average ACI_N above the 30th percentile (Figure 34D,E). It may also suggest an enhanced WBF process is more prevalent at lower temperatures, where the

107

difference between the liquid and ice saturation vapor pressures is greater. This is consistent with number distribution functions at temperatures less than -8°C, outside the Hallett-Mossop secondary ice crystal production zone (Hallett & Mossop, 1974), which markedly increase at ACI_N greater than the 70th percentile.

Findings of the increasing number distribution functions of large ice with increasing average ACI_N have thus far been attributed to entrainment-mixing events enhancing WBF. Considering that the characteristic pathway of the WBF process is the transition of liquid to ice, the liquid water content (LWC) over the total water content (TWC; ice and liquid) would be expected to transition from 1 to 0 during these events. Thus, if an enhanced WBF process were present, a hypothetical set of mixed phase samples would more likely be associated with lower values of LWC/TWC compared to a weak WBF process. Figure 37 directly relates average ACI_N to 1 Hz mixed phase samples within the transects for all temperatures (Figure 37A), temperatures less than -8°C (Figure 37B) and temperatures greater than -8°C (Figure 37C). The joint histogram is normalized over each average ACI_N bin. For all temperatures, the frequency of LWC/TWC at 0.9–1.0 gradually decreases from ~0.9 to 0.2 as average ACI_N increases from -0.6 to 1.0 cm^{-3}. The frequency of lower LWC/TWC correspondingly increases with increasing average ACI_N as well, having frequencies skewed towards higher LWC/TWC at low average ACI_N and more uniformly distributed at high average ACI_N. Results in Figure 37B&C examine the impacts of temperature related to differences such as the greater difference in liquid and ice saturation vapor pressures at lower temperatures, as well as the potential of enhanced ice particle regimes associated with secondary ice production from -3° to -8°C. Both trends mentioned for all temperatures are observed for both temperature ranges, although they are much more prevalent at temperatures less than

-8°C.
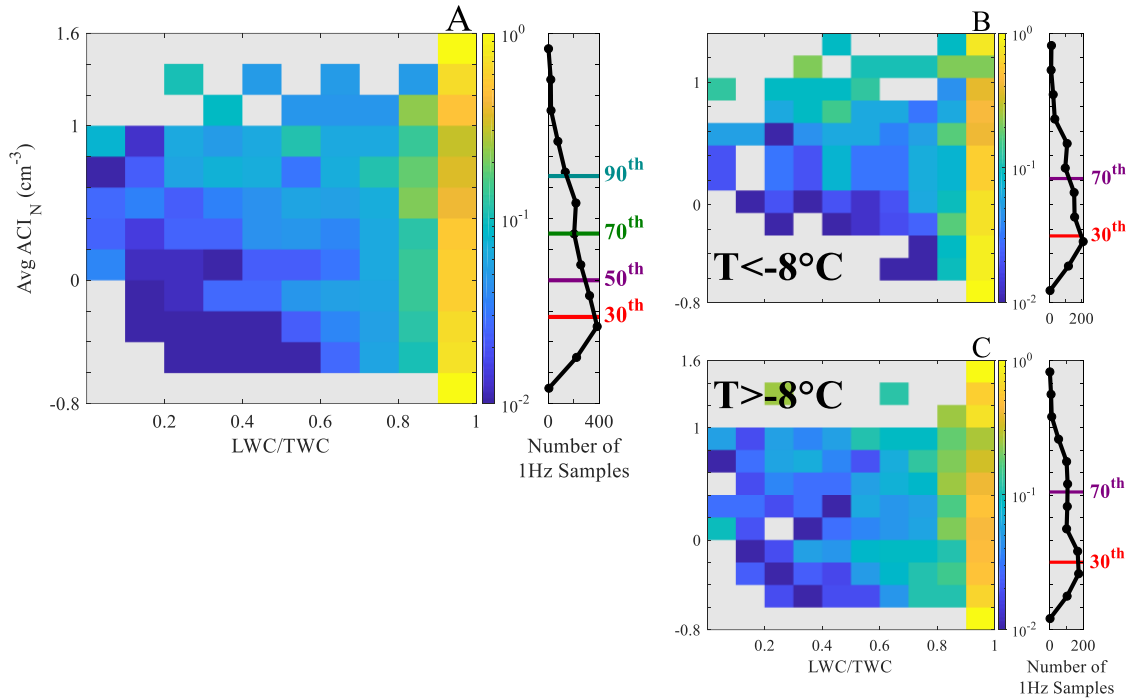
Figure 37: Normalized joint histograms of occurrences relating 1 Hz mixed phase samples of LWC/TWC to transect average ACI_N for all temperatures (A), for temperatures less than -8°C (B) and temperatures warmer than -8°C (C). Results are normalized by average ACI_N bins, where the sum of each row equals one. The number of samples for each average ACI_N bin are shown in the narrow plots immediately to the right of the respective histograms. Percentiles of average ACI_N are shown by the colored horizontal lines.

Namely, the frequency of samples at relatively low LWC/TWC and low average ACI_N is slightly greater at higher temperatures, which may be due to the sufficiency of weaker mixing to induce an enhanced WBF, increased riming or errors associated with misclassification of drizzle (which can appear as aspherical particles) as ice.

To explore how mixed phase PSDs vary depending on the amount of glaciation, PSDs in Figure 38 are calculated for different ranges of LWC/TWC for all average ACI_N (Figure 38A–C) and for the upper 50th percentile of ACI_N (Figure 38D–F). Note that sample sizes are shown in the respective panels, and the difference in sample sizes

109

between the highest and lowest ranges of LWC/TWC decreases with increasing average

ACI_N, consistent with findings in Figure 37. As previously mentioned, the liquid mass is

expected to decrease whereas ice mass is expected to increase as LWC/TWC transitions

from 1 to 0. This is consistent with trends in the average PSDs for all ranges of average

ACI_N, where number distribution functions of particles with D greater than 200 μm are

greatest for LWC/TWC<0.4 and lowest for LWC/TWC>0.9.
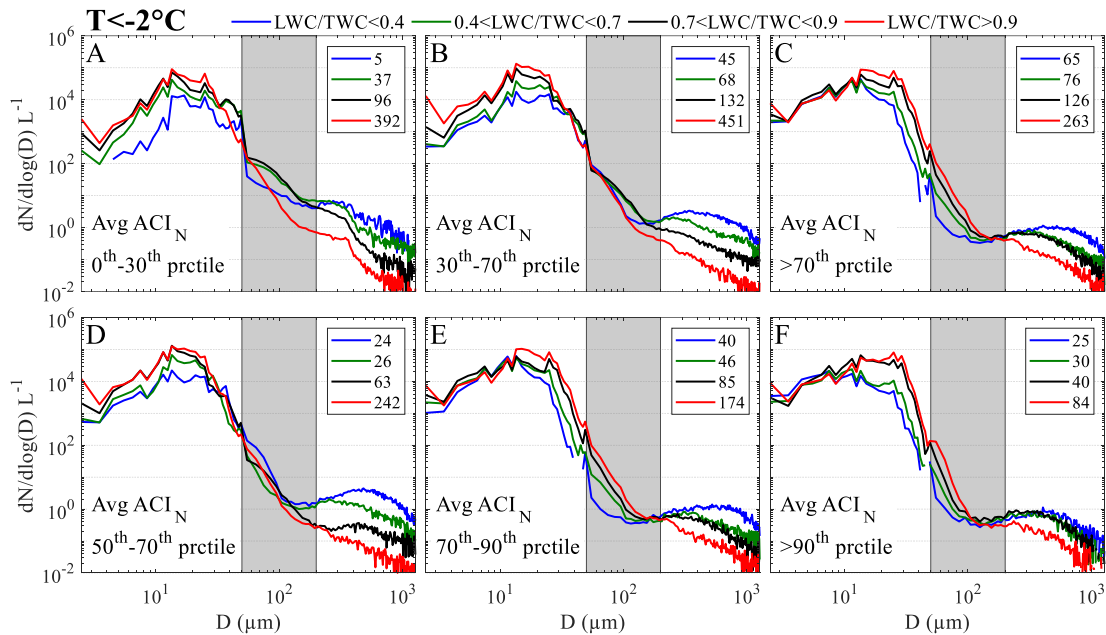
Figure 38: Average mixed phase PSDs shown for percentiles ranging over all mixed phase samples (A–C) and for percentile ranges exceeding the 50th percentile (D–F). Colored lines represent average PSDs for different ranges of LWC/TWC. The number of samples is shown in each respective panel. Results are shown for temperatures less than -2°C.

Number distribution functions of particles with D < 50 μm also decrease with decreasing

LWC/TWC for all average ACI_N. However, number distribution functions for D < 15 μm

decrease more rapidly for the average ACI_N less than the 70th percentile compared to

higher percentiles of the average ACI_N. In fact, these number distribution functions only

vary by 8–30% for different LWC/TWC above the 70th percentile (Figure 38C). The

difference in the number distribution function for D between 30 and 100 μm amongst difference ranges of LWC/TWC increases with increasing average ACI_N, characterized by decreasing number distribution functions for D = 100 μm. These particles are most likely droplets (based off assumptions of CDP sensitivity to spherical particles and from visual examination of 2DS imagery), which are preferentially removed at relatively high average ACI_N.

Results in Figure 38D–F focus on differences in PSDs at relatively high ACI_N, in part to avoid the large set of drizzling samples discussed previously (Figure 34D), which appear as sharp decreases in the number distribution functions at D = 400 μm for average ACI_N less than the 30th percentile (Fig. 38A). This is also done to account for the inability to determine when entrainment-mixing is in fact taking place (similarly discussed in reference to Figure 35). Similar trends of decreasing N(log(D)) at D<10 μm with decreasing LWC/TWC for relatively low average ACI_N, (50th to 70th percentile; Figure 38D) and decreasing number distribution functions at 100 μm with increasing average ACI_N are observed. In addition, the difference in particle sizes from 30–100 μm with decreasing LWC/TWC, which are primarily large drops, is much more apparent at greater average ACI_N, as the colored lines do not overlap and increasingly diverge. This is most notable at average ACI_N greater than the 90th percentile, which also has an order of magnitude difference in drop sizes from 10–30 μm (Figure 38F).

Although the number distribution functions of large ice (D>200 μm) still differ for ranges of LWC/TWC above the 90th percentile of average ACI_N, they are the least variable compared to lower average ACI_N percentiles. This may be due to evaporating drops primarily replenishing the subsaturated air resulting from substantial dry air entrainment, which may also impede ice crystal growth. In contrast, the highest number

distribution functions of large ice occur at low LWC/TWC for average ACI_N between the

50th and 70th percentiles. However, there are fewer samples at low LWC/TWC for lower

average ACI_N compared with higher average ACI_N. This is likely why the highest large

ice concentrations occur at average ACI above the 90th percentile in Figure 35. Namely,

averages at low average ACI_N are heavily weighted by samples having high LWC/TWC.

These findings suggest that at substantially strong mixing, the enhanced WBF process

associated with evaporating drops is partially offset by sufficiently large intrusions of dry

air.

4.6. Results in context of cloud morphology

Results thus far have examined entrainment-mixing regardless of cloud type and

location within the clouds (e.g., cloud top and cloud base). Averaged PSDs in relation to

the normalized cloud height (z_n) are shown in this section and related to the transect

analysis.

Figure 39 shows average PSDs for the liquid (A) and mixed phase (B) samples at

cloud base ($z_n<0.1$), cloud top ($z_n>0.9$) and within the cloud ($0.1<z_n<0.9$). The PSDs shift

towards larger particle sizes with increasing z_n for the liquid phase, consistent with

particle growth via condensation and collision-coalescence of an ascending air parcel.

However, large drop number distribution functions (D>200 μm) are nearly similar

regardless of z_n. In contrast, the highest concentrations of large ice particles in mixed

phase samples are observed at cloud top and are lowest near cloud base. Peak number

distribution functions of large ice crystals also shift to slightly larger sizes (from 300 to

500 μm) with increasing z_n, suggesting large ice particles are preferentially growing at

cloud top. It is important to note that although ACI_N are often greater at cloud top than

cloud base, relatively high ACI_N occur at cloud top *and cloud base* (Figure 29B).
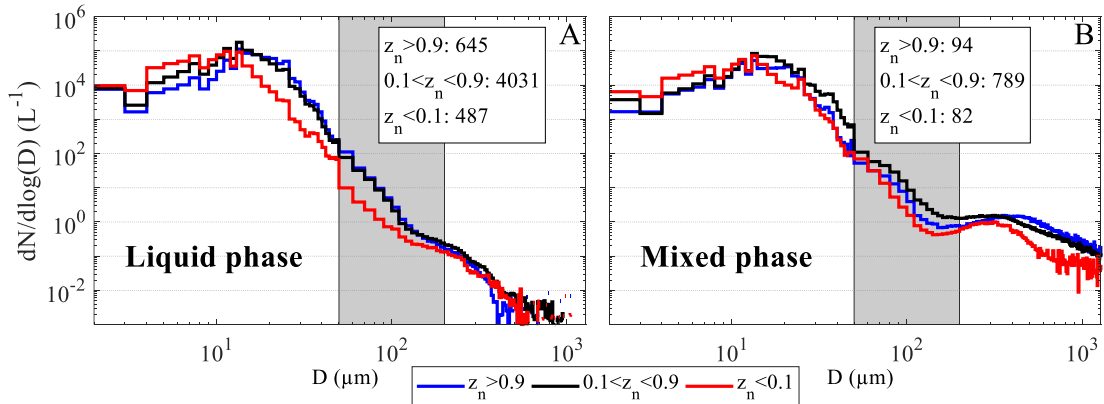
Figure 39: Average PSDs for liquid (A) and mixed (B) phase samples for different ranges of z_n.

Analysis of 1 Hz and average ACI_N are not controlled by normalized cloud height, so results may (perhaps likely) combine samples from both of these regions. Since large ice concentrations are found to be lowest at cloud base (Figure 39B; Figure 40B,C), there is the possibility for an underestimation of entrainment-mixing WBF enhancement. Regardless, these peak sizes from 300–500 µm are similar to those observed with relatively high average ACI_N throughout this study (e.g., Figure 35), highlighting the potential importance of entrainment-mixing on WBF process rates.

Mixed phase results are separated according to the number of cloud layers in Figure 40. PSDs from single-layer clouds are shown in Figure 40A and from multi-layer clouds in Figure 40B. Cloud layer classification follows D'Alessandro et al. (in preparation). Not only have mixed phase occurrence frequencies been found to be much larger in multi-layer clouds (D'Alessandro et al., in preparation), but notable peaks of large ice concentrations from 300–500 µm are primarily observed in multi-layer clouds as well. These peaks are enhanced for middle cloud layers, defined as cloud layers residing between the highest and lowest cloud layers of multi-layer clouds (Figure 40C).
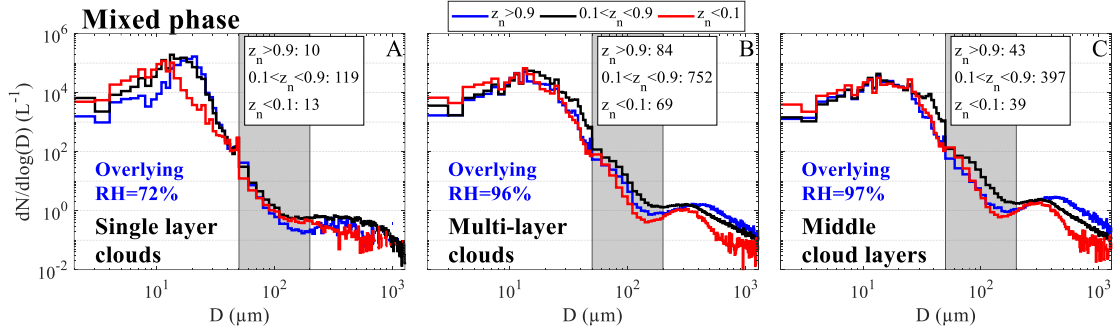
Figure 40: Similar to Figure 39, except results are only shown for mixed phase samples. Results are shown for single-layer clouds (A), multi-layer clouds (B) and middle cloud layers (residing between the highest and lowest cloud layers of multi-layer clouds; C). The blue text is average RH immediately overlying the respective cloud layer types (taken from D'Alessandro et al. (in preparation)).

D'Alessandro et al. (in preparation) shows air immediately overlying these middle layers is nearly saturated, whereas subsaturated conditions are commonly observed overlying single-layer clouds as well as the highest layers of multi-layer clouds (blue text in Figure 40). This suggests the importance of an ample moisture supply towards ice crystal growth in entrainment-mixing events, contrary to simply considering dry air enhancing evaporation and the resulting available vapor content.

4.7. Conclusion

4.7.1. Overview of findings

This study uses in situ observations from SOCRATES to provide a statistical analysis on the impacts of entrainment-mixing upon mixed phase cloud properties over the Southern Ocean. Strong correlations exist between drop clustering and the ratio of actual to adiabatic mass content at cloud tops (-0.62 to -0.74), as well as clustering and mixing length scales (0.53). These and other findings suggest clustering on scales of 100–1000m is primarily related to entrainment-mixing. Because of this, droplet clustering is utilized as a proxy variable for qualitatively determining the degree of entrainment-

mixing. Observations are split into transects, defined as regions of neighboring 1 Hz samples which range from 1.0 to 2.1 km in horizontal sampling distance. The use of transects allows for samples associated with local entrainment-mixing to be analyzed in relation to the background microphysical properties and allows for analysis on spatial scales comparable to horizontal grid spacing in weather and climate models.

Clustering is positively related to ice particle concentrations with maximum dimensions exceeding 200 μm, suggesting entrainment-mixing enhances WBF process rates. Average number distribution functions associated with the highest percentiles of clustering (>70th percentiles) closely resemble those at cloud top of multi-layer clouds, suggesting entrainment-mixing could be a major factor determining ice characteristics at cloud top.

Clustering is examined as a function of LWC/TWC in order to ascertain impacts of mixing on mixed phase evolution, considering that values will transition from 1 to 0 during glaciation. Distributions of LWC/TWC are heavily skewed towards 1 at minimal/non-existent clustering, and transition to more uniform distributions of LWC/TWC with increasing clustering. This trend is more pronounced at temperatures less than -8°C, where the difference in the saturation vapor pressures of liquid and ice is greater than at higher temperatures. Results suggest that a minimal amount of entrainment-mixing may increase the likelihood for mixed phase samples to undergo complete glaciation on spatial scales of ~100m. Average PSDs are similarly examined as functions of LWC/TWC to evaluate mixed phase evolution. Drop number distribution functions between 10–20 μm decrease with decreasing LWC/TWC regardless of weak or prevalent clustering. At relatively low clustering, small drop number distribution

functions (D<10 μm) are found to decrease with decreasing LWC/TWC, which is consistent with glaciating conditions. In contrast, larger drop number distribution functions (D>30 μm) are preferentially reduced with decreasing LWC/TWC when clustering is prevalent. These results suggest different drop size modes are preferentially removed during glaciation depending on the relative strength of entrainment-mixing.

4.7.2. Concluding remarks

The goal of this study was to provide a qualitative assessment of the impact of mixing on mixed phase microphysical properties. Drop clustering has been argued to provide a simple and effective measure to broadly diagnose the strength of entrainment-mixing. In fact, previous studies have attempted to characterize entrainment-mixing and its impacts based on drop size distribution inhomogeneities (Bower & Choularton, 1988; Paluch, 1986; Paluch & Knight, 1984). Although clustering undoubtedly fails to capture the associated complexities and relevant properties of air-mass interactions, analysis here separates mixed phase properties by broad percentile ranges of clustering in order to capture the general strength of mixing and its impacts. Persistent trends (e.g., increasing number distribution functions of large ice with greater average ACI_N) combined with findings consistent with current theoretical understandings of mixing (e.g., downward shifts in average PSDs with increasing ACI_N indicative of inhomogeneous mixing, decreasing number distribution functions of large drops with increasing average ACI_N for liquid phase transects) suggest the results presented here capture the intended mixing-cloud particle interactions.

Previous studies have argued for or against different clustering metrics for reasons such as scale dependence (Baker & Lawson, 2010; Shaw et al., 2002). However, scale

116

invariance is expected to be minimal since number concentrations are normalized by a constant sample volume. In addition, the clustering metric is only in service of diagnosing the magnitude of mixing. The study does not intend to provide an absolute measure of clustering but rather to inform the observational and modeling communities potential pathways for the evolution of mixed phase microphysical properties in the presence of entrainment-mixing.

A few studies have already been introduced that discuss direct relationships of droplet clustering on local microphysical properties (e.g., Castellano et al., 2004; Castellano et al., 2008). However, these effects are determined on much smaller spatial scales than the scale of clustering presented in this study. Regardless of these potential impacts of clustering on microphysical properties, such considerations do not nullify findings relating entrainment-mixing to mixed phase evolution. Rather, mixing likely enhances clustering which effectively impacts the microphysical properties. For example, clustering resulting from dry air insertion may lead to enhanced evaporation of droplets near the edges of drop clusters due to differences in the local vapor density fields within clusters and near cluster edges (Castellano & Ávila, 2011). It may prove helpful to disseminate direct impacts of mixing and clustering on mixed phase properties.

Clustering is calculated on spatial scales orders of magnitude greater (100 m) than those considered in most of the theoretical clustering studies listed here (~1 cm). Commonly deployed in situ instrumentation for most field campaigns, including SOCRATES, are unable to determine clustering at finer spatial scales. Such probes require averaging over relatively long durations to compensate for the instruments' inherent lack of ergodicity. Other probes, such as the Holographic Detector for Clouds (HOLODEC), have the advantage of obtaining size distributions by imaging a constant

volume sample field. Few intercomparisons between these instruments have been performed (e.g., Beals et al., 2015; Glienke et al., 2017; Jackson et al., 2014), and those comparing varying scales of clustering are warranted in order to disseminate primary and secondary causes impacting mixed phase properties.

Future work should aim to constrain mixing properties by directly relating entrainment rates with mixed phase properties at cloud top. Similar work evaluating entrainment-mixing is warranted for different cloud types and regions globally, which will be associated with varying atmospheric phenomenon, turbulent features, and mixed phase properties. Additional work should also explore the impacts of phase inhomogeneity on the potential enhancement of WBF within the length scale of mixed phase observations (~100 m) used here.

5 CONCLUSIONS

Both climate and higher resolution models fail to adequately represent clouds over the Southern Ocean, as they often mischaracterize cloud phase frequencies and bulk microphysical properties. This dissertation uses airborne in situ observations from the SOCRATES field campaign to characterize the frequency and spatial heterogeneity of cloud phase, compare and contrast the microphysical properties of single and multi-layered clouds, and evaluate the impacts of entrainment-mixing on the microphysical properties of mixed phase clouds. Approximately 14 hours of in-cloud data within temperatures where liquid, ice and mixed phase samples can coexist (-40° to 0°C) are available and are used in the analyses, whereas 55 single- and 183 multi-layer cloud profiles are used to compare the different cloud layer types. A combination of in situ instrumentation is used here to determine cloud phase, including a supervised machine learning algorithm applied to a particle imaging cloud probe. The main results are summarized below.

This dissertation reported large amounts of liquid observed in low-level clouds over the Southern Ocean, with ~70% of in-cloud samples classified as liquid at temperatures between -20° and 0°C. The frequency of ice generally increased with decreasing temperature, and sharply increased as temperatures decreased below -20°C. However, the lowest cloud layers of multi-layered clouds had the largest frequency of ice-containing samples (i.e., mixed and ice phase), and the highest layers of multi-layered clouds had the lowest frequency. Further, ice-containing frequencies were found to slightly *decrease* with decreasing temperature from -20° to 0°C within the boundary layer. These results suggest a prominent seeder-feeder mechanism exists over this region,

consistent with previous case studies that observed ice precipitation (e.g., Alexander et al., 2021). Results from this dissertation also highlight the necessity of using airborne, in situ observations to adequately analyze phase frequencies, since relying solely on ground-based or satellite remote sensing data fails to capture trends reported here due to attenuation and other uncertainties (e.g., sun glint due to low solar zenith angle).

The relationship of cloud phase to concentrations of ice nucleating particles (INP) and cloud condensation nuclei (CCN) is also explored in this dissertation, which can give insight into the relevance of primary and secondary ice nucleation mechanisms over the region. Select cases showed significant correlations between INP concentrations and ice-containing frequencies expected of primary ice nucleation. However, many cases where phase frequencies resided within temperatures similar to INP activation temperatures did not have significant correlations. This suggests alternative ice initiation processes (e.g., secondary ice production) are likely prevalent over the region. Due to the dearth of INP over the Southern Ocean, long averaging times were required to get statistically significant samples above background values. This and other limitations introduce uncertainties into the collocation of INP and phase data, which may also account for the weak correlations. Phase frequencies in this dissertation were separately related to INP and CCN above and within the boundary layer. Within the boundary layer, CCN concentrations had no impact on phase frequencies. However, the frequency of liquid was found to be significantly higher in high CCN environments in the free troposphere. Large drop concentrations (diameters > 25 μm) are also negatively correlated with CCN concentrations, suggesting a reduced Hallet-Mossop process (a secondary ice production mechanism requiring large drops) may contribute to higher liquid phase frequencies.

The spatial heterogeneity of cloud phase is analyzed in this dissertation, which is crucial to adequately represent in numerical weather models since previous studies have shown it can drastically impact simulate cloud properties due to varying the rate of the WBF process. The statistical analysis performed here extends previous studies that qualitatively evaluated spatial heterogeneity for select cases. The first quantitative measure of spatial heterogeneity is introduced here and referred to as a spatial heterogeneity score (SHS). The mixed (liquid) phase is found to be the most (least) spatially heterogeneous phase between -20° and 0°C. Additionally, utilizing SHS allows for directly relating measured parameters to the degree of spatial heterogeneity. Two parameters found to be directly related to spatial heterogeneity are vertical air motion and ice crystal size. Vertical velocity distributions are centered at 0 m s^{-1} and broaden with increasing heterogeneity, suggesting phase heterogeneity can be parameterized as a function of turbulent motion (e.g., turbulent kinetic energy). Ice crystal sizes in ice and mixed phase samples are smaller in regions of greater spatial heterogeneity, suggesting greater heterogeneity may be associated with the earlier stages of cloud lifetimes. This finding may also be due to dry air mixing within spatially heterogeneous regions, which could inhibit ice particle growth.

The bulk microphysical properties of single- and multi-layer clouds are evaluated and contrasted in this dissertation. Single-layer clouds have greater liquid drop concentrations than multi-layer clouds. However, the highest drop concentrations were associated with single-layer clouds from the only two research flights which sampled clouds in coupled environments. Drop concentrations in coupled environments are approximately double of those in decoupled environments. But, even when comparing

single- and multi-layered clouds in decoupled environments, single-layer clouds generally have higher drop concentrations. Both liquid drop size distributions and total particle size distributions (i.e., including ice particles in mixed and ice phase samples) are broader in non-top cloud layers (i.e., multi-layer clouds underlying the highest layer), compared with top cloud layers (i.e., single-layer and the highest layer of multi-layer clouds). The differences in microphysical properties between single- and multi-layer clouds are observed regardless of whether they reside within or above the boundary layer.

Findings from this dissertation reveal drop clustering is slightly greater at cloud top for top cloud layers, which is likely related to greater cloud top cooling rates which are also observed for top layers. A distinct difference in relative humidity immediately above cloud top is also observed between top and non-top layers. Namely, above-cloud relative humidity is ~70% for top cloud layers (~60% for single-layer clouds) whereas conditions are nearly saturated above-cloud for non-top layers. Despite differences in the cloud top and aforementioned properties between single- and multi-layer clouds, both cloud types have relatively high concentrations of drizzle size drops (drops with maximum dimensions exceeding 50 μm having average number concentrations ranging from 30–50 L^{-1}), revealing both cloud types have a propensity for precipitating.

The impacts of entrainment-mixing on mixed phase cloud properties are analyzed in this dissertation by taking advantage of strong, positive relationships between droplet clustering and entrainment-mixing. These relationships are observed when relating a clustering metric (altered clustering index; ACI) to the ratio of the actual cloud mass to adiabatically derived mass at cloud top (i.e., drop clustering increases as the ratio approaches zero). Additionally, drop concentrations and clustering in cloud transects (sets

of neighboring cloud samples ~1.2 km in length) are found to negatively covary, and covary more significantly as the values of the 80th and 20th drop concentration percentiles within individual transects diverge. The transect average clustering also increases as the values of the 80th and 20th drop concentration percentiles diverge, and the average drop size decreases with greater divergence in the drop concentrations percentiles. These findings are consistent with entrainment-mixing locally decreasing drop concentrations (and average drop size) within the cloud transects, which is directly related to the transect average clustering.

Some of the benefits of utilizing clustering as a proxy variable to diagnose entrainment-mixing strength are listed here. First, there is no prior established method for deriving the mixing length scale from in situ observations since the length scale varies depending on the location and spatial scale of the measurement for a given clear-air eddy. Previous studies have derived the length scale based off the clear-sky fraction within a cloud sample. This yields an exceedingly low sample size since most in-cloud measurements in stratified clouds have a clear-sky fraction of zero. The fact that clustering is directly related to (locally) low drop concentrations suggests drop clustering can act as a "looser clear-sky restriction" towards diagnosing entrainment, where a given entrainment event does not completely evaporate a partial cloud area. Additionally, the uncertainty associated with varying spatial scales is not captured when explicitly calculating mixing length scales and the associated turbulent mixing times. However, the use of 1 Hz clustering values in conjunction with the transect average clustering essentially captures scales on the order of 100 m and 1km, respectively.

Mixed phase size distributions are controlled by 1 Hz and transect average

clustering. Results here reveal greater large ice concentrations (maximum dimensions exceed ~300 μm) with increasing clustering. This suggests entrainment-mixing can enhance ice crystal growth via an enhanced WBF process, whereby the local evaporation of drops is enhanced and the associated water vapor contributes to ice crystal growth. Greater clustering is also found here to be directly related with increasing frequencies of mixed phase samples having low liquid to total water content ratios (LWC/TWC), suggesting entrainment-mixing is directly related to increasing glaciation rates (since LWC/TWC is expected to decrease during glaciation). However, mixed phase samples with the greatest large ice concentrations occur in regions with moderate clustering at low LWC/TWC. This suggests sufficiently large degrees of entrainment-mixing may impede the enhanced WBF process and partially offset the enhanced ice crystal growth.

Findings from this dissertation should ultimately be used to improve cloud microphysics parameterizations in both climate and higher resolution models, which will likely reduce biases in the radiative profiles over the Southern Ocean as discussed in Chapters 1–3. Low resolution models should avoid assumptions of homogeneous distributions of liquid and ice particles in mixed phase grid points, which have been shown to result in unrealistic glaciation rates (Tan & Storelvmo, 2016). Parameterizing phase heterogeneity by turbulence parameter(s) will likely improve simulated cloud properties and lifetimes over the region. Modelers should also evaluate the microphysical properties of varying simulated cloud layer types. Results show distinct differences in the properties of different cloud layer types and suggest a high prevalence of varying ice initiation/growth processes, some of which are notoriously difficult to simulate (e.g., secondary ice production). Differences in the layer properties may also aid in the

understanding of multi-layer cloud formation, which is still uncertain. Modelers should also evaluate whether models capture enhanced glaciation rates and under what conditions (or whether) an enhanced WBF process occurs given the presence of entrainment-mixing. Results here characterize the entrainment-mixing strength by the degree of droplet clustering, rather than explicitly solving for entrainment rates or turbulent mixing times. Because of this, modelers should simply evaluate the varying pathways associated with mixed phase evolution in the presence of entrainment-mixing shown here. Namely, that (1) glaciation is enhanced in the presence of entrainment-mixing, (2) increases in large ice crystal concentrations (i.e., enhanced WBF process) can occur in the presence of entrainment-mixing and (3) the enhanced WBF process can be offset by sufficiently high degrees of entrainment-mixing.

Finally, many of the analyses presented here should be replicated for varying regions and cloud regime types, particularly for varying regions over the Southern Ocean as well as the Arctic, in order to evaluate the representative ess of the results. For example, the SOCRATES domain was selected due to its representativeness of the pristine conditions commonly observed over more remote regions of the Southern Ocean. However, D'Alessandro et al. (2019) found significantly lower liquid phase frequencies over the Southern Ocean in the Drake passage compared with the phase frequencies south of Tasmania presented here, likely due to differences in aerosol source regions from nearby land masses. Analyzing the phase spatial heterogeneity and impacts of entrainment-mixing on mixed phase clouds may also be of particular interest for varying geographic regions and cloud regimes not evaluated here (e.g., wave clouds, deep convective clouds, etc.), as well as on varying spatial scales (e.g., < 100 m).

6 APPENDIX A – Supplementary material

The turbulent dissipation is taken from Paluch & Baumgardner (1989) and shown as:

$$\varepsilon = \frac{D_{NN}^{\frac{3}{2}}}{(4.01b)^{\frac{3}{2}} l_e} \tag{A1}$$

Where $b \approx 0.2(2\pi)^{2/3}$ (taken from Panofsky & Dutton (1984)), l_e is the length scale and D_{NN} is taken from Meischner et al. (2001) and shown as:

$$D_{NN}(t, TAS) = \frac{1}{3} \left\{ \begin{array}{c} \frac{8}{7}\left[u(t) - u\left(t - \frac{l_e}{TAS}\right)\right]^2 + \frac{8}{7}\left[v(t) - v\left(t - \frac{l_e}{TAS}\right)\right]^2 + \\ \left[w(t) - w(t - \frac{l_e}{TAS})\right]^2 \end{array} \right\} \tag{A2}$$

and additional terms are defined in Appendix C. The phase relaxation times used to determine Da are taken from Pinsky et al. (2018), although the phase relaxation time for the liquid phase has been introduced in earlier studies (Korolev & Mazin, 2003; Pinsky et al., 2015) and is expressed as:

$$\tau_{phase,w} = \left(\frac{4\pi\rho_w A_2}{\rho_a F_w} N_w \overline{r_w}\right)^{-1} \tag{A3}$$

where A_2 is expressed as:

$$A_2 = \frac{1}{q_v} + \frac{L_w^2}{c_p R_v T^2} \tag{A4}$$

and F_w is expressed as:

$$F_w = \frac{\rho_w L_w^2}{K R_v T^2} + \frac{\rho_w R_v T}{e_w D_e} \tag{A5}$$

and additional terms are defined in Appendix C. To derive the phase relaxation time for the mixed phase, the phase relaxation time for the ice is used (Korolev & Mazin, 2003; Pinsky et al., 2015) and expressed as:

$$\tau_{phase,i} = \left(\frac{4\pi\rho_i A_3 \varphi}{\rho_i F_i} N_i \overline{r_i}\right)^{-1} \tag{A6}$$

where A_3 is expressed as:

$$A_3 = \frac{1}{q_v} + \frac{L_w L_i}{c_p R_v T^2} \qquad\qquad \text{A7)}$$

and F_i is expressed as:

$$F_i = \frac{\rho_i L_i^2}{K R_v T^2} + \frac{\rho_i R_v T}{e_i D_e} \qquad\qquad \text{A8)}$$

and additional terms are defined in Appendix C. The phase relaxation times of the liquid and ice phase are combined to determine the relaxation time for the mixed phase (Pinsky et al., 2018) and is expressed as:

$$\tau_{phase,m} = \frac{\tau_{phase,w} \tau_{phase,i}}{(\tau_{phase,w} + \tau_{phase,i})} \qquad\qquad \text{A9}$$

The shorter microphysical response time between the phase relaxation and evaporation times is selected when determine L*. The evaporation time for the liquid is taken from Rogers & Yau (1996) and is expressed as:

$$\tau_{evap} = -\frac{r_m^2}{2As} \qquad\qquad \text{A10)}$$

Where A is expressed as:

$$A = \frac{1}{\left[\left(\frac{L_w}{R_v T} - 1\right)\frac{L_w \rho_w}{KT} + \frac{\rho_w R_v T}{D_e e_w}\right]} \qquad\qquad \text{A11)}$$

The evaporation time for the mixed phase is defined as the time for complete glaciation to occur within a mixed phase cloud (Hoffmann, 2020), which is expressed as:

$$\tau_{gl} = \frac{3}{2}\tau_{phase,i}\frac{q_l}{(q_{s,l} - q_{s,i})} \qquad\qquad \text{A12)}$$

and additional terms are defined in Appendix C.

7 APPENDIX B – Supplementary figures
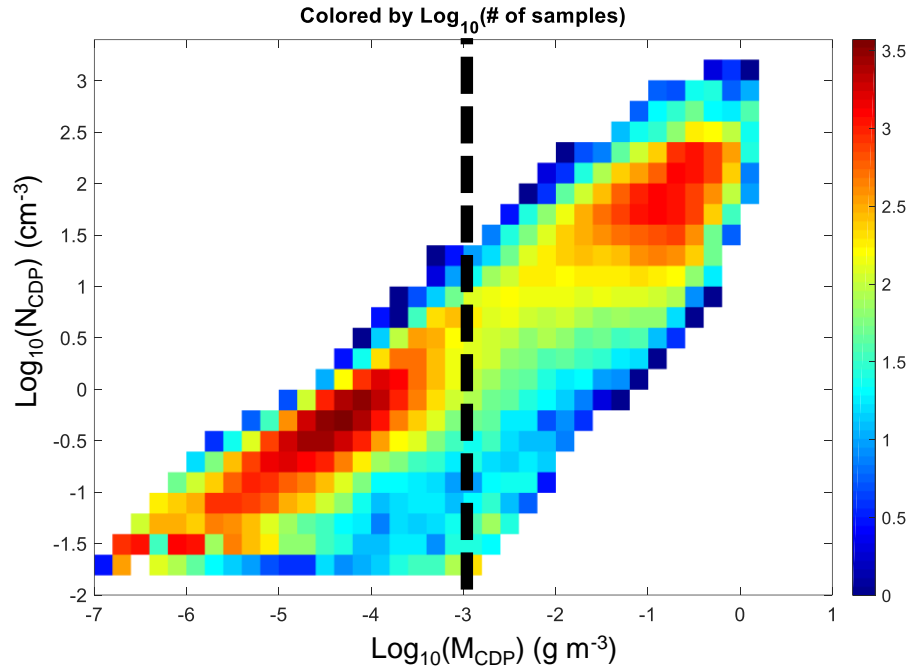
Figure A: Joint frequency distribution of M_{CDP} and N_{CDP}. The dashed line shows the M_{CDP} threshold as defined in Section 1.2.2.
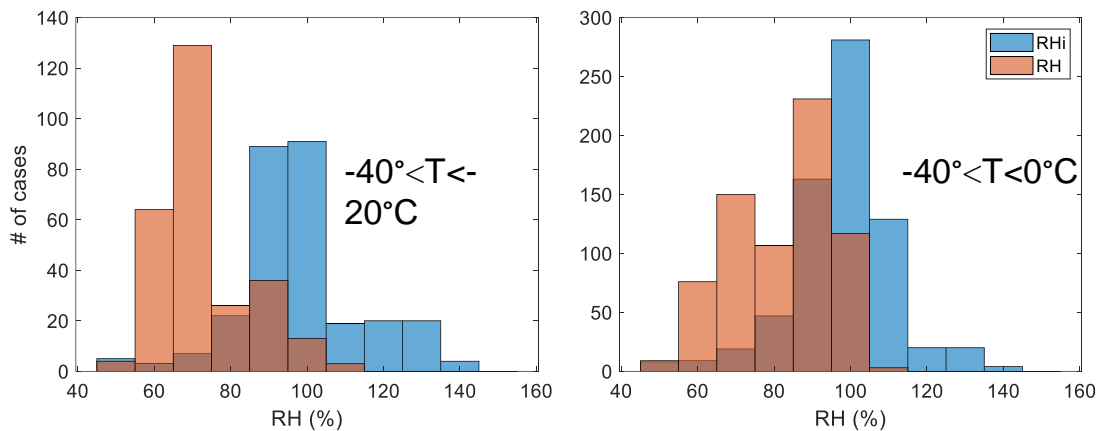
Figure B: Histograms of relative humidity with respect to ice (RHi) and relative humidity with respect to liquid (RH) of the 751 cases changed as discussed in Section 1.2.2 at temperatures less than -20°C (left panel; 289 cases) and at all temperatures (right panel).
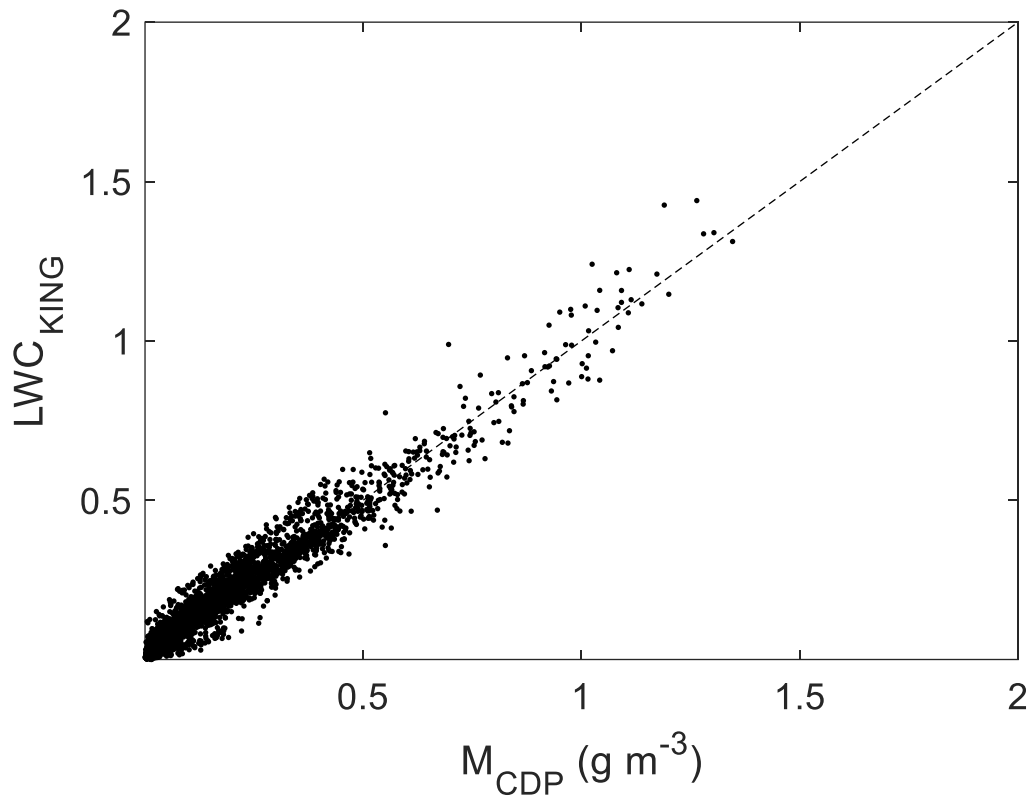
Figure C: Scatter plot of M_{CDP} and LWC_{KING} for mixed phase samples where $N_{CDP} > 5$ cm^{-3}.
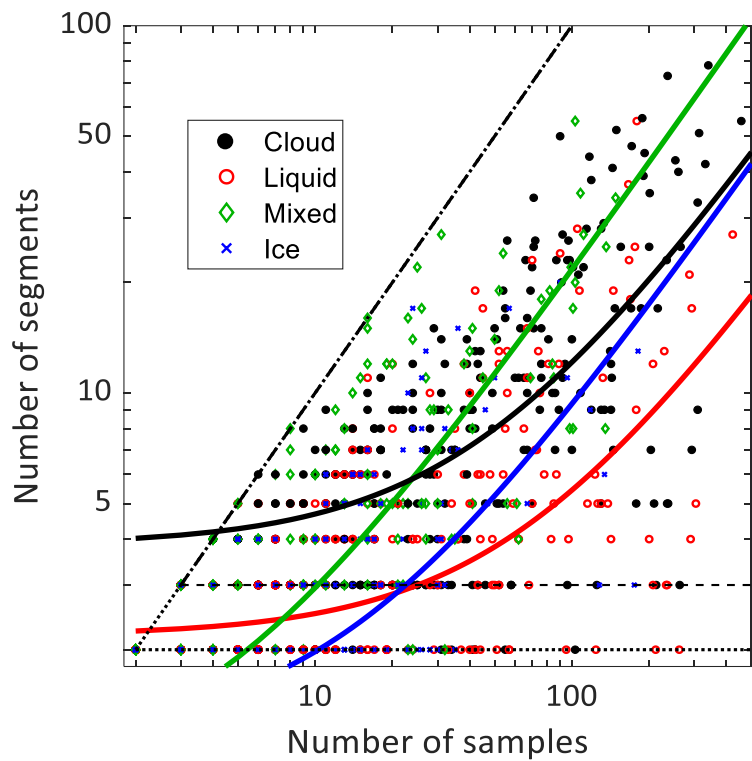
Figure D: Similar to Figure 8C,D except for temperatures from -20° to 0°C.
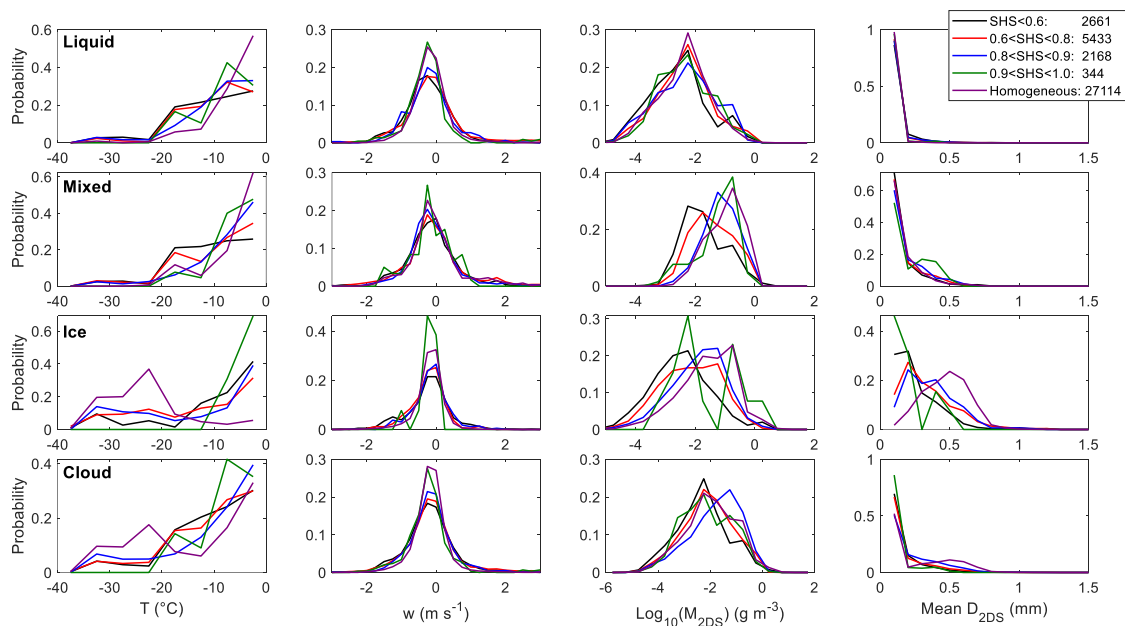
Figure E1: Similar to Figure 11, except subtransects (as defined in the text) are set as lengths of 10 samples.
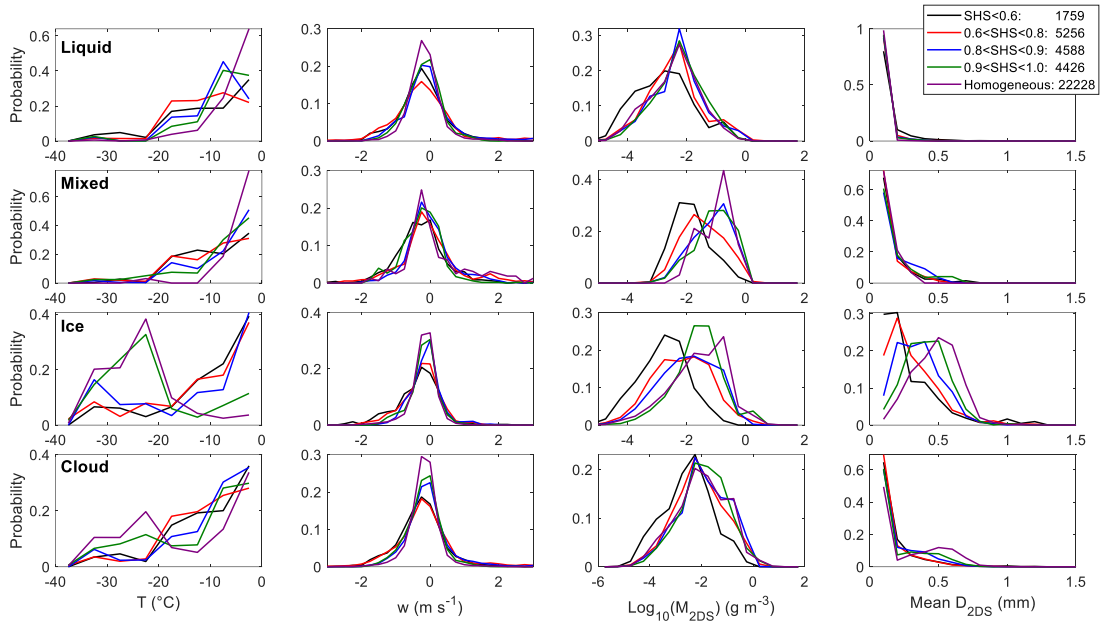
Figure E2: Similar to Figure 11, except subtransects (as defined in the text) are set as lengths of 30 samples.
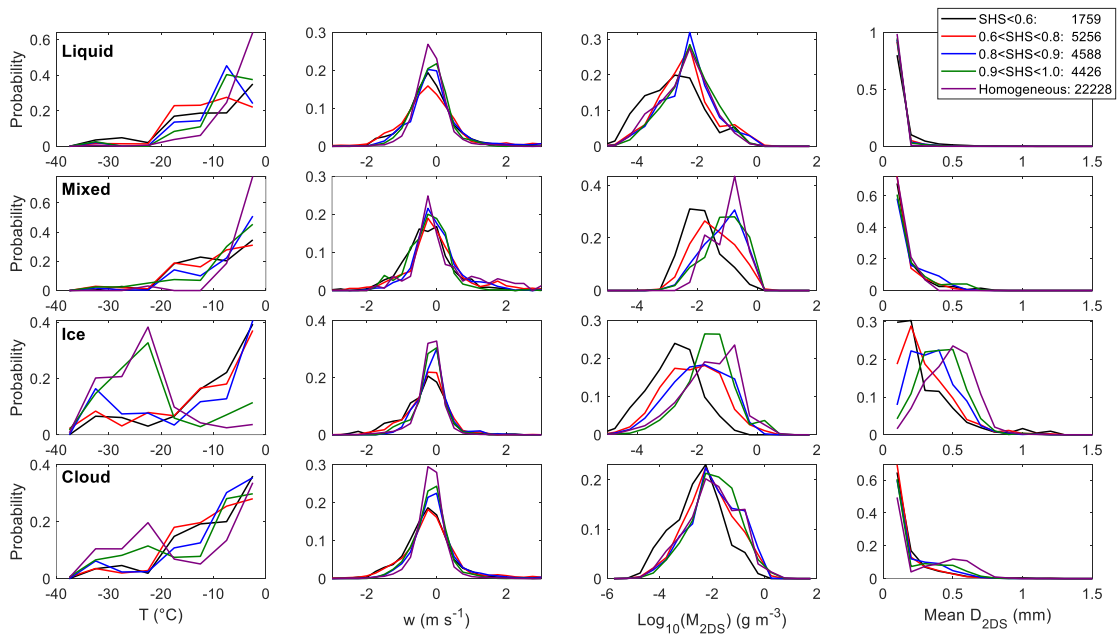
Figure E3: Similar to Figure 11, except subtransects (as defined in the text) are set as lengths of 40 samples.
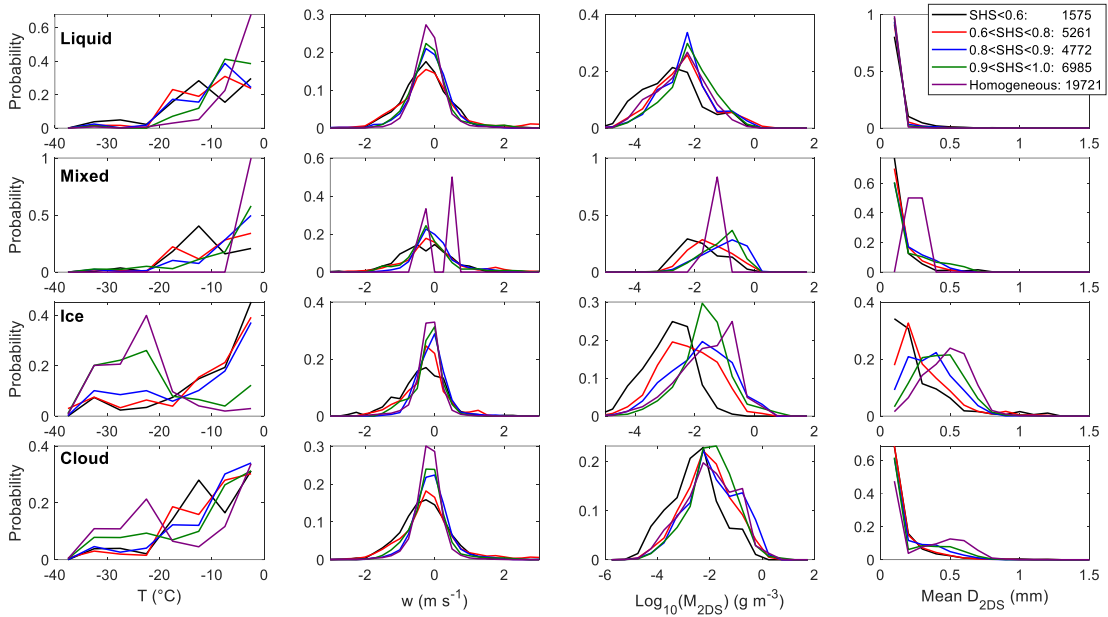
Figure E4: Similar to Figure 11, except subtransects (as defined in the text) are set as lengths of 50 samples.
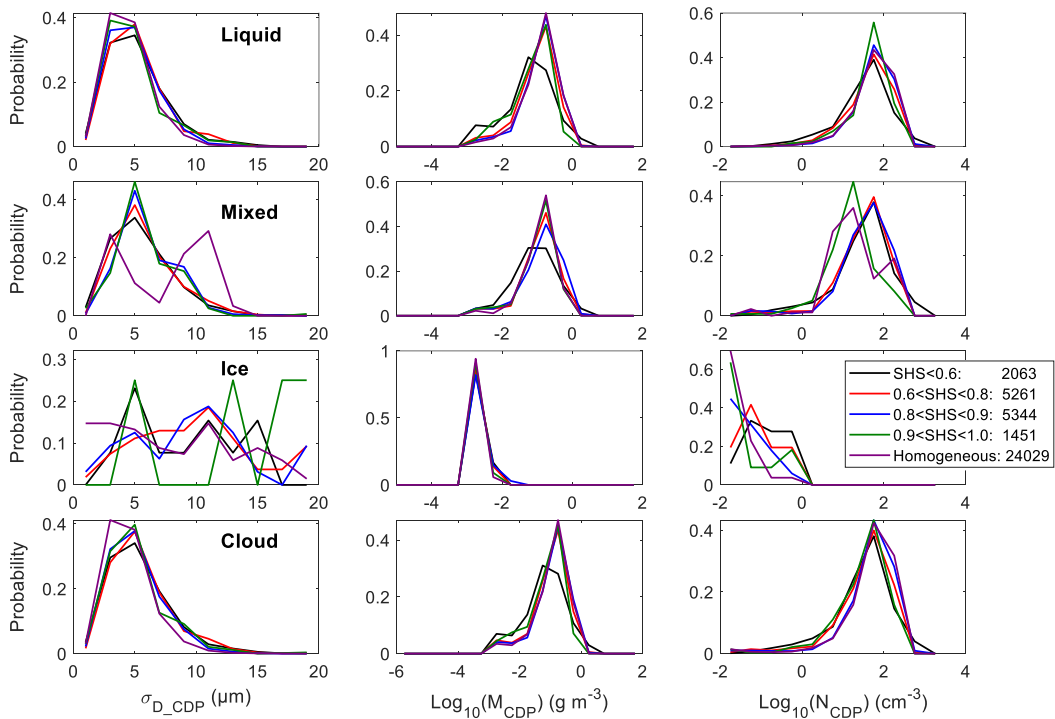
Figure F: Similar to Figure 11, showing σ_{D_CDP} (left column), M_{CDP} (middle column) and N_{CDP} (right column).
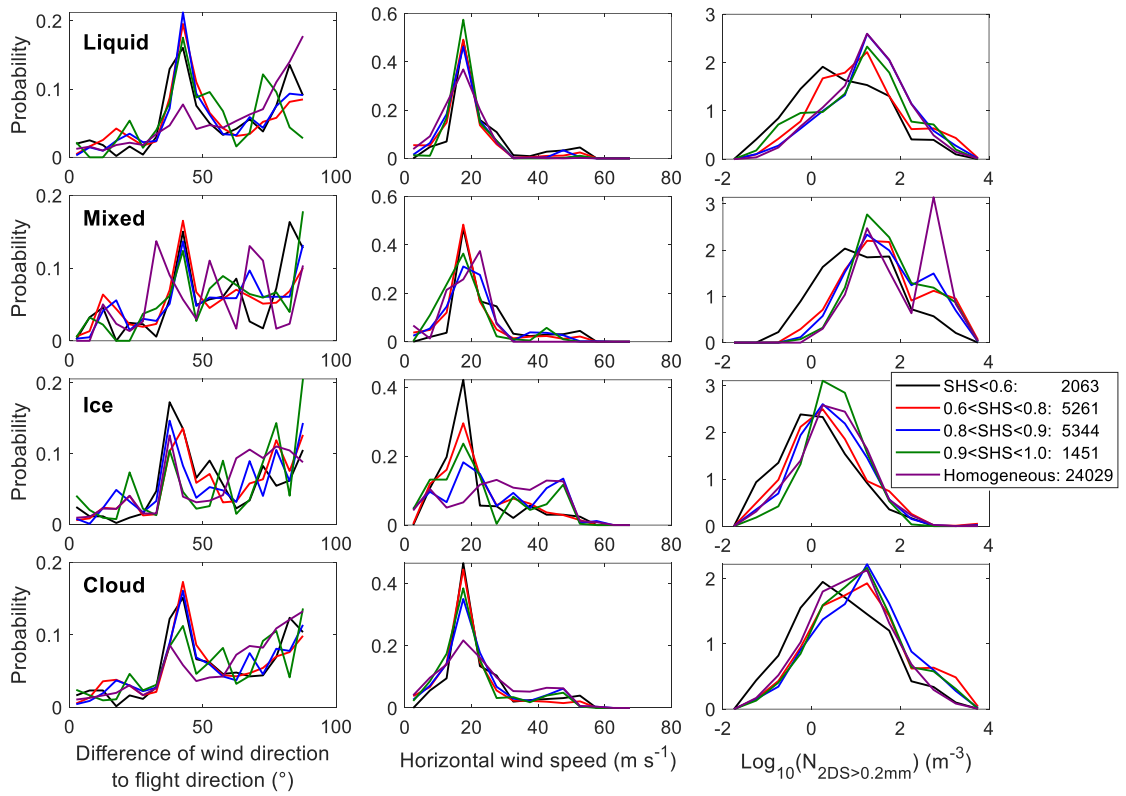
Figure G: Similar to Figure 11, except for the difference between wind direction and flight direction (left column), horizontal wind speed (middle column) and N_{2DS} (right column). The difference between wind direction and flight direction is set to have a range of 0° to 90°, where an absolute directional difference of 180° would be set to 0° and an absolute difference of 100° would be set to 80°, etc.
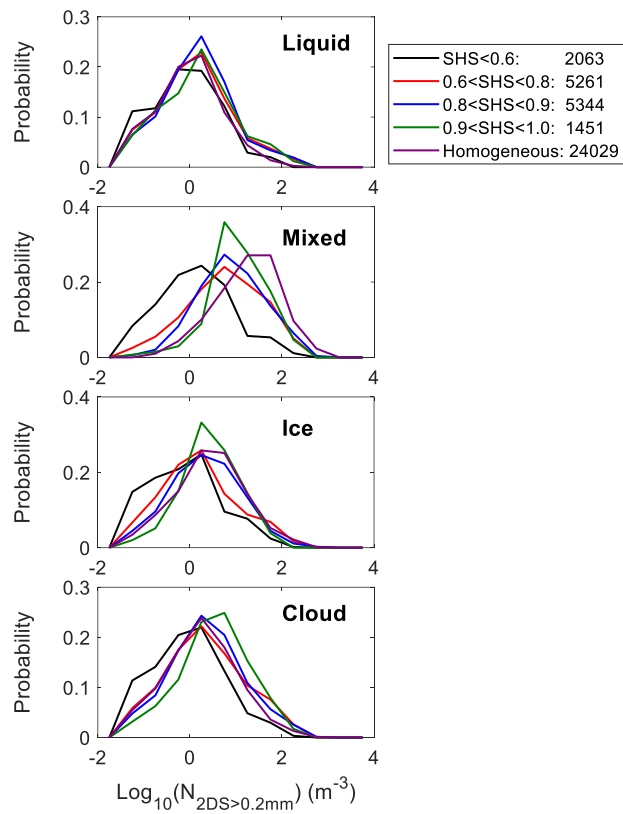
Figure H: Similar to Figure 11, except for N_{2DS} where particles have D>200 μm (N_{2DS}>0.2mm)
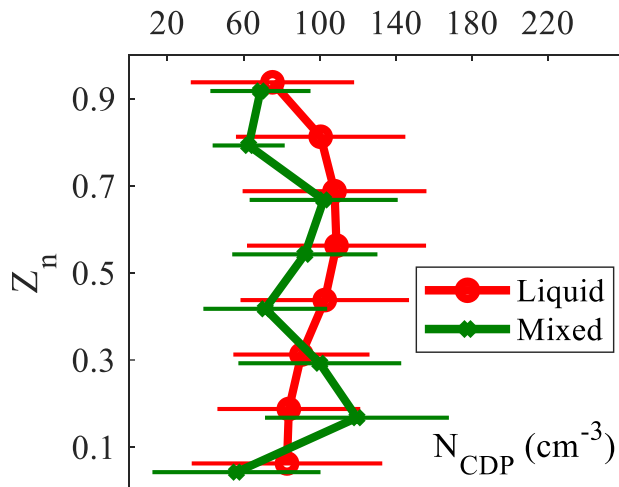
Figure I: Vertical profile of average N_{CDP} similar to Figure 25–27, except shown for the highest cloud layer of multi-layer clouds.
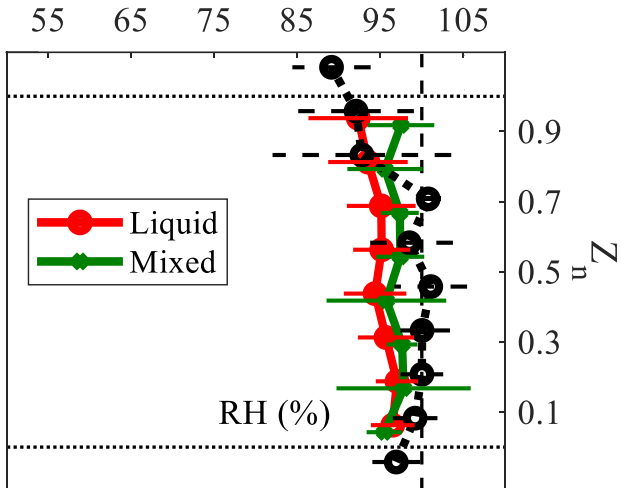
Figure J: Vertical profile of average RH similar to Figure 25–27 , except shown for the highest cloud layer of multi-layer clouds.

APPENDIX C – List of relevant terms

Symbol	Description
2DS	Two-Dimension Stereo Probe
ACI	Altered Clustering Index
AVAPC	Altered Volume Average Pair Correlation
CCN	Cloud condensation nuclei
CDP	Cloud Droplet Probe
CI	Clustering Index
D	Maximum particle dimension
Da	Damköhler number
D_e	Coefficient of diffusion of water vapor in air
e_i	Saturation vapor pressure for ice
e_w	Saturation vapor pressure for liquid water
F	Clear sky fraction
F_{solar}	Incoming solar irradiance
F_{terr_net}	Net terrestrial irradiance
f	Sampling frequency
INP	Ice nucleating particle
K	Coefficient of thermal conductivity of air
L	Mixing length scale
L_i	Latent heat of sublimation
L_w	Latent heat of vaporization
L*	Transition length scale
LWC	Liquid water content
l_e	Length scale
M	Mass content
Mean D	Number weighted mean diameter
MVD	Volume weighted mean diameter
N	Number concentration
N_i	Ice number concentration
N_w	Liquid number concentrations
q_l	Liquid water mixing ratio
$q_{s,i}$	Ice saturation vapor mixing ratio
$q_{s,l}$	Liquid water saturation vapor mixing ratio
q_v	Water vapor mixing ratio
RH	Relative humidity
RICE	Rosemount Icing Detector
R_v	Gas constant for water vapor
r_i	Ice particle radius
r_w	Liquid particle radius
r_m	Number weighted mean radius
r_v	Volume weighted mean radius
s	Supersaturation

SHS	Spatial heterogeneity score
t	Time
T	Air temperature
TAS	True air speed
TWC	Total condensed water content
u	East wind component
v	North wind component
VAPC	Volume Average Pair Correlation
VCSEL	Vertical cavity surface emitting laser hygrometer
w	Vertical air motion
z	Altitude
z_{cloud_top}	Cloud top altitude
z_{cloud_base}	Cloud base altitude
z_n	Normalized height
ε	Turbulent dissipation rate
τ_{evap}	Evaporation time
τ_{gl}	Time for glaciation of mixed phase cloud
τ_m	Turbulent mixing time
$\tau_{phase,i}$	Ice phase relaxation time
$\tau_{phase,w}$	Liquid phase relaxation time
$\tau_{phase,m}$	Mixed phase relaxation time
τ_{phase}	Phase relaxation time
τ_r	Microphysics response time
τ_{react}	Reaction time
ρ_a	Density of air
ρ_i	Density of ice
ρ_w	Density of liquid water
φ	e_w/e_i

8 REFERENCES

Ahn, E., Huang, Y., Chubb, T. H., Baumgardner, D., Isaac, P., de Hoog, M., et al. (2017).
In situ observations of wintertime low-altitude clouds over the Southern Ocean.
Quarterly Journal of the Royal Meteorological Society, *143*(704), 1381–1394.
https://doi.org/10.1002/qj.3011

Ahn, E., Huang, Y., Siems, S. T., & Manton, M. J. (2018). A Comparison of Cloud
Microphysical Properties Derived From MODIS and CALIPSO With In Situ
Measurements Over the Wintertime Southern Ocean. *Journal of Geophysical
Research: Atmospheres*, *123*(19), 11,120-11,140.
https://doi.org/10.1029/2018JD028535

Alexander, S. P., & Protat, A. (2018). Cloud Properties Observed From the Surface and
by Satellite at the Northern Edge of the Southern Ocean. *Journal of Geophysical
Research: Atmospheres*, *123*(1), 443–456. https://doi.org/10.1002/2017JD026552

Alexander, S. P., McFarquhar, G. M., Marchand, R., Protat, A., Vignon, É., Mace, G. G.,
& Klekociuk, A. R. (2021). Mixed-Phase Clouds and Precipitation in Southern
Ocean Cyclones and Cloud Systems Observed Poleward of 64°S by Ship-Based
Cloud Radar and Lidar. *Journal of Geophysical Research: Atmospheres*, *126*(8),
e2020JD033626. https://doi.org/10.1029/2020JD033626

Andrejczuk, M., Grabowski, W. W., Malinowski, S. P., & Smolarkiewicz, P. K. (2009).
Numerical simulation of cloud-clear air interfacial mixing: Homogeneous versus
inhomogeneous mixing. *Journal of the Atmospheric Sciences*. American
Meteorological Society. https://doi.org/10.1175/2009JAS2956.1

Atlas, R. L., Bretherton, C. S., Blossey, P. N., Gettelman, A., Bardeen, C., Lin, P., &

Ming, Y. (2020). How Well Do Large-Eddy Simulations and Global Climate

Models Represent Observed Boundary Layer Structures and Low Clouds Over the

Summertime Southern Ocean? *Journal of Advances in Modeling Earth Systems*,

12(11), e2020MS002205. https://doi.org/10.1029/2020MS002205

Baker, B., & Lawson, R. P. (2010). Analysis of tools used to quantify droplet clustering

in clouds. *Journal of the Atmospheric Sciences*, *67*(10), 3355–3367.

https://doi.org/10.1175/2010JAS3409.1

Baker, B. A. (1992). Turbulent entrainment and mixing in clouds: a new observational

approach. *Journal of the Atmospheric Sciences*, *49*(5), 387–404.

https://doi.org/10.1175/1520-0469(1992)049<0387:TEAMIC>2.0.CO;2

Baker, M. B., Corbin, R. G., & Latham, J. (1980). The influence of entrainment on the

evolution of cloud droplet spectra: I. A model of inhomogeneous mixing. *Quarterly

Journal of the Royal Meteorological Society*, *106*(449), 581–598.

https://doi.org/10.1002/qj.49710644914

Bates, T. S., Huebert, B. J., Gras, J. L., Griffiths, F. B., & Durkee, P. A. (1998).

International Global Atmospheric Chemistry (IGAC) Project's First Aerosol

Characterization Experiment (ACE 1): Overview. *Journal of Geophysical Research:

Atmospheres*, *103*(D13), 16297–16318. https://doi.org/10.1029/97JD03741

Baumgardner, D., Abel, S. J., Axisa, D., Cotton, R., Crosier, J., Field, P., et al. (2017).

Cloud Ice Properties: In Situ Measurement Challenges. *Meteorological

Monographs*, *58*(1), 9.1-9.23. https://doi.org/10.1175/amsmonographs-d-16-0011.1

Baumgardner, Darrel, & Korolev, A. (1997). Airspeed corrections for optical array probe

sample volumes. *Journal of Atmospheric and Oceanic Technology*, *14*(5), 1224–

1229. https://doi.org/10.1175/1520-0426(1997)014<1224:ACFOAP>2.0.CO;2

Beals, M. J., Fugal, J. P., Shaw, R. A., Lu, J., Spuler, S. M., & Stith, J. L. (2015).
Holographic measurements of inhomogeneous cloud mixing at the centimeter scale.
Science, *350*(6256), 87–90. https://doi.org/10.1126/science.aab0751

Bergeron, T. (1928). Über die dreidimensional verknüpfende Wetteranalyse. *Geophys.
Norv.*, *5*(6), 1–111.

Bergeron, T. (1935). On the physics of clouds and precipitation. *Proces Verbaux de
l'Association de Météorologie, International Union of Geodesy and Geophysics*,
156–178.

Bishop, C. (2006). Pattern Recognition and Machine Learning. *New York: Springer*.

Biter, C. J., Dye, J. E., Huffman, D., & King, W. D. (1987). The Drop-Size Response of
the CSIRO Liquid Water Probe. *Journal of Atmospheric and Oceanic Technology*,
4(3), 359–367. https://doi.org/10.1175/1520-
0426(1987)004<0359:TDSROT>2.0.CO;2

Bodas-Salcedo, A., Williams, K. D., Ringer, M. A., Beau, I., Cole, J. N. S., Dufresne, J.-
L., et al. (2014). Origins of the Solar Radiation Biases over the Southern Ocean in
CFMIP2 Models*. *Journal of Climate*, *27*(1), 41–56. https://doi.org/10.1175/JCLI-
D-13-00169.1

Bodas-Salcedo, A., Hill, P. G., Furtado, K., Williams, K. D., Field, P. R., Manners, J. C.,
et al. (2016). Large Contribution of Supercooled Liquid Clouds to the Solar
Radiation Budget of the Southern Ocean. *Journal of Climate*, *29*(11), 4213–4228.
https://doi.org/10.1175/JCLI-D-15-0564.1

Boers, R., Jensen, J. B., Krummel, P. B., & Gerber, H. (1996). Microphysical and short-

wave radiative structure of wintertime stratocumulus clouds over the Southern Ocean. *Quarterly Journal of the Royal Meteorological Society*, *122*(534), 1307–1339. https://doi.org/10.1002/qj.49712253405

Boers, R., Jensen, J. B., & Krummel, P. B. (1998). Microphysical and short-wave radiative structure of stratocumulus clouds over the Southern Ocean: Summer results and seasonal differences. *Quarterly Journal of the Royal Meteorological Society*, *124*(545), 151–168. https://doi.org/10.1002/qj.49712454507

Bower, K. N., & Choularton, T. W. (1988). The effects of entrainment on the growth of droplets in continental cumulus clouds. *Quarterly Journal of the Royal Meteorological Society*, *114*(484), 1411–1434. https://doi.org/10.1002/qj.49711448404

Burnet, F., & Brenguier, J. L. (2007). Observational study of the entrainment-mixing process in warm convective clouds. *Journal of the Atmospheric Sciences*, *64*(6), 1995–2011. https://doi.org/10.1175/JAS3928.1

Castellano, N. E., Avila, E. E., & Saunders, C. P. R. (2004). Theoretical model of the Bergeron-Findeisen mechanism of ice crystal growth in clouds. *Atmospheric Environment*, *38*(39), 6751–6761. https://doi.org/10.1016/j.atmosenv.2004.09.003

Castellano, Nesvit E., & Ávila, E. E. (2011). Vapour density field of a population of cloud droplets. *Journal of Atmospheric and Solar-Terrestrial Physics*, *73*(16), 2423–2428. https://doi.org/10.1016/j.jastp.2011.08.013

Castellano, Nesvit E., Ávila, E. E., & Saunders, C. P. R. (2008). Vapour density field of mixed-phase clouds. *Atmospheric Research*, *88*(1), 56–65. https://doi.org/10.1016/j.atmosres.2007.10.002

Ceppi, P., Zelinka, M. D., & Hartmann, D. L. (2014). The response of the Southern

    Hemispheric eddy-driven jet to future changes in shortwave radiation in CMIP5.

    Geophysical Research Letters, *41*(9), 3244–3250.

    https://doi.org/10.1002/2014GL060043

Cesana, G., & Chepfer, H. (2013). Evaluation of the cloud thermodynamic phase in a

    climate model using CALIPSO-GOCCP. *Journal of Geophysical Research:*

    Atmospheres, *118*(14), 7922–7937. https://doi.org/10.1002/jgrd.50376

Chaumat, L., & Brenguier, J. L. (2001). Droplet spectra broadening in cumulus clouds.

    Part II: Microscale droplet concentration heterogeneities. *Journal of the Atmospheric*

    Sciences, *58*(6), 642–654. https://doi.org/10.1175/1520-

    0469(2001)058<0642:DSBICC>2.0.CO;2

Chen, Y. C., Xue, L., Lebo, Z. J., Wang, H., Rasmussen, R. M., & Seinfeld, J. H. (2011).

    A comprehensive numerical study of aerosol-cloud-precipitation interactions in

    marine stratocumulus. *Atmospheric Chemistry and Physics*, *11*(18), 9749–9769.

    https://doi.org/10.5194/acp-11-9749-2011

Christensen, M. W., Carrió, G. G., Stephens, G. L., & Cotton, W. R. (2013). Radiative

    impacts of free-tropospheric clouds on the properties of marine stratocumulus.

    Journal of the Atmospheric Sciences, *70*(10), 3102–3118.

    https://doi.org/10.1175/JAS-D-12-0287.1

Chubb, T., Huang, Y., Jensen, J., Campos, T., Siems, S., & Manton, M. (2016).

    Observations of high droplet number concentrations in Southern Ocean boundary

    layer clouds. *Atmospheric Chemistry and Physics*, *16*(2), 971–987.

    https://doi.org/10.5194/acp-16-971-2016

Chubb, T. H., Jensen, J. B., Siems, S. T., & Manton, M. J. (2013). In situ observations of supercooled liquid clouds over the Southern Ocean during the HIAPER Pole-to-Pole Observation campaigns. *Geophysical Research Letters*, *40*(19), 5280–5285. https://doi.org/10.1002/grl.50986

Chylek, P., Robinson, S., Dubey, M. K., King, M. D., Fu, Q., & Clodius, W. B. (2006). Comparison of near-infrared and thermal infrared cloud phase detections. *Journal of Geophysical Research*, *111*(D20), D20203. https://doi.org/10.1029/2006JD007140

Cober, S. G., & Isaac, G. A. (2012). Characterization of aircraft icing environments with Supercooled Large Drops for application to commercial aircraft certification. *Journal of Applied Meteorology and Climatology*, *51*(2), 265–284. https://doi.org/10.1175/JAMC-D-11-022.1

Cober, S. G., Isaac, G. A., Korolev, A. V., & Strapp, J. W. (2001). Assessing Cloud-Phase Conditions. *Journal of Applied Meteorology*, *40*(11), 1967–1983. https://doi.org/10.1175/1520-0450(2001)040<1967:ACPC>2.0.CO;2

Collins, W. D. (2001). Parameterization of generalized cloud overlap for radiative calculations in general circulation models. *Journal of the Atmospheric Sciences*, *58*(21), 3224–3242. https://doi.org/10.1175/1520-0469(2001)058<3224:POGCOF>2.0.CO;2

Cooper, W. A., Friesen, R. B., Hayman, M., Jensen, J. B., Lenschow, D. H., Romashkin, P. A., et al. (2016). *Characterization of Uncertainty in Measurements of Wind From the NSF/NCAR Gulfstream V Research Aircraft*. Retrieved from https://opensky.ucar.edu/islandora/object/technotes%3A540/datastream/PDF/view

Coopman, Q., Riedi, J., Zeng, S., & Garrett, T. J. (2020). Space-Based Analysis of the

Cloud Thermodynamic Phase Transition for Varying Microphysical and Meteorological Regimes. *Geophysical Research Letters*, *47*(6), e2020GL087122. https://doi.org/10.1029/2020GL087122

Cossich, W., Maestri, T., Magurno, D., Martinazzo, M., Di Natale, G., Palchetti, L., et al. (2021). Ice and mixed-phase cloud statistics on the Antarctic Plateau. *Atmospheric Chemistry and Physics*, *21*(18), 13811–13833. https://doi.org/10.5194/acp-21-13811-2021

Costa, A., Meyer, J., Afchine, A., Luebke, A., Günther, G., Dorsey, J. R., et al. (2017). Classification of Arctic, midlatitude and tropical clouds in the mixed-phase temperature regime. *Atmospheric Chemistry and Physics*, *17*(19), 12219–12238. https://doi.org/10.5194/acp-17-12219-2017

Curry, J. A. (1986). Interactions among turbulence, radiation and microphysics in Arctic stratus clouds. *Journal of the Atmospheric Sciences*, *43*(1), 90–106. https://doi.org/10.1175/1520-0469(1986)043<0090:IATRAM>2.0.CO;2

Curry, J. A., Ebert, E. E., & Herman, G. F. (1988). Mean and turbulence structure of the summertime Arctic cloudy boundary layer. *Quarterly Journal of the Royal Meteorological Society*, *114*(481), 715–746. https://doi.org/10.1002/qj.49711448109

D'Alessandro, J. J., Mcfarquhar, G. M., Stith, J. L., Jensen, J. B., Diao, M., DeMott, P. J., & Sanchez, K. J. (in preparation). An evaluation of the phase and microphysical properties of single- and multi-layer clouds over the Southern Ocean using in situ observations from SOCRATES. *Journal of Geophysical Research Atmospheres*.

D'Alessandro, J. J., Diao, M., Wu, C., Liu, X., Jensen, J. B., & Stephens, B. B. (2019). Cloud phase and relative humidity distributions over the Southern Ocean in austral

summer based on in situ observations and CAM5 simulations. *Journal of Climate*, *32*(10), 2781–2805. https://doi.org/10.1175/JCLI-D-18-0232.1

D'Alessandro, J. J., McFarquhar, G. M., Wu, W., Stith, J. L., Jensen, J. B., & Rauber, R. M. (2021). Characterizing the Occurrence and Spatial Heterogeneity of Liquid, Ice, and Mixed Phase Low-Level Clouds Over the Southern Ocean Using in Situ Observations Acquired During SOCRATES. *Journal of Geophysical Research: Atmospheres*, *126*(11), e2020JD034482. https://doi.org/10.1029/2020JD034482

DeMott, P. J., Hill, T. C. J., Petters, M. D., Bertram, A. K., Tobo, Y., Mason, R. H., et al. (2017). Comparative measurements of ambient atmospheric concentrations of ice nucleating particles using multiple immersion freezing methods and a continuous flow diffusion chamber. *Atmospheric Chemistry and Physics*, *17*(18), 11227–11245. https://doi.org/10.5194/acp-17-11227-2017

Devenish, B. J., Bartello, P., Brenguier, J.-L., Collins, L. R., Grabowski, W. W., IJzermans, R. H. A., et al. (2012). Droplet growth in warm turbulent clouds. *Quarterly Journal of the Royal Meteorological Society*, *138*(667), 1401–1429. https://doi.org/10.1002/qj.1897

Diao, M. (2021). VCSEL 1 Hz water vapor data: UCAR/NCAR—Earth Observing Laboratory. Retrieved October 10, 2022, from https://data.eol.ucar.edu/dataset/552.051

Dodson, D. S., & Small Griswold, J. D. (2019). Droplet inhomogeneity in shallow cumuli: The effects of in-cloud location and aerosol number concentration. *Atmospheric Chemistry and Physics*, *19*(11), 7297–7317. https://doi.org/10.5194/acp-19-7297-2019

Eloranta, E. E. (2006). High Spectral Resolution Lidar. In *Lidar* (pp. 143–163). Springer-Verlag. https://doi.org/10.1007/0-387-25101-4_5

EOL. (2018). SOCRATES (2018) Project Manager Report. Retrieved March 8, 2021 from https://www.eol.ucar.edu/system/files/SOCRATES PM Report.pdf

Fiddes, S. L., Protat, A., Mallet, M. D., Alexander, S. P., & Woodhouse, M. T. (2022). Southern Ocean cloud and shortwave radiation biases in a nudged climate model simulation: does the model ever get it right? Retrieved April 11, 2022, from https://acp.copernicus.org/preprints/acp-2022-259/

Field, P. R., Wood, R., Brown, P. R. A., Kaye, P. H., Hirst, E., Greenaway, R., & Smith, J. A. (2003). Ice particle interarrival times measured with a fast FSSP. *Journal of Atmospheric and Oceanic Technology*, *20*(2), 249–261. https://doi.org/10.1175/1520-0426(2003)020<0249:IPITMW>2.0.CO;2

Field, P. R., Hogan, R. J., Brown, P. R. A., Illingworth, A. J., Choularton, T. W., Kaye, P. H., et al. (2004). Simultaneous radar and aircraft observations of mixed-phase cloud at the 100 m scale. *Quarterly Journal of the Royal Meteorological Society*, *130*(600), 1877–1904. https://doi.org/10.1256/qj.03.102

Field, P. R., Heymsfield, A. J., & Bansemer, A. (2006). Shattering and particle interarrival times measured by optical array probes in ice clouds. *Journal of Atmospheric and Oceanic Technology*, *23*(10), 1357–1371. https://doi.org/10.1175/JTECH1922.1

Field, P. R., Lawson, R. P., Brown, P. R. A., Lloyd, G., Westbrook, C., Moisseev, D., et al. (2017). Secondary Ice Production - current state of the science and recommendations for the future. *Meteorological Monographs*, 7.1-7.20.

https://doi.org/10.1175/amsmonographs-d-16-0014.1

Filioglou, M., Mielonen, T., Balis, D., Giannakaki, E., Arola, A., Kokkola, H., et al. (2019). Aerosol Effect on the Cloud Phase of Low-Level Clouds Over the Arctic. *Journal of Geophysical Research: Atmospheres*, *124*(14), 7886–7899. https://doi.org/10.1029/2018JD030088

Findeisen, W. (1938). Kolloid-meteorologische Vorgänge bei Neiderschlags-bildung. *Meteorologische Zeitschrift*, *55*, 121–133.

Findeisen, W. (1940). On the origin of thunderstorm electricity. *Meteorologische Zeitschrift*, *57*, 201–215.

Finlon, J. A., McFarquhar, G. M., Nesbitt, S. W., Rauber, R. M., Morrison, H., Wu, W., & Zhang, P. (2019). A novel approach for characterizing the variability in mass–dimension relationships: results from MC3E. *Atmospheric Chemistry and Physics*, *19*(6), 3621–3643. https://doi.org/10.5194/acp-19-3621-2019

Finlon, J. A., Rauber, R. M., Wu, W., Zaremba, T. J., McFarquhar, G. M., Nesbitt, S. W., et al. (2020). Structure of an Atmospheric River Over Australia and the Southern Ocean: II. Microphysical Evolution. *Journal of Geophysical Research: Atmospheres*, *125*(18). https://doi.org/10.1029/2020JD032514

Fleishauer, R. P., Larson, V. E., & Vonder Haar, T. H. (2002). Observed microphysical structure of midlevel, mixed-phase clouds. *Journal of the Atmospheric Sciences*, *59*(11), 1779–1804. https://doi.org/10.1175/1520-0469(2002)059<1779:OMSOMM>2.0.CO;2

Frey, W. R., & Kay, J. E. (2017). The influence of extratropical cloud phase and amount feedbacks on climate sensitivity. *Climate Dynamics*, 1–20.

https://doi.org/10.1007/s00382-017-3796-5

Gao, S., Lu, C., Liu, Y., Yum, S. S., Zhu, J., Zhu, L., et al. (2021). Comprehensive quantification of height dependence of entrainment mixing between stratiform cloud top and environment. *Atmospheric Chemistry and Physics*, *21*(14), 11225–11241. https://doi.org/10.5194/acp-21-11225-2021

Gao, Z., Liu, Y., Li, X., & Lu, C. (2018). Investigation of Turbulent Entrainment-Mixing Processes With a New Particle-Resolved Direct Numerical Simulation Model. *Journal of Geophysical Research: Atmospheres*, *123*(4), 2194–2214. https://doi.org/10.1002/2017JD027507

Gerber, H. E., Frick, G. M., Jensen, J. B., & Hudson, J. G. (2008). Entrainment, mixing, and microphysics in trade-wind cumulus. *Journal of the Meteorological Society of Japan*, *86A*, 87–106. https://doi.org/10.2151/jmsj.86a.87

Gettelman, A., & Sherwood, S. C. (2016). Processes Responsible for Cloud Feedback. *Current Climate Change Reports*, *2*(4), 179–189. https://doi.org/10.1007/s40641-016-0052-8

Gettelman, A., Bardeen, C. G., McCluskey, C. S., Järvinen, E., Stith, J., Bretherton, C., et al. (2020). Simulating Observations of Southern Ocean Clouds and Implications for Climate. *Journal of Geophysical Research: Atmospheres*, *125*(21), e2020JD032619. https://doi.org/10.1029/2020JD032619

Glienke, S., Kostinski, A., Fugal, J., Shaw, R. A., Borrmann, S., & Stith, J. (2017). Cloud droplets to drizzle: Contribution of transition drops to microphysical and optical properties of marine stratocumulus clouds. *Geophysical Research Letters*, *44*(15), 8002–8010. https://doi.org/10.1002/2017GL074430

Grabowski, W. W., & Wang, L.-P. (2013). Growth of Cloud Droplets in a Turbulent Environment. *Annual Review of Fluid Mechanics*, *45*(1), 293–324. https://doi.org/10.1146/annurev-fluid-011212-140750

Hallett, J., & Mossop, S. C. (1974). Production of secondary ice particles during the riming process. *Nature*, *249*(5452), 26–28. https://doi.org/10.1038/249026a0

Haynes, J. M., Jakob, C., Rossow, W. B., Tselioudis, G., & Brown, J. B. (2011). Major characteristics of Southern Ocean cloud regimes and their effects on the energy budget. *Journal of Climate*, *24*(19), 5061–5080. https://doi.org/10.1175/2011JCLI4052.1

Herman, G., & Goody, R. (1976). Formation and Persistence of Summertime Arctic Stratus Clouds. *Journal of the Atmospheric Sciences*, *33*(8), 1537–1553. https://doi.org/10.1175/1520-0469(1976)033<1537:FAPOSA>2.0.CO;2

Heymsfield, A. J. (1977). Precipitation Development in Stratiform Ice Clouds: A Microphysical and Dynamical Study. *Journal of the Atmospheric Sciences*, *34*(2), 367–381. https://doi.org/10.1175/1520-0469(1977)034<0367:PDISIC>2.0.CO;2

Heymsfield, A. J., & Miloshevich, L. M. (1989). Evaluation of Liquid Water Measuring Instruments in Cold Clouds Sampled during FIRE. *Journal of Atmospheric and Oceanic Technology*, *6*(3), 378–388. https://doi.org/10.1175/1520-0426(1989)006<0378:EOLWMI>2.0.CO;2

Heymsfield, A. J., Field, P. R., Bailey, M., Rogers, D., Stith, J., Twohy, C., et al. (2011). Ice in clouds experiment-layer clouds. Part I: Ice growth rates derived from lenticular wave cloud penetrations. *Journal of the Atmospheric Sciences*, *68*(11), 2628–2654. https://doi.org/10.1175/JAS-D-11-025.1

Hill, A. A., Field, P. R., Furtado, K., Korolev, A., & Shipway, B. J. (2014). Mixed-phase

   clouds in a turbulent environment. Part 1: Large-eddy simulation experiments.

   Quarterly Journal of the Royal Meteorological Society, *140*(680), 855–869.

   https://doi.org/10.1002/qj.2177

Hobbs, P. V., & Rangno, A. L. (1998). Microstructures of low and middle-level clouds

   over the Beaufort Sea. *Quarterly Journal of the Royal Meteorological Society*,

   124(550), 2035–2071. https://doi.org/10.1002/qj.49712455012

Hoffmann, F. (2020). Effects of entrainment and mixing on the wegener-bergeron-

   findeisen process. *Journal of the Atmospheric Sciences*, *77*(6), 2279–2296.

   https://doi.org/10.1175/JAS-D-19-0289.1

Hogan, R. J., Illingworth, A. J., O'Connor, E. J., & PoiaresBaptista, J. P. V. (2003).

   Characteristics of mixed-phase clouds. II: A climatology from ground-based lidar.

   Quarterly Journal of the Royal Meteorological Society, *129*(592), 2117–2134.

   https://doi.org/10.1256/qj.01.209

Holroyd, E. W. (1987). Some Techniques and Uses of 2D-C Habit Classification

   Software for Snow Particles. *Journal of Atmospheric and Oceanic Technology*, *4*(3),

   498–511. https://doi.org/10.1175/1520-0426(1987)004<0498:stauoc>2.0.co;2

Houze, R. A. (2014). Cloud Dynamics - Second Edition. In *International Geophysics*

   (Vol. 104, pp. 1–432). Academic Press. https://doi.org/10.1016/B978-0-12-374266-

   7.00001-9

Hu, Y., Winker, D., Vaughan, M., Lin, B., Omar, A., Trepte, C., et al. (2009).

   CALIPSO/CALIOP cloud phase discrimination algorithm. *Journal of Atmospheric

   and Oceanic Technology*, *26*(11), 2293–2309.

https://doi.org/10.1175/2009JTECHA1280.1

Huang, Y., Siems, S. T., Manton, M. J., Hande, L. B., & Haynes, J. M. (2012). The Structure of Low-Altitude Clouds over the Southern Ocean as Seen by CloudSat. *Journal of Climate*, *25*(7), 2535–2546. https://doi.org/10.1175/JCLI-D-11-00131.1

Huang, Y., Siems, S. T., Manton, M. J., Thompson, G., Huang, Y., Siems, S. T., et al. (2014). An Evaluation of WRF Simulations of Clouds over the Southern Ocean with A-Train Observations. *Monthly Weather Review*, *142*(2), 647–667. https://doi.org/10.1175/MWR-D-13-00128.1

Huang, Y., Siems, S. T., Manton, M. J., & Thompson, G. (2014). An Evaluation of WRF Simulations of Clouds over the Southern Ocean with A-Train Observations. *Monthly Weather Review*, *142*(2), 647–667. https://doi.org/10.1175/MWR-D-13-00128.1

Huang, Y., Franklin, C. N., Siems, S. T., Manton, M. J., Chubb, T., Lock, A., et al. (2015). Evaluation of boundary-layer cloud forecasts over the Southern Ocean in a limited-area numerical weather prediction system using in situ , space-borne and ground-based observations. *Quarterly Journal of the Royal Meteorological Society*, *141*(691), 2259–2276. https://doi.org/10.1002/qj.2519

Huang, Y., Siems, S. T., & Manton, M. J. (2021). Wintertime In Situ Cloud Microphysical Properties of Mixed-Phase Clouds Over the Southern Ocean. *Journal of Geophysical Research: Atmospheres*, *126*(11), e2021JD034832. https://doi.org/10.1029/2021JD034832

Hudson, J. G., & Frisbie, P. R. (1991). Cloud condensation nuclei near marine stratus. *Journal of Geophysical Research*, *96*(D11), 20795–20808. https://doi.org/10.1029/91jd02212

Intrieri, J. M., Shupe, M. D., Uttal, T., & McCarty, B. J. (2002). An annual cycle of

    Arctic cloud characteristics observed by radar and lidar at SHEBA. *Journal of*

    Geophysical Research: Oceans, *107*(10), SHE 5-1.

    https://doi.org/10.1029/2000jc000423

Jackson, R. C., McFarquhar, G. M., Korolev, A. V., Earle, M. E., Liu, P. S. K., Lawson,

    R. P., et al. (2012). The dependence of ice microphysics on aerosol concentration in

    arctic mixed-phase stratus clouds during ISDAC and M-PACE. *Journal of*

    Geophysical Research Atmospheres, *117*(15).

    https://doi.org/10.1029/2012JD017668

Jackson, R. C., Mcfarquhar, G. M., Stith, J., Beals, M., Shaw, R. A., Jensen, J., et al.

    (2014). An assessment of the impact of antishattering tips and artifact removal

    techniques on cloud ice size distributions measured by the 2D cloud probe. *Journal*

    of Atmospheric and Oceanic Technology, *31*(12), 2567–2590.

    https://doi.org/10.1175/JTECH-D-13-00239.1

Jaczewski, A., & Malinowski, S. P. (2005). Spatial distribution of cloud droplets in a

    turbulent cloud-chamber flow. *Quarterly Journal of the Royal Meteorological*

    Society, *131*(609), 2047–2062. https://doi.org/10.1256/qj.04.65

Järvinen, E., McCluskey, C. S., Waitz, F., Schnaiter, M., Bansemer, A., Bardeen, C. G.,

    et al. (2022). Evidence for Secondary Ice Production in Southern Ocean Maritime

    Boundary Layer Clouds. *Journal of Geophysical Research: Atmospheres*, *127*(16),

    e2021JD036411. https://doi.org/10.1029/2021jd036411

Jensen, J. B., & Baker, M. B. (1989). A simple model of droplet spectral evolution during

    turbulent mixing. *Journal of the Atmospheric Sciences*, *46*(18), 2812–2829.

https://doi.org/10.1175/1520-0469(1989)046<2812:ASMODS>2.0.CO;2

Jensen, J. B., & Nugent, A. D. (2017). Condensational growth of drops formed on giant sea-salt aerosol particles. *Journal of the Atmospheric Sciences*, *74*(3), 679–697. https://doi.org/10.1175/JAS-D-15-0370.1

Jolliffe, I. T., & Stephenson, D. B. (2011). Forecast Verification: A Practitioner's Guide in Atmospheric Science, 2nd Edition. Retrieved from https://www.wiley.com/en-us/Forecast+Verification%3A+A+Practitioner%27s+Guide+in+Atmospheric+Scien ce%2C+2nd+Edition-p-9780470660713

Kay, J. E., Hillman, B. R., Klein, S. A., Zhang, Y., Medeiros, B., Pincus, R., et al. (2012). Exposing Global Cloud Biases in the Community Atmosphere Model (CAM) Using Satellite Observations and Their Corresponding Instrument Simulators. *Journal of Climate*, *25*(15), 5190–5207. https://doi.org/10.1175/JCLI-D-11-00469.1

Kay, Jennifer E., Wall, C., Yettella, V., Medeiros, B., Hannay, C., Caldwell, P., & Bitz, C. (2016). Global Climate Impacts of Fixing the Southern Ocean Shortwave Radiation Bias in the Community Earth System Model (CESM). *Journal of Climate*, *29*(12), 4617–4636. https://doi.org/10.1175/JCLI-D-15-0358.1

Khanal, S., & Wang, Z. (2018). Uncertainties in MODIS-Based Cloud Liquid Water Path Retrievals at High Latitudes Due to Mixed-Phase Clouds and Cloud Top Height Inhomogeneity. *Journal of Geophysical Research: Atmospheres*, *123*(19), 11,154-11,172. https://doi.org/10.1029/2018JD028558

Kim, S., & Casper, R. (2013). Applications of convolution in image processing with MATLAB. *University of Washington*, 1–20. Retrieved from http://kiwi.bridgeport.edu/cpeg585/ConvolutionFiltersInMatlab.pdf

King, W. D., Parkin, D. A., & Handsworth, R. J. (1978). A Hot-Wire Liquid Water Device Having Fully Calculable Response Characteristics. *Journal of Applied Meteorology*, *17*(12), 1809–1813. https://doi.org/10.1175/1520-0450(1978)017<1809:AHWLWD>2.0.CO;2

Korolev, A., McFarquhar, G., Field, P. R., Franklin, C., Lawson, P., Wang, Z., et al. (2017). Mixed-Phase Clouds: Progress and Challenges. *Meteorological Monographs*, *58*, 5.1-5.50. https://doi.org/10.1175/AMSMONOGRAPHS-D-17-0001.1

Korolev, A. V. (2007). Limitations of the Wegener–Bergeron–Findeisen Mechanism in the Evolution of Mixed-Phase Clouds. *Journal of the Atmospheric Sciences*, *64*(9), 3372–3375. https://doi.org/10.1175/JAS4035.1

Korolev, Alexei, & Field, P. R. (2008). The Effect of Dynamics on Mixed-Phase Clouds: Theoretical Considerations. *Journal of the Atmospheric Sciences*, *65*(1), 66–86. https://doi.org/10.1175/2007JAS2355.1

Korolev, Alexei, & Isaac, G. A. (2006). Relative Humidity in Liquid, Mixed-Phase, and Ice Clouds. *Journal of the Atmospheric Sciences*, *63*(11), 2865–2880. https://doi.org/10.1175/JAS3784.1

Korolev, Alexei, & Leisner, T. (2020). Review of experimental studies of secondary ice production. *Atmospheric Chemistry and Physics*, *20*(20), 11767–11797. https://doi.org/10.5194/acp-20-11767-2020

Korolev, Alexei, Khain, A., Pinsky, M., & French, J. (2016). Theoretical study of mixing in liquid clouds-Part 1: Classical concepts. *Atmospheric Chemistry and Physics*, *16*(14), 9235–9254. https://doi.org/10.5194/acp-16-9235-2016

Korolev, Alexei V., & Mazin, I. P. (2003). Supersaturation of Water Vapor in Clouds.
Journal of the Atmospheric Sciences, *60*(24), 2957–2974.
https://doi.org/10.1175/1520-0469(2003)060<2957:SOWVIC>2.0.CO;2

Korolev, Alexei V., Isaac, G. A., Cober, S. G., Strapp, J. W., & Hallett, J. (2003).
Microphysical characterization of mixed-phase clouds. *Quarterly Journal of the
Royal Meteorological Society*, *129*(587), 39–65. https://doi.org/10.1256/qj.01.204

Kreidenweis, S. M., Petters, M., & Lohmann, U. (2018). 100 years of progress in cloud
physics, aerosols, and aerosol chemistry research. *Meteorological Monographs*, *59*,
11.1-11.72. https://doi.org/10.1175/AMSMONOGRAPHS-D-18-0024.1

Kumar, B., Schumacher, J., & Shaw, R. A. (2014). Lagrangian mixing dynamics at the
cloudy-clear air interface. *Journal of the Atmospheric Sciences*, *71*(7), 2564–2580.
https://doi.org/10.1175/JAS-D-13-0294.1

Kumar, B., Götzfried, P., Suresh, N., Schumacher, J., & Shaw, R. A. (2018). Scale
Dependence of Cloud Microphysical Response to Turbulent Entrainment and
Mixing. *Journal of Advances in Modeling Earth Systems*, *10*(11), 2777–2785.
https://doi.org/10.1029/2018MS001487

Lamb, D., & Verlinde, J. (2011). *Physics and chemistry of clouds*. *Physics and Chemistry
of Clouds*. Cambridge University Press.
https://doi.org/10.1017/CBO9780511976377

Lance, S., Brock, C. A., Rogers, D., & Gordon, J. A. (2010). Water droplet calibration of
the Cloud Droplet Probe (CDP) and in-flight performance in liquid, ice and mixed-
phase clouds during ARCPAC. *Atmospheric Measurement Techniques*, *3*(6), 1683–
1706. https://doi.org/10.5194/amt-3-1683-2010

Lasher-Trapp, S. G., Cooper, W. A., & Blyth, A. M. (2005). Broadening of droplet size

distributions from entrainment and mixing in a cumulus cloud. *Quarterly Journal of*

the Royal Meteorological Society, *131*(605), 195–220.

https://doi.org/10.1256/qj.03.199

Latham, J., & Reed, R. L. (1977). Laboratory studies of the effects of mixing on the

evolution of cloud droplet spectra. *Quarterly Journal of the Royal Meteorological*

Society, *103*(436), 297–306. https://doi.org/10.1002/qj.49710343607

Lawson, R. P., & Gettelman, A. (2014). Impact of Antarctic mixed-phase clouds on

climate. *Proceedings of the National Academy of Sciences of the United States of*

America, *111*(51), 18156–61. https://doi.org/10.1073/pnas.1418197111

Lehmann, K., Siebert, H., & Shaw, R. A. (2009). Homogeneous and inhomogeneous

mixing in cumulus clouds: Dependence on local turbulence structure. *Journal of the*

Atmospheric Sciences, *66*(12), 3641–3659. https://doi.org/10.1175/2009JAS3012.1

Levin, E. J. T., DeMott, P. J., Suski, K. J., Boose, Y., Hill, T. C. J., McCluskey, C. S., et

al. (2019). Characteristics of Ice Nucleating Particles in and Around California

Winter Storms. *Journal of Geophysical Research: Atmospheres*, *124*(21), 11530–

11551. https://doi.org/10.1029/2019JD030831

Li, J., Yi, Y., Minnis, P., Huang, J., Yan, H., Ma, Y., et al. (2011). Radiative effect

differences between multi-layered and single-layer clouds derived from CERES,

CALIPSO, and CloudSat data. *Journal of Quantitative Spectroscopy and Radiative*

Transfer, *112*(2), 361–375. https://doi.org/10.1016/j.jqsrt.2010.10.006

Liu, Y., Key, J. R., Ackerman, S. A., Mace, G. G., & Zhang, Q. (2012). Arctic cloud

macrophysical characteristics from CloudSat and CALIPSO. *Remote Sensing of*

Environment, *124*, 159–173. https://doi.org/10.1016/j.rse.2012.05.006

Lu, C., Liu, Y., & Niu, S. (2011). Examination of turbulent entrainment-mixing mechanisms using a combined approach. *Journal of Geophysical Research*, *116*(D20), D20207. https://doi.org/10.1029/2011JD015944

Lu, C., Liu, Y., Zhu, B., Yum, S. S., Krueger, S. K., Qiu, Y., et al. (2018). On Which Microphysical Time Scales to Use in Studies of Entrainment-Mixing Mechanisms in Clouds. *Journal of Geophysical Research: Atmospheres*, *123*(7), 3740–3756. https://doi.org/10.1002/2017JD027985

Luo, Y., Xu, K.-M., Morrison, H., McFarquhar, G. M., Wang, Z., & Zhang, G. (2008). Multi-layer arctic mixed-phase clouds simulated by a cloud-resolving model: Comparison with ARM observations and sensitivity experiments. *Journal of Geophysical Research*, *113*(D12), D12208. https://doi.org/10.1029/2007JD009563

Mace, G. G. (2010). Cloud properties and radiative forcing over the maritime storm tracks of the Southern Ocean and North Atlantic derived from A-Train. *Journal of Geophysical Research*, *115*(D10), D10201. https://doi.org/10.1029/2009JD012517

Mace, G. G., Protat, A., & Benson, S. (2021). Mixed-Phase Clouds Over the Southern Ocean as Observed From Satellite and Surface Based Lidar and Radar. *Journal of Geophysical Research: Atmospheres*, *126*(16), e2021JD034569. https://doi.org/10.1029/2021JD034569

Matus, A. V., & L'Ecuyer, T. S. (2017). The role of cloud phase in Earth's radiation budget. *Journal of Geophysical Research: Atmospheres*, *122*(5), 2559–2578. https://doi.org/10.1002/2016JD025951

Mazin, I. P., Korolev, A. V., Heymsfield, A., Isaac, G. A., & Cober, S. G. (2001).

Thermodynamics of Icing Cylinder for Measurements of Liquid Water Content in Supercooled Clouds. *Journal of Atmospheric and Oceanic Technology*, *18*(4), 543–558. https://doi.org/10.1175/1520-0426(2001)018<0543:TOICFM>2.0.CO;2

McCluskey, C. S., Hill, T. C. J., Humphries, R. S., Rauker, A. M., Moreau, S., Strutton, P. G., et al. (2018). Observations of Ice Nucleating Particles Over Southern Ocean Waters. *Geophysical Research Letters*, *45*(21), 11,989-11,997. https://doi.org/10.1029/2018GL079981

McCoy, D. T., Hartmann, D. L., Grosvenor, D. P., McCoy, D. T., Hartmann, D. L., & Grosvenor, D. P. (2014). Observed Southern Ocean Cloud Properties and Shortwave Reflection. Part I: Calculation of SW Flux from Observed Cloud Properties*. *Journal of Climate*, *27*(23), 8836–8857. https://doi.org/10.1175/JCLI-D-14-00287.1

McCoy, D. T., Hartmann, D. L., & Grosvenor, D. P. (2014). Observed Southern Ocean Cloud Properties and Shortwave Reflection. Part II: Phase Changes and Low Cloud Feedback*. *Journal of Climate*, *27*(23), 8858–8868. https://doi.org/10.1175/JCLI-D-14-00288.1

McCoy, I. L., Bretherton, C. S., Wood, R., Twohy, C. H., Gettelman, A., Bardeen, C. G., & Toohey, D. W. (2021). Influences of Recent Particle Formation on Southern Ocean Aerosol Variability and Low Cloud Properties. *Journal of Geophysical Research: Atmospheres*, *126*(8), e2020JD033529. https://doi.org/10.1029/2020JD033529

McFarquhar, G., Um, J., Freer, M., Baumgardner, D., Kok, G. L., & Mace, G. (2007). Importance of small ice crystals to cirrus properties: Observations from the Tropical Warm Pool International Cloud Experiment (TWP-ICE). *Geophysical Research*

Letters, *34*(13). https://doi.org/10.1029/2007GL029865

McFarquhar, G. M., Finlon, J. A., Stechman, D. M., Wu, W., & Jackson, Robert M. Freer, M. (2018). University of Illinois/Oklahoma Optical Array Probe (OAP) Processing Software. Version 3.1.4. Zenodo. https://doi.org/doi:http://doi.org/10.5281/

McFarquhar, Greg, Zhang, G., Poellot, M. R., Kok, G. L., McCoy, R., Tooman, T., et al. (2007). Ice properties of single-layer stratocumulus during the Mixed-Phase Arctic Cloud Experiment: 1. Observations. *Journal of Geophysical Research*, *112*(D24), D24201. https://doi.org/10.1029/2007JD008633

McFarquhar, Greg, Ghan, S., Verlinde, J., Korolev, A., Strapp, J. W., Schmid, B., et al. (2011). Indirect and semi-direct aerosol campaign: The impact of arctic aerosols on clouds. *Bulletin of the American Meteorological Society*, *92*(2), 183–201. https://doi.org/10.1175/2010BAMS2935.1

McFarquhar, Greg M. (2004). The effect of raindrop clustering on collision-induced break-up of raindrops. *Quarterly Journal of the Royal Meteorological Society*, *130*(601), 2169–2190. https://doi.org/10.1256/qj.03.98

McFarquhar, Greg M., & Cober, S. G. (2004). Single-scattering properties of mixed-phase Arctic clouds at solar wavelengths: Impacts on radiative transfer. *Journal of Climate*, *17*(19), 3799–3813. https://doi.org/10.1175/1520-0442(2004)017<3799:SPOMAC>2.0.CO;2

McFarquhar, Greg M., Baumgardner, D., Bansemer, A., Abel, S. J., Crosier, J., French, J., et al. (2017). Processing of Ice Cloud In Situ Data Collected by Bulk Water, Scattering, and Imaging Probes: Fundamentals, Uncertainties, and Efforts toward

Consistency. *Meteorological Monographs*, *58*, 11.1-11.33.

https://doi.org/10.1175/amsmonographs-d-16-0007.1

McFarquhar, Greg M., Bretherton, C., Marchand, R., Protat, A., DeMott, P. J.,

Alexander, S. P., et al. (2021). Observations of clouds, aerosols, precipitation, and

surface radiation over the Southern Ocean: An overview of CAPRICORN,

MARCUS, MICRE and SOCRATES. *Bulletin of the American Meteorological*

Society, *102*(4), E894–E928. https://doi.org/10.1175/bams-d-20-0132.1

Meischner, P., Baumann, R., Höller, H., & Jank, T. (2001). Eddy dissipation rates in

thunderstorms estimated by Doppler radar in relation to aircraft in situ

measurements. *Journal of Atmospheric and Oceanic Technology*, *18*(10), 1609–

1627. https://doi.org/10.1175/1520-0426(2001)018<1609:EDRITE>2.0.CO;2

Mellado, J. P. (2017). Cloud-Top Entrainment in Stratocumulus Clouds. *Annual Review*

of Fluid Mechanics, *49*(1), 145–169. https://doi.org/10.1146/annurev-fluid-010816-

060231

Mioche, G., Jourdan, O., Ceccaldi, M., & Delanoë, J. (2015). Variability of mixed-phase

clouds in the Arctic with a focus on the Svalbard region: A study based on

spaceborne active remote sensing. *Atmospheric Chemistry and Physics*, *15*(5),

2445–2461. https://doi.org/10.5194/acp-15-2445-2015

Mioche, G., Jourdan, O., Delanoë, J., Gourbeyre, C., Febvre, G., Dupuy, R., et al. (2017).

Vertical distribution of microphysical properties of Arctic springtime low-level

mixed-phase clouds over the Greenland and Norwegian seas. *Atmospheric*

Chemistry and Physics, *17*(20), 12845–12869. https://doi.org/10.5194/acp-17-

12845-2017

Mitchell, J. F. B., Senior, C. A., & Ingram, W. J. (1989). C02 and climate: a missing feedback? *Nature*, *341*(6238), 132–134. https://doi.org/10.1038/341132a0

Morrison, A. E., Siems, S. T., & Manton, M. J. (2011). A Three-Year Climatology of Cloud-Top Phase over the Southern Ocean and North Pacific. *Journal of Climate*, *24*(9), 2405–2418. https://doi.org/10.1175/2010JCLI3842.1

Morrison, H., de Boer, G., Feingold, G., Harrington, J., Shupe, M. D., & Sulia, K. (2012). Resilience of persistent Arctic mixed-phase clouds. *Nature Geoscience*, *5*(1), 11–17. https://doi.org/10.1038/ngeo1332

Mossop, S. C. (1956). Sublimation nuclei. *Proceedings of the Physical Society. Section B*, *69*(2), 161–164. https://doi.org/10.1088/0370-1301/69/2/305

Mülmenstädt, J., Sourdeval, O., Delanoë, J., & Quaas, J. (2015). Frequency of occurrence of rain from liquid-, mixed-, and ice-phase clouds derived from A-Train satellite retrievals. *Geophysical Research Letters*, *42*(15), 6502–6509. https://doi.org/10.1002/2015GL064604

Murphy, D. M., & Koop, T. (2005). Review of the vapour pressures of ice and supercooled water for atmospheric applications. *Quarterly Journal of the Royal Meteorological Society*, *131*(608), 1539–1565. https://doi.org/10.1256/qj.04.94

Nagao, T. M., & Suzuki, K. (2021). Temperature-Independent Cloud Phase Retrieval From Shortwave-Infrared Measurement of GCOM-C/SGLI With Comparison to CALIPSO. *Earth and Space Science*, *8*(11), e2021EA001912. https://doi.org/10.1029/2021EA001912

Naud, C. M., Booth, J. F., & Del Genio, A. D. (2014). Evaluation of ERA-Interim and MERRA cloudiness in the southern ocean. *Journal of Climate*, *27*(5), 2109–2124.

https://doi.org/10.1175/JCLI-D-13-00432.1

Paluch, I. R. (1986). Mixing and the cloud droplet size spectrum: generalizations from the CCOPE data. *Journal of the Atmospheric Sciences*, *43*(18), 1984–1993. https://doi.org/10.1175/1520-0469(1986)043<1984:MATCDS>2.0.CO;2

Paluch, I. R., & Baumgardner, D. G. (1989). Entrainment and fine-scale mixing in a continental convective cloud. *Journal of the Atmospheric Sciences*, *46*(2), 261–278. https://doi.org/10.1175/1520-0469(1989)046<0261:EAFSMI>2.0.CO;2

Paluch, I. R., & Knight, C. A. (1984). Mixing and the evolution of cloud droplet size spectra in a vigorous continental cumulus. *Journal of the Atmospheric Sciences*, *41*(11), 1801–1815. https://doi.org/10.1175/1520-0469(1984)041<1801:MATEOC>2.0.CO;2

Panofsky, H. A., & Dutton, J. A. (1984). Atmospheric Turbulence Models and Methods for Engineering Applications. Retrieved from http://www.sciepub.com/reference/40493

Pawlowska, H., Brenguier, J. L., & Burnet, F. (2000). Microphysical properties of stratocumulus clouds. *Atmospheric Research*, *55*(1), 15–33. https://doi.org/10.1016/S0169-8095(00)00054-5

Pinsky, M., Khain, A., & Korolev, A. (2015). Phase transformations in an ascending adiabatic mixed-phase cloud volume. *Journal of Geophysical Research: Atmospheres*, *120*(8), 3329–3353. https://doi.org/10.1002/2015JD023094

Pinsky, M., Khain, A., & Korolev, A. (2018). Theoretical analysis of liquid-ice interaction in the unsaturated environment with application to the problem of homogeneous mixing. *Journal of the Atmospheric Sciences*, *75*(4), 1045–1062.

https://doi.org/10.1175/JAS-D-17-0228.1

Praz, C., Ding, S., McFarquhar, G. M., & Berne, A. (2018). A Versatile Method for Ice
Particle Habit Classification Using Airborne Imaging Probe Data. *Journal of
Geophysical Research: Atmospheres*, *123*(23), 13,472-13,495.
https://doi.org/10.1029/2018JD029163

Pruppacher, H. R., & Klett, J. D. (1996). *Microphysics of Clouds and Precipitation*.
Springer Netherlands.

Rahn, D. A., & Garreaud, R. (2010). Marine boundary layer over the subtropical
southeast Pacific during VOCALS-REx-Part 1: Mean structure and diurnal cycle.
Atmospheric Chemistry and Physics, *10*(10), 4491–4506.
https://doi.org/10.5194/acp-10-4491-2010

Rangno, A. L., & Hobbs, P. V. (1991). Ice particle concentrations and precipitation
development in small polar maritime cumuliform clouds. *Quarterly Journal of the
Royal Meteorological Society*, *117*(497), 207–241.
https://doi.org/10.1002/qj.49711749710

Riedi, J., Marchant, B., Platnick, S., Baum, B. A., Thieuleux, F., Oudard, C., et al.
(2010). Cloud thermodynamic phase inferred from merged POLDER and MODIS
data. *Atmospheric Chemistry and Physics*, *10*(23), 11851–11865.
https://doi.org/10.5194/acp-10-11851-2010

Roberts, G. C., & Nenes, A. (2005). A Continuous-Flow Streamwise Thermal-Gradient
CCN Chamber for Atmospheric Measurements. *Aerosol Science and Technology*,
39(3), 206–221. https://doi.org/10.1080/027868290913988

Rogers, R. R., & Yau, M. K. (1996). *A Short Course in Cloud Physics* (3rd ed.). Elsevier.

Retrieved from https://www.elsevier.com/books/a-short-course-in-cloud-physics/yau/978-0-08-057094-5

Romps, D. M. (2010). A direct measure of entrainment. *Journal of the Atmospheric Sciences*, *67*(6), 1908–1927. https://doi.org/10.1175/2010JAS3371.1

Rosenow, A. A., Plummer, D. M., Rauber, R. M., McFarquhar, G. M., Jewett, B. F., & Leon, D. (2014). Vertical velocity and physical structure of generating cells and convection in the comma head region of continental winter cyclones. *Journal of the Atmospheric Sciences*, *71*(5), 1538–1558. https://doi.org/10.1175/JAS-D-13-0249.1

Sanchez, K. J., Roberts, G. C., Saliba, G., Russell, L. M., Twohy, C., Reeves, M. J., et al. (2021). Measurement report: Cloud processes and the transport of biological emissions affect southern ocean particle and cloud condensation nuclei concentrations. *Atmospheric Chemistry and Physics*, *21*(5), 3427–3446. https://doi.org/10.5194/acp-21-3427-2021

Savitzky, A., & Golay, M. J. E. (1964). Smoothing and Differentiation of Data by Simplified Least Squares Procedures. *Analytical Chemistry*, *36*(8), 1627–1639. https://doi.org/10.1021/ac60214a047

Schima, J., McFarquhar, G., Romatschke, U., Vivekanandan, J., D'Alessandro, J., Haggerty, J., et al. (2022). Characterization of Southern Ocean Boundary Layer Clouds Using Airborne Radar, Lidar, and In-situ Cloud Data: Results from SOCRATES. *Journal of Geophysical Research: Atmospheres*.

Schuddeboom, A. J., & McDonald, A. J. (2021). The Southern Ocean Radiative Bias, Cloud Compensating Errors, and Equilibrium Climate Sensitivity in CMIP6 Models. *Journal of Geophysical Research: Atmospheres*, *126*(22), e2021JD035310.

https://doi.org/10.1029/2021JD035310

Schwarzenboeck, A., Mioche, G., Armetta, A., Herber, A., & Gayet, J.-F. (2009). Response of the Nevzorov hot wire probe in clouds dominated by droplet conditions in the drizzle size range. *Atmospheric Measurement Techniques*, *2*(2), 779–788. https://doi.org/10.5194/amt-2-779-2009

Shaw, R. A., Kostinski, A. B., & Larsen, M. L. (2002). Towards quantifying droplet clustering in clouds. *Quarterly Journal of the Royal Meteorological Society*, *128*(582), 1043–1057. https://doi.org/10.1256/003590002320373193

Shaw, Raymond A., Reade, W. C., Collins, L. R., & Verlinde, J. (1998). Preferential concentration of cloud droplets by turbulence: Effects on the early evolution of cumulus cloud droplet spectra. *Journal of the Atmospheric Sciences*, *55*(11), 1965–1976. https://doi.org/10.1175/1520-0469(1998)055<1965:PCOCDB>2.0.CO;2

Shupe, M. D., & Intrieri, J. M. (2004). Cloud Radiative Forcing of the Arctic Surface: The Influence of Cloud Properties, Surface Albedo, and Solar Zenith Angle. *Journal of Climate*, *17*(3), 616–628. https://doi.org/10.1175/1520-0442(2004)017<0616:CRFOTA>2.0.CO;2

Small, J. D., & Chuang, P. Y. (2008). New observations of precipitation initiation in warm cumulus clouds. *Journal of the Atmospheric Sciences*, *65*(9), 2972–2982. https://doi.org/10.1175/2008JAS2600.1

Solomon, A., Shupe, M. D., Persson, P. O. G., & Morrison, H. (2011). Moisture and dynamical interactions maintaining decoupled Arctic mixed-phase stratocumulus in the presence of a humidity inversion. *Atmospheric Chemistry and Physics*, *11*(19), 10127–10148. https://doi.org/10.5194/acp-11-10127-2011

Stephens, B. B., Long, M. C., Keeling, R. F., Kort, E. A., Sweeney, C., Apel, E. C., et al. (2018). The O2 /N2 Ratio and CO2 Airborne Southern Ocean Study. *Bulletin of the American Meteorological Society*, *99*(2), 381–402. https://doi.org/10.1175/BAMS-D-16-0206.1

Stith, J. L., Ramanathan, V., Cooper, W. A., Roberts, G. C., DeMott, P. J., Carmichael, G., et al. (2009). An overview of aircraft observations from the Pacific Dust Experiment campaign. *Journal of Geophysical Research*, *114*(D5), D05207. https://doi.org/10.1029/2008JD010924

Storelvmo, T., Kristjánsson, J. E., & Lohmann, U. (2008). Aerosol Influence on Mixed-Phase Clouds in CAM-Oslo. *Journal of the Atmospheric Sciences*, *65*(10), 3214–3230. https://doi.org/10.1175/2008JAS2430.1

Stubenrauch, C. J., Rossow, W. B., Scott, N. A., & Chédin, A. (1999). Clouds as seen by satellite sounders (3I) and imagers (ISCCP). Part III: Spatial heterogeneity and radiative effects. *Journal of Climate*, *12*(12), 3419–3442. https://doi.org/10.1175/1520-0442(1999)012<3419:CASBSS>2.0.CO;2

Sun, Z., & Shine, K. P. (1994). Studies of the radiative properties of ice and mixed-phase clouds. *Quarterly Journal of the Royal Meteorological Society*, *120*(515), 111–137. https://doi.org/10.1002/qj.49712051508

Tan, I., Storelvmo, T., & Zelinka, M. D. (2016). Observational constraints on mixed-phase clouds imply higher climate sensitivity. *Science*, *352*(6282), 224–227. https://doi.org/10.1126/science.aad5300

Tan, Ivy, & Storelvmo, T. (2016). Sensitivity Study on the Influence of Cloud Microphysical Parameters on Mixed-Phase Cloud Thermodynamic Phase

Partitioning in CAM5. *Journal of the Atmospheric Sciences*, *73*(2), 709–728. https://doi.org/10.1175/JAS-D-15-0152.1

Tölle, M. H., & Krueger, S. K. (2014). Effects of entrainment and mixing on droplet size distributions in warm cumulus clouds. *Journal of Advances in Modeling Earth Systems*, *6*(2), 281–299. https://doi.org/10.1002/2012MS000209

Trenberth, K. E., & Fasullo, J. T. (2010). Simulation of Present-Day and Twenty-First-Century Energy Budgets of the Southern Oceans. *Journal of Climate*, *23*(2), 440–454. https://doi.org/10.1175/2009JCLI3152.1

Tsay, S. C., & Jayaweera, K. (1984). Physical characteristics of Arctic stratus clouds. *Journal of Climate & Applied Meteorology*, *23*(4), 584–596. https://doi.org/10.1175/1520-0450(1984)023<0584:PCOASC>2.0.CO;2

Tsushima, Y., Emori, S., Ogura, T., Kimoto, M., Webb, M. J., Williams, K. D., et al. (2006). Importance of the mixed-phase cloud distribution in the control climate for assessing the response of clouds to carbon dioxide increase: a multi-model study. *Climate Dynamics*, *27*(2–3), 113–126. https://doi.org/10.1007/s00382-006-0127-7

Twohy, C. H., McMeeking, G. R., DeMott, P. J., McCluskey, C. S., Hill, T. C. J., Burrows, S. M., et al. (2016). Abundance of fluorescent biological aerosol particles at temperatures conducive to the formation of mixed-phase and cirrus clouds. *Atmospheric Chemistry and Physics*, *16*(13), 8205–8225. https://doi.org/10.5194/acp-16-8205-2016

Verlinde, J., Harrington, J. Y., McFarquhar, G. M., Yannuzzi, V. T., Avramov, A., Greenberg, S., et al. (2007). The mixed-phase arctic cloud experiment. *Bulletin of the American Meteorological Society*, *88*(2), 205–221.

https://doi.org/10.1175/BAMS-88-2-205

Verlinde, Johannes, Rambukkange, M. P., Clothiaux, E. E., McFarquhar, G. M., & Eloranta, E. W. (2013). Arctic multilayered, mixed-phase cloud processes revealed in millimeter-wave cloud radar Doppler spectra. *Journal of Geophysical Research: Atmospheres*, *118*(23), 13,199-13,213. https://doi.org/10.1002/2013JD020183

Vivekanandan, J., Ellis, S., Tsai, P., Loew, E., Lee, W. C., Emmett, J., et al. (2015). A wing pod-based millimeter wavelength airborne cloud radar A wing pod-based millimeter wavelength airborne cloud radar A wing pod-based millimeter wavelength airborne cloud radar. *Geosci. Instrum. Method. Data Syst. Discuss*, *5*, 117–159. https://doi.org/10.5194/gid-5-117-2015

Wang, J., Jian, B., Wang, G., Zhao, Y., Li, Y., Letu, H., et al. (2021). Climatology of cloud phase, cloud radiative effects and precipitation properties over the tibetan plateau. *Remote Sensing*, *13*(3), 1–21. https://doi.org/10.3390/rs13030363

Wang, Yang, McFarquhar, G. M., Rauber, R. M., Zhao, C., Wu, W., Finlon, J. A., et al. (2020). Microphysical Properties of Generating Cells Over the Southern Ocean: Results From SOCRATES. *Journal of Geophysical Research: Atmospheres*, *125*(13). https://doi.org/10.1029/2019JD032237

Wang, Yong, Zhang, D., Liu, X., & Wang, Z. (2018). Distinct Contributions of Ice Nucleation, Large-Scale Environment, and Shallow Cumulus Detrainment to Cloud Phase Partitioning With NCAR CAM5. *Journal of Geophysical Research: Atmospheres*, *123*(2), 1132–1154. https://doi.org/10.1002/2017JD027213

Wang, Z., Mora Ramirez, M., Dadashazar, H., MacDonald, A. B., Crosbie, E., Bates, K. H., et al. (2016). Contrasting cloud composition between coupled and decoupled

marine boundary layer clouds. *Journal of Geophysical Research: Atmospheres*, *121*(19), 11,679-11,691. https://doi.org/10.1002/2016JD025695

Wegener, A. (1911). *Thermodynamik der Atmosphäre*. Leipzig, Germany: J. A. Barth.

Wofsy, S. C., & HIPPO Science Team and Cooperating Modellers and Satellite Teams. (2011). HIAPER Pole-to-Pole Observations (HIPPO): fine-grained, global-scale measurements of climatically important atmospheric gases and aerosols. *Philosophical Transactions. Series A, Mathematical, Physical, and Engineering Sciences*, *369*(1943), 2073–86. https://doi.org/10.1098/rsta.2010.0313

Wood, R. (2012). Stratocumulus clouds. *Monthly Weather Review*. American Meteorological Society. https://doi.org/10.1175/MWR-D-11-00121.1

Wu, W., & McFarquhar, G. M. (2019). NSF/NCAR GV Hiaper fast 2DS particle size distribution (psd) product data. Version 1.1. UCAR/NCAR-Earth Observing Laboratorytle. https://doi.org/https://doi.org/10.26023/8hmg-wqp3-xa0x

Yang, C. A., Diao, M., Gettelman, A., Zhang, K., Sun, J., McFarquhar, G., & Wu, W. (2021). Ice and Supercooled Liquid Water Distributions Over the Southern Ocean Based on In Situ Observations and Climate Model Simulations. *Journal of Geophysical Research: Atmospheres*, *126*(24), e2021JD036045. https://doi.org/10.1029/2021JD036045

Yum, S. S., Wang, J., Liu, Y., Senum, G., Springston, S., McGraw, R., & Yeom, J. M. (2015). Cloud microphysical relationships and their implication on entrainment and mixing mechanism for the stratocumulus clouds measured during the VOCALS project. *Journal of Geophysical Research: Atmospheres*, *120*(10), 5047–5069. https://doi.org/10.1002/2014JD022802

Zaremba, T. J., Rauber, R. M., McFarquhar, G. M., Hayman, M., Finlon, J. A., & Stechman, D. M. (2020). Phase Characterization of Cold Sector Southern Ocean Cloud Tops: Results from SOCRATES. *Journal of Geophysical Research: Atmospheres*. https://doi.org/10.1029/2020JD033673

Zhang, M., Liu, X., Diao, M., D'Alessandro, J. J., Wang, Y., Wu, C., et al. (2019). Impacts of Representing Heterogeneous Distribution of Cloud Liquid and Ice on Phase Partitioning of Arctic Mixed-Phase Clouds with NCAR CAM5. *Journal of Geophysical Research: Atmospheres*, *124*(23), 13071–13090. https://doi.org/10.1029/2019JD030502

Zondlo, M. A., Paige, M. E., Massick, S. M., & Silver, J. A. (2010). Vertical cavity laser hygrometer for the National Science Foundation Gulfstream-V aircraft. *Journal of Geophysical Research*, *115*(D20), D20309. https://doi.org/10.1029/2010JD014445